MICROWAVE METAMATERIAL CIRCUITS

INTRODUCTION

Electromagnetic metamaterials are usually defined as artificial effectively homogeneous structures with specific properties that cannot be observed in natural materials. A classic example of metamaterial is the structure exhibiting simultaneously negative values of the dielectric permittivity ε and the magnetic permeability μ. Very often the concept of "left-handedness" is used for the structures with backward electromagnetic waves in contrast to conventional materials with forward electromagnetic waves where the electric field, the magnetic field, and the propagation vector form the right-handed triad (1–3).

Different approaches are used for a description of the fundamental electromagnetic properties of metamaterials and the practical realization of these materials as well. Among them, the transmission line (TL) approach gives an efficient design tool for microwave applications providing a correct description of physical properties of metamaterials (4, 5). A conventional transmission line with positive phase velocity behaves as a right-handed transmission line (RH TL). An artificial RH TL can be formed as a ladder network of capacitors connected in shunt and series inductors. The unit cell of the RH TL is shown in Figure 1a. The dual transmission line can be designed as a ladder network of inductors connected in shunt and series capacitors as in the unit cell in Figure 1b. This line has negative phase velocity and is referred to as the left-handed transmission line (LH TL). A backward wave propagates along the LH TL, which can be considered as the one-dimensional metamaterial. A more general model of an LH TL is the composite right/left handed (CRLH) structure, which includes RH effects (5, 6). In many practical applications, the influence of RH effects is negligibly small and many interesting features can be observed when a combination of RH TL and LH TL is used. The most important feature of the LH and RH TLs is that their dispersion characteristics are described by different equations. That can be used for many beneficial applications. Furthermore, we consider comprehensively properties of LH and RH TLs and different combinations of these lines, which can be used for a design of miniature microwave devices with improved performance and enlarged functionality. Among them are microwave filters, microwave power divider/combiners, microwave phase shifters, matching circuits, etc.

DEFINITIONS AND GENERAL EQUATIONS FOR METAMATERIAL TRANSMISSION LINES: RH TL AND LH TL

The homogeneous RH TL presented as a cascaded connection of the unit cells (Figure 1a) is described by the telegraph equations:

$$\begin{aligned} \frac{\partial V}{\partial z} &= -L_1 \frac{\partial I}{\partial t} \\ \frac{\partial I}{\partial z} &= -C_1 \frac{\partial V}{\partial t} \end{aligned} \tag{1}$$

where L_1 and C_1 are the inductance and capacitance per unit length correspondingly. V is the voltage and I is the current, and both are periodical with respect to time t and coordinate z, along which the I-V wave propagates.

In the case of harmonic waves $\frac{\partial}{\partial t} = i\omega$ (ω is the circular frequency) and the wave equations for voltage and current look as follows:

$$\frac{\partial^2 V}{\partial z^2} = -\omega^2 L_1 C_1 V \tag{2}$$

$$\frac{\partial^2 I}{\partial z^2} = -\omega^2 L_1 C_1 I \tag{3}$$

The solutions to the equations 2 and 3 are

$$V = V_0 e^{i(\omega t - kz)} \tag{4}$$

$$I = I_0 e^{i(\omega t - kz)} \tag{5}$$

where the wave number $k = k_R$ is defined as

$$k_R = \omega\sqrt{L_1 C_1} > 0 \tag{6}$$

Both the phase and group velocities are positive:

$$V_{ph} = \frac{\omega}{k_R} = \frac{1}{\sqrt{L_1 C_1}} > 0 \tag{7}$$

$$V_g = \left(\frac{\partial k_R}{\partial \omega}\right)^{-1} = V_{ph} = \frac{1}{\sqrt{L_1 C_1}} > 0 \tag{8}$$

Therefore the forward wave propagates in the RH TL. In line with equation 6 describing the dispersion law, the wave number is proportional to the frequency. The characteristic impedance is defined as

$$Z_0 = \frac{V}{I} = \sqrt{\frac{L_1}{C_1}} \tag{9}$$

For a homogeneous LH TL formed as a cascaded connection of the unit cells (Figure 1b), the telegraph equations in the case of sinusoidal waves look as follows:

$$\frac{\partial V}{\partial z} = -\frac{1}{i\omega} \cdot \left(\frac{1}{C}\right)_1 I \tag{10}$$

$$\frac{\partial I}{\partial z} = -\frac{1}{i\omega} \cdot \left(\frac{1}{L}\right)_1 V \tag{11}$$

where $\left(\frac{1}{C}\right)_1$ and $\left(\frac{1}{L}\right)_1$ are the inverse capacitance and the inverse inductance per unit length. The wave equations are written as

$$\frac{\partial^2 V}{\partial z^2} = -\frac{1}{\omega^2} \cdot \left(\frac{1}{L}\right)_1 \cdot \left(\frac{1}{C}\right)_1 V \tag{12}$$

J. Webster (ed.), *Wiley Encyclopedia of Electrical and Electronics Engineering*. Copyright © 2014 John Wiley & Sons, Inc.

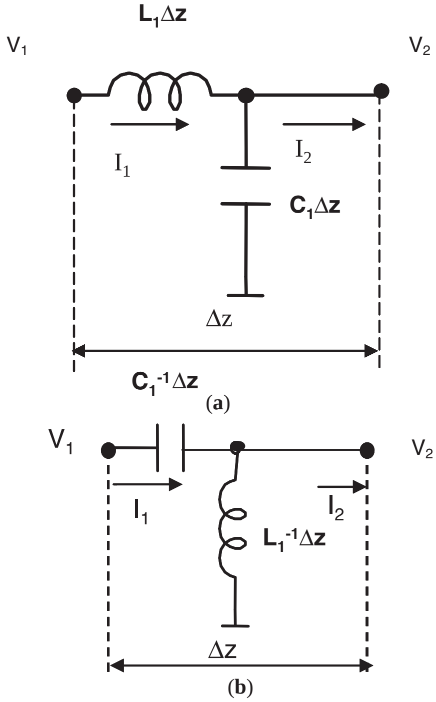

Figure 1. Unit cells of (a) RH TL and (b) LH TL.

$$\frac{\partial^2 I}{\partial z^2} = -\frac{1}{\omega^2}\cdot\left(\frac{1}{L}\right)_1\cdot\left(\frac{1}{C}\right)_1 I \tag{13}$$

The solutions to equations 12 and 13 look like those to equations 4 and 5 with the wave number defined as

$$k_L = -\frac{1}{\omega}\cdot\sqrt{\left(\frac{1}{L}\right)_1\cdot\left(\frac{1}{C}\right)_1} < 0 \tag{14}$$

In this case, the wave number and the phase velocity are negative:

$$V_{ph} = -\omega^2\frac{1}{\sqrt{\left(\frac{1}{L}\right)_1\cdot\left(\frac{1}{C}\right)_1}} < 0 \tag{15}$$

whereas the group velocity is positive

$$V_g = \left(\frac{\partial k_L}{\partial \omega}\right)^{-1} = \omega^2\frac{1}{\sqrt{\left(\frac{1}{L}\right)_1\cdot\left(\frac{1}{C}\right)_1}} > 0 \tag{16}$$

Hence, the backward wave propagates in the LH TL. In line with equation 14, the wave number k_L (propagation constant) is inversely proportional to the frequency.

The characteristic impedance of the LH TL is defined as

$$Z_0 = \sqrt{\frac{\left(\frac{1}{C}\right)_1}{\left(\frac{1}{L}\right)_1}} \tag{17}$$

Equations 1–17 describe the homogeneous infinitely long TLs described by the reactive parameters per unit length. A section of such a line of length l can be described by the electrical length θ defined as

$$\theta_{R,L} = k_{R,L}\cdot l \tag{18}$$

In accordance with equation 6, the frequency dependence of the electrical length of a section of the RH TL is

$$\theta_R(\omega) = \theta_{0R}\frac{\omega}{\omega_0} \tag{19}$$

where $\theta_{0R} = k_R l > 0$ is the electrical length at the frequency ω_0. In the case of a section of LH TL, the electrical length can be found from equations 14 and 18 and the frequency dependence is written as

$$\theta_L(\omega) = \theta_{0L}\frac{\omega_0}{\omega} \tag{20}$$

Here $\theta_{0L} = k_L l < 0$ is the electrical length at the frequency ω_0.

In practice, the artificial RH and LH TLs can be composed as a periodical structure containing one inductive and one capacitive component in the unit cell of the length l defined by a real length of the lumped components (Figure 2). In this case, one has to use the translation symmetry for a description of the *I*-*V* wave propagating along the one-dimensional structure (7, 8). The telegraph equations for the RH TL are written as

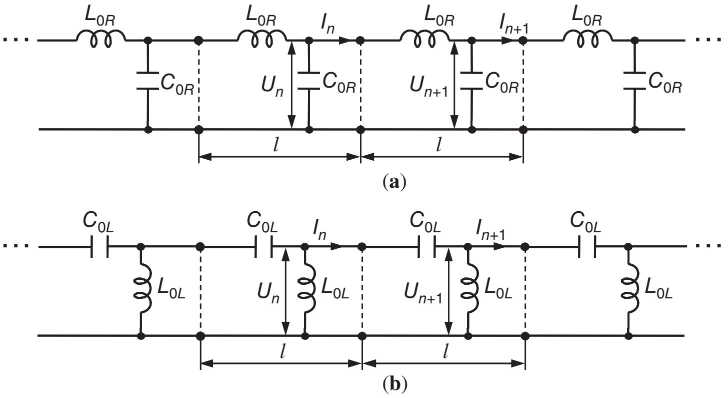

Figure 2. Artificial lumped-element transmission lines: (a) RH TL and (b) LH TL.

$$V_{n+1} - V_n = -i\omega L_{0R} I_{n+1} \quad (21)$$

$$I_{n+1} - I_n = -i\omega C_{0R} V_n \quad (22)$$

The voltage and current are

$$V_n = V_0 e^{-in\theta}, I_n = I_0 e^{-in\theta} \quad (23)$$

with $\theta = kl$, $n = 1, 2, \ldots$

Substituting equation 23 into equations 21 and 22, one obtains after some transformations the dispersion equation:

$$\sin^2\left(\frac{\theta}{2}\right) = \frac{1}{4}\omega^2 L_{0R} C_{0R} = \frac{\omega^2}{\omega_{cR}^2} \quad (24)$$

with the cut-off frequency

$$\omega_{cR} = \frac{2}{\sqrt{L_{0R} C_{0R}}} \quad (25)$$

For $\omega > \omega_{cR}$, θ is an imaginary quantity and the wave attenuates: the higher frequency, the more the attenuation. In the low-frequency limit ($\omega \ll \omega_{cR}$)

$$\frac{\omega}{\omega_{cR}} = \pm\sin\left(\frac{\theta}{2}\right) \cong \pm\frac{\theta}{2} \quad (26)$$

and

$$k_R = \frac{2\omega}{l\omega_{cR}} = \omega\sqrt{L_{1R} C_{1R}} \quad (27)$$

with $L_{1R} = L_{0R}/l$ and $C_{1R} = C_{0R}/l$. The artificial lumped element RH TL behaves at $\omega \ll \omega_c$ as an infinitely long perfect TL with the linear dispersion law. In a wide frequency range, the artificial periodic RH TL (Figure 2a) is considered as a low-pass lumped element TL.

Now we consider the LH TL shown in Figure 2b. It is important to mention that the real capacitances and inductances in this artificial line are related to the parameters per unit length in Figure 1b in line with the following equalities:

$$C_{0L} = \left[C_1{}^{-1} l\right]^{-1} \text{and}\, L_{0L} = \left[L_1{}^{-1} l\right]^{-1}$$

The same consideration of the artificial LH TL (Figure 2b) as it was used for the RH TL (Figure 2a) leads to the following dispersion equation:

$$\sin^2\left(\frac{\theta}{2}\right) = \frac{1}{4}\frac{1}{\omega^2 L_{0L} C_{0L}} = \frac{\omega_{cL}^2}{\omega^2} \quad (28)$$

with the cut-off frequency

$$\omega_{cL} = \frac{1}{2\sqrt{L_{0L} C_{0L}}} \quad (29)$$

For $\omega < \omega_{cL}$, θ is imaginary and the wave attenuates: the lower frequency, the more the attenuation. In the high-frequency limit ($\omega \gg \omega_{cL}$)

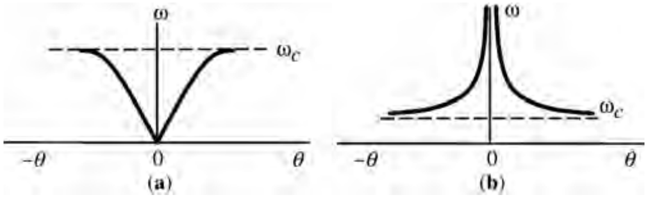

Figure 3. Dispersion characteristics of (a) RH lumped-element TL and (b) LH lumped-element TL.

$$\frac{\omega_{cL}}{\omega} = \pm\sin\left(\frac{\theta}{2}\right) \cong \pm\frac{\theta}{2} \quad (30)$$

and

$$k_L = \frac{1}{\omega}\cdot\sqrt{\left(\frac{1}{L}\right)_{1L}\left(\frac{1}{C}\right)_{1L}} \quad (31)$$

with $\left(\frac{1}{L}\right)_{1L} = \left(\frac{1}{L_{0L}}\right)\cdot\frac{1}{l}$ and $\left(\frac{1}{C}\right)_{1L} = \left(\frac{1}{C_{0L}}\right)\cdot\frac{1}{l}$. The artificial lumped element LH TL (Figure 2b) behaves as an infinitely long perfect TL with k_L inversely proportional to ω. The artificial periodic LH TL is considered as a high-pass lumped element TL. The dispersion characteristics of the RH and LH TLs are shown in Figure 3. On further consideration, the frequency range is limited by the inequalities: $\omega \ll \omega_{cR}$ for the RH TL and $\omega \gg \omega_{cL}$ for the LH TL.

LUMPED EQUIVALENT OF UNIT CELLS OF RH TL AND LH TL

In general, the TL section can be described by the ABCD matrix (9):

$$\begin{bmatrix} A & B \\ C & D \end{bmatrix} = \begin{bmatrix} \cos\theta & iZ_0\sin\theta \\ i\sin\theta/Z_0 & \cos\theta \end{bmatrix} \quad (32)$$

where θ is the electrical length of the TL section at chosen frequency ω and Z_0 is the characteristic impedance of the line. Taking into account the symmetry of the section of homogeneous TL, it is possible to replace it with the symmetric lumped element T- or Π-circuits. The unit cells presented in Figure 4 can be used as equivalent circuits of the sections of RH and LH transmission lines. It is supposed that the geometrical length of the lumped element unit cell is equal to zero. Comparing the matrix (32) with the ABCD matrices of T- and Π-circuits, one can find the *L*-*C* components of the equivalent lumped element unit cells (10):

$$L_{R,T} = \frac{Z_0\tan(\theta_{0R}/2)}{\omega_0}, C_{R,T} = \frac{\sin\theta_{0R}}{\omega_0 Z_0} \quad (33)$$

$$L_{R,\Pi} = \frac{Z_0\sin\theta_{0R}}{\omega_0}, C_{R,\Pi} = \frac{\tan(\theta_{0R}/2)}{\omega_0 Z_0} \quad (34)$$

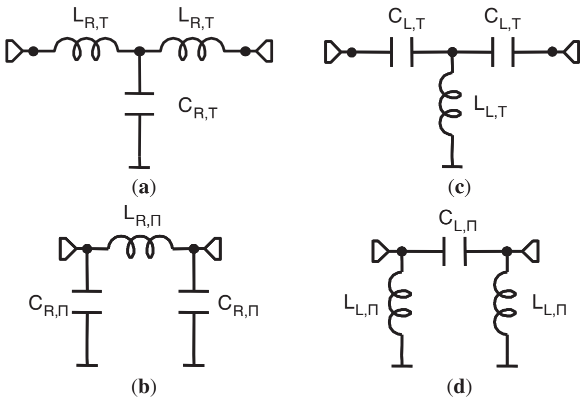

Figure 4. Lumped-element equivalent circuits of the RH TL and LH TL sections.

for the RH TL and

$$L_{L,T} = \frac{Z_0}{\omega_0 \sin|\theta_{0L}|}, C_{L,T} = \frac{1}{\omega_0 Z_0 \tan(|\theta_{0L}|/2)} \quad (35)$$

$$L_{L,\Pi} = \frac{Z_0}{\omega_0 \tan(|\theta_{0L}|/2)}, C_{L,\Pi} = \frac{1}{\omega_0 Z_0 \sin|\theta_{0L}|} \quad (36)$$

for the LH TL.

In the frequency range close to the chosen frequency ω_0, the characteristics of the T- or Π-circuits with LC-parameters defined by equations 33–36 will be the same as for the corresponding RH/LH TL sections with known Z_0 and θ. This equivalent presentation of the RH/LH TL sections is used in a design of microwave devices.

A generalized approach to the metamaterial TLs was suggested in Refs. 5 and 11–15 introducing the concept of a composite right/left-handed (CRLH) transmission line. Figure 5a shows the equivalent circuit of a unit cell of a transmission line containing series capacitor C_L and the inductance L_R. These reactive components form a series resonance circuit with resonance frequency ω_{se}. The short-circuited part of the unit cell is represented by a parallel circuit with capacitor C_R and inductance L_L. This circuit has resonance frequency ω_{sh}. At low frequencies, the properties of the transmission line are determined primarily by parameters L_L and C_L, which provide a negative phase velocity of the wave in the transmission line, that is, impart the properties of an LH TL to the line. At higher frequencies, the properties of the transmission line are governed primarily by reactive components L_R and C_R, which provide a positive phase velocity of the wave in the transmission line, that is, impart the properties of a RH TL line (subscripts R and L refer to the right- and left-handed transmission lines, respectively).

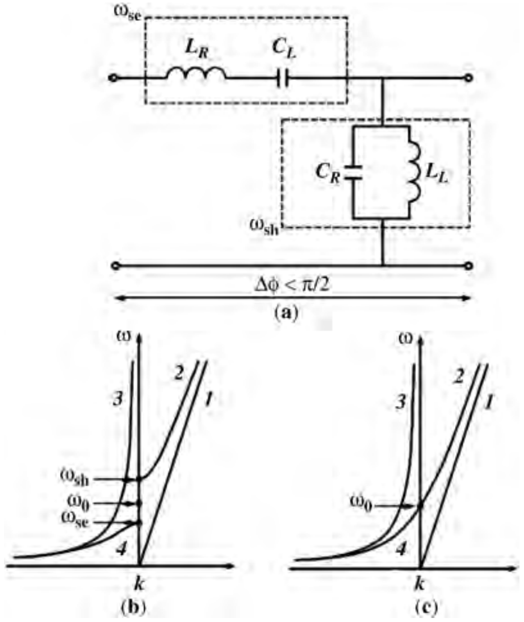

Figure 5. Equivalent circuit of a section of (a) CRLH TL and a dispersion diagram of the CRLH TL: (b) unbalanced case and (c) balanced case.

The dispersion diagram of the unit cell (5) is presented in Figure 5b by curves *2* and *4*. Curves *1* and *3* correspond to ideal RH TL and LH TL. At high frequencies, the absolute value of the impedance of C_L tends to zero, whereas that of the impedance of L_L goes to infinity; accordingly, the cell contains only series inductance L_R and parallel capacitance C_R. The unit cell acts as a low-pass filter with upper cut-off frequency ω_{sh}. Accordingly, at low frequencies, the cell has the properties of a high-pass filter with lower cut-off frequency ω_{se}. In general, frequencies ω_{sh} and ω_{se} are different and therefore there exists a forbidden gap between the positive dispersion and negative dispersion regions. However, if these frequencies are the same, the gap disappears (Figure 5c). In this case, the unit cell is said to be "balanced" and the length of a wave propagating in the transmission line at frequency ω_0 goes to infinity. Despite the "filtering nature" of the composite structure, it is never used at the edge of the Brillouin zone. Note that, although a CRLH structure has both an LH range and an RH range, the dispersion curve in each of these ranges significantly differs from that of the ideal LH and RH structures, respectively, because of the combined effects of LH and RH contributions at all frequencies. A single cell of a CRLH is shown in Figure 6, where the series capacitance is performed as an interdigital capacitor with a parasitic inductance and the shunted inductance is made as a grounded stub with a parasitic capacitance (5). Split-ring resonators (SRRs) and complementary split-ring resonators (CSRRs) are used as a rule for implementing CRLH TLs (Figure 7) (12–15). Near the resonant frequency the SRR behaves as a magnetic dipole and the CSRR exhibits the electric dipole behavior (13). The metamaterial TLs can be implemented also by loading a host RH transmission line with series capacitances and shunt inductances or electrically small resonators (16, 17). Various types of artificial transmission lines are used for a design of resonators exhibiting unusual properties of metamaterial TL sections.

Because CRLH TLs may look at first sight similar to conventional filters, let us now point out the essential distinctions existing between these two types of the structures (5):

- An LH MTM structure exhibits a specific phase response, leading to LH transmission at lower frequencies and RH transmission at higher frequencies.

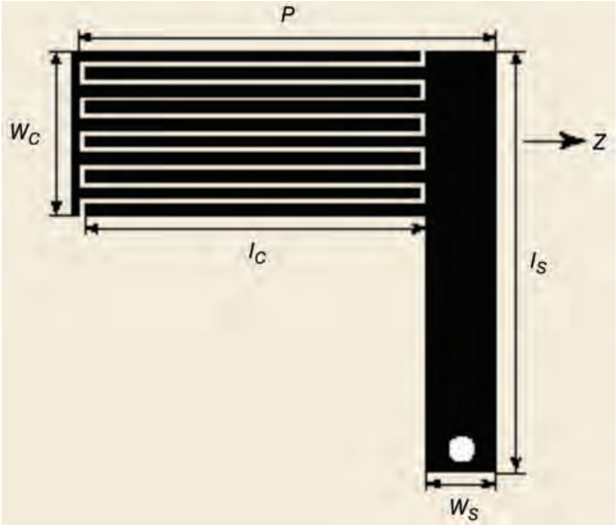

Figure 6. Single cell of CRLH TL. From Reference 11; copyright © 2004 IEEE, reprinted with permission conveyed through Copyright Clearance Center, Inc.

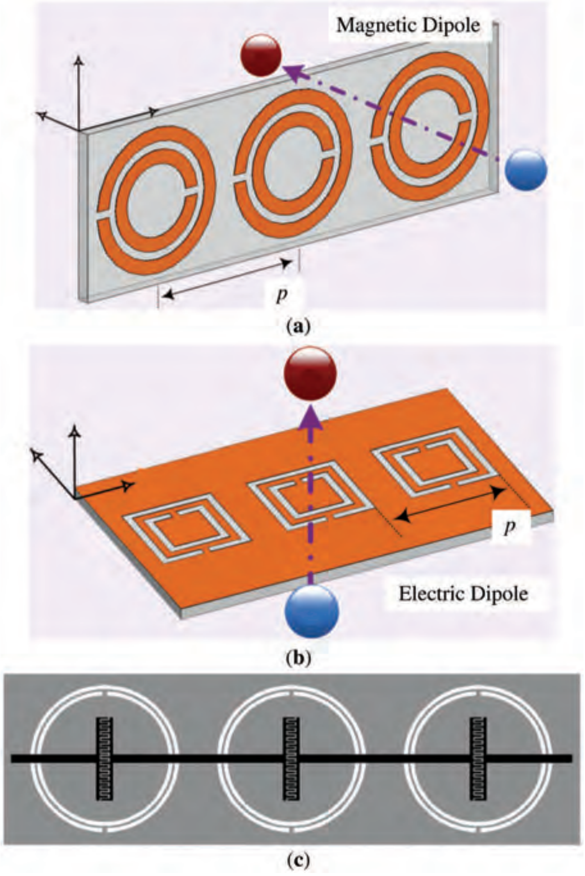

Figure 7. (a) Split-ring resonator (SRR), (b) complementary split-ring resonator (CSRR), and (c) planar CRLH structure composed by interdigital coupling slots and CSRRs on the ground. From Reference 13; copyright © 2012 IEEE, reprinted with permission conveyed through Copyright Clearance Center, Inc.

Conventional filters are generally designed to meet *magnitude* specifications and do not exhibit an LH range.

- An MTM structure is intended to be used as a transmission line or transmission structure. *Only the pass band* is directly useful. The stop bands are usually parasitic effects limiting the operation bandwidth of the MTM. Thus, the filtering characteristic of the network are generally not used in MTM as in filters.
- An MTM structure is constituted of unit cells satisfying the *homogeneity condition* $|\theta| < \pi/2$. Conventional filters do not generally satisfy this condition; they may have node-to-node phase shifts larger than $\pi/2$.
- An MTM structure *can be 2D or 3D and behave as bulk media*, whereas conventional filters are 1D and behave as electric circuits.
- An MTM structure *can be made of identical cells*, whereas in a conventional filter, each "cell" has generally different *LC* values to match the specifications of a given prototype.

MICROWAVE RESONATORS AND FILTERS BASED ON METAMATERIAL TL SECTIONS

General Properties of a Resonator on a Combination of RH/LH TL Sections

A resonator on a transmission line section has a set of resonant frequencies, which are defined by the following resonance condition:

$$\theta_\Sigma = \pi \cdot n, \text{where } n = 0, \pm 1, \pm 2, \pm 3, \ldots \tag{37}$$

where θ_Σ is the total electrical length of the resonator and n is the resonance number. For the resonator on the natural TL section (RH TL), n is positive and the resonant frequencies are multiple numbers. In the case of a cascaded connection of RH and LH TL sections, the spectrum of the resonant frequencies is formed by positive and negative numbers of responses including the zeroth-order resonance (18–20). The spectrum of the resonant frequencies is a set of values defined by the parameters of the RH and LH TL sections.

Let us consider the equivalent diagram of the symmetrical structure of RH-LH-RH resonator (Figure 8). The resonator is formed by a cascaded connection of the RH and LH TL sections. The resonance condition is defined as (20, 21)

$$\begin{aligned}\cos^{-1}\Bigg[&\cos\left(2\theta_R\cdot\frac{f_{+n}}{f_0}\right)\cos\left(2\theta_L\cdot\frac{f_0}{f_{+n}}\right)+0.5(Z_{RL}^{-1}-Z_{RL})\\&\times\sin\left(2\theta_R\cdot\frac{f_{+n}}{f_0}\right)\sin\left(2\theta_L\cdot\frac{f_0}{f_{+n}}\right)2\theta_L\Bigg]=n\cdot\pi\end{aligned} \tag{38}$$

$$\begin{aligned}\cos^{-1}\Bigg[&\cos\left(2\theta_R\cdot\frac{f_{-n}}{f_0}\right)\cos\left(2\theta_L\cdot\frac{f_0}{f_{-n}}\right)+0.5(Z_{RL}^{-1}-Z_{RL})\\&\times\sin\left(2\theta_R\cdot\frac{f_{-n}}{f_0}\right)\sin\left(2\theta_L\cdot\frac{f_0}{f_{-n}}\right)2\theta_L\Bigg]=-n\cdot\pi\end{aligned} \tag{39}$$

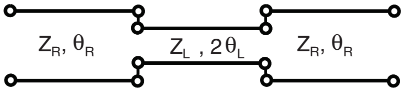

Figure 8. Equivalent circuit of the LH/RH TL resonator.

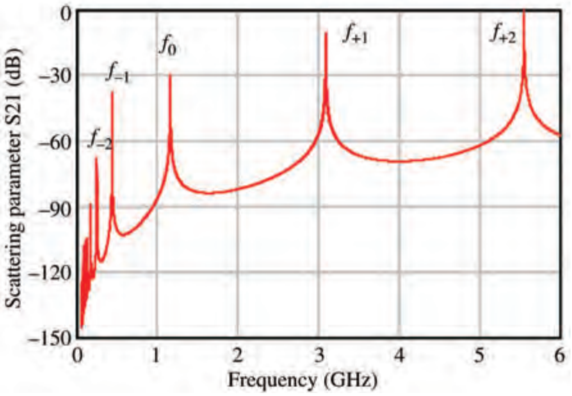

Figure 9. Resonant responses of the RH-LH-RH resonator with $Z_{RL} = 1$ shown in Figure 8.

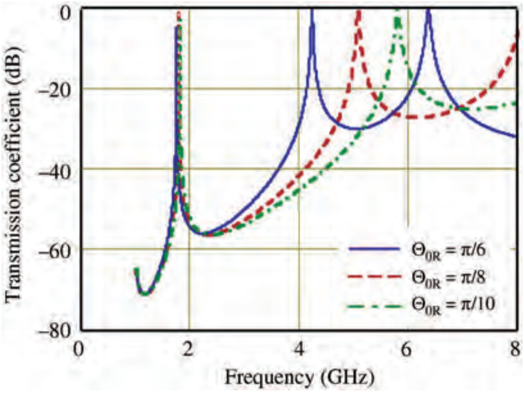

Figure 10. The fundamental ($n = 1$) and the first spurious ($n = 2$) responses of the RH/LH TL resonator for different electrical lengths of RH/TL sections and $Z_R/Z_L = 2.5$.

where f_n and f_{-n} are the resonant frequencies for $n > 0$ and $n < 0$ correspondingly, θ_R and θ_L are the electrical lengths of the TL sections at chosen frequency f_0, and $Z_{RL} = Z_R/Z_L$ is the ratio of the characteristic impedances of the RH and LH TL sections. The resonant frequency spectrum of the resonator is shown in Figure 9. The number of resonances is infinite.

The resonator on a combination of RH/LH TL sections has a unique resonant property, referred to as zeroth-order resonance, when the phase constant of the dominant mode is zero. The phase and amplitude of standing waves in the resonator are distributed uniformly over the whole structure at the resonant frequency. The resonant frequency depends only on the configuration of the unit cells used in the resonator design. Regardless of the operational frequency and resonator components, the zeroth-order resonators can be designed. The resonance condition for the zeroth-order resonator is defined by the following equations:

$$\cos^{-1}\left[\cos 2\theta_R \cos 2\theta_L + 0.5\left(Z_{RL}^{-1} - Z_{RL}\right)\sin 2\theta_R \sin 2\theta_L\right] = 0 \tag{40}$$

$$\sin^{-1}\left[\frac{2\sin\theta_R\cos\theta_L}{\left(Z_{RL} - Z_{RL}^{-1}\right) + \left(Z_{RL} + Z_{RL}^{-1}\right)\cos\theta_R}\right] - \theta_L = 0 \tag{41}$$

In practice, the resonator is designed as a cascaded connection of T- or Π- lumped element unit cells shown in Figure 4.

In many practical applications it is necessary to reject the higher harmonics. The popular way to suppress the higher harmonics is using a stepped impedance resonator (SIR) (22–24). To obtain more freedom in a design of a resonator with suppressed harmonic responses, an SIR based on a cascaded connection of the LH TL and RH TL sections is considered (20, 21). In contrast to the ordinary SIR on RH transmission line sections, the advanced structure provides the possibility of changing the resonant frequency of higher modes by using different dispersion characteristics of the RH and LH transmission lines even in the case of the same characteristic impedance of the TL sections. Since the LH TL can be realized as the lumped element equivalent of the LH TL only, such design makes it possible to decrease the resonator dimensions drastically, just in the case of using the RH TL part of the resonator made as a distributed TL section.

The ratio of the characteristic impedances $Z_{RL} = Z_R/Z_L$ and the electrical lengths of the transmission line sections θ_R and θ_L are considered variable parameters of the SIR. These parameters can be found from equations for the fundamental resonance at the frequency ω_0 ($n = 1$) and for the first spurious resonance at ω_1 ($n = 2$):

$$\tan(\theta_{0L}) = -Z_{RL}\cot(\theta_{0R}) \tag{42}$$

$$\tan\left(\theta_{0L}\frac{\omega_0}{\omega_1}\right) = Z_{RL}^{-1}\tan\left(\theta_{0R}\frac{\omega_1}{\omega_0}\right) \tag{43}$$

Here θ_{0R} and θ_{0L} are the electrical lengths of RH and LH TL sections at the fundamental resonant frequency ω_0.

In line with equations 42 and 43, the shorter the length of the RH TL section, the higher the resonant frequency ω_1. At the same time, the higher the ratio Z_R/Z_L, the higher ω_1 and the more effective the suppression of the higher harmonics. This is illustrated by Figure 10 with the results of simulation of the SIR with different values of the length of the RH TL section ($f_0 = 1.75$ GHz).

The open-ended lumped element SIR based on a cascaded connection of RH and LH TL sections is shown in Figure 11b. The resonator has the R-L-R structure with T-type of the RH TL section and Π-type of the LH TL section. The characteristic impedance and electrical length of each section is defined by the LC-parameters. For the simulation of scattering parameters, the small coupling capacitances $C1$ on input and output of the resonator have been introduced. The transmission characteristic with three resonance responses for $n = -1$, $n = 0$, and $n = +1$ is presented in Figure 11a. In case of the SIR designed on lumped elements, the number of resonances is limited and only three resonances exist for the resonator under consideration. In general, the number of resonances depends on the number of L- and C-components and on the manner of their connections.

Microwave Resonators Based on Composite Right/Left-Handed (CRLH) TL Sections

As in the case of a cascaded connection of RH/LH TL sections, a lumped equivalent of the CRLH TL section

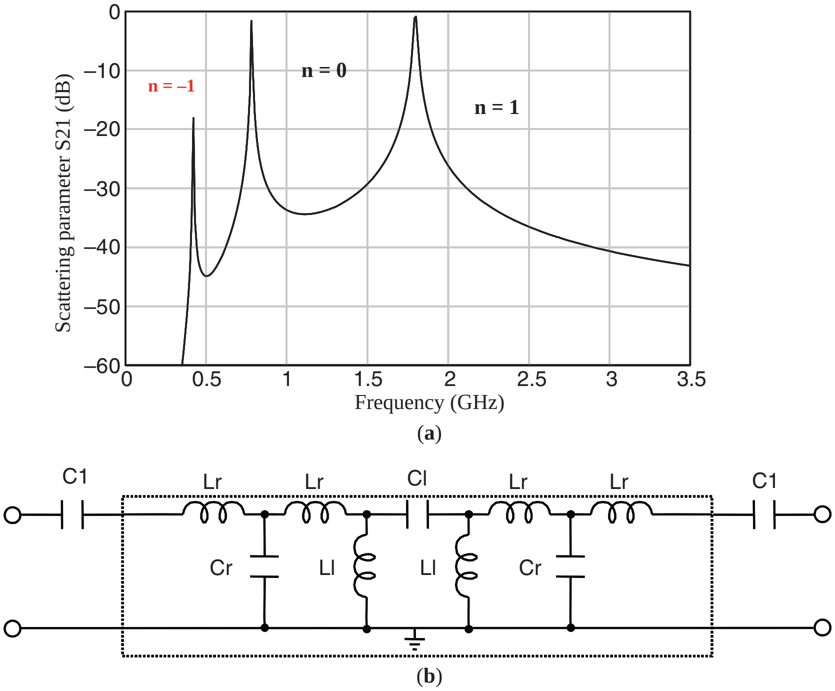

Figure 11. Equivalent diagram of the (a) R-L-R resonator and the (b) resonant frequency spectrum.

can be used for a resonator design in the frequency range far from the cut-off frequencies. The resonance condition corresponds to the same as that formulated in the previous case: The electrical length of the resonator is equal to the integer number of π (see equation 37). The electrical length of one unit cell of CRLH is defined by the propagation constant β in the TL (11):

$$\beta(\omega) = s(\omega)\sqrt{\omega^2 L_R C_R + \frac{1}{\omega^2 L_L C_L} - \left(\frac{L_R}{L_L} + \frac{C_R}{C_L}\right)} \qquad (44)$$

where

$$s(\omega) = \begin{bmatrix} -1 & for & \omega < \omega_1 = \min(\omega_1, \omega_2) \\ +1 & for & \omega > \omega_2 = \min(\omega_1, \omega_2) \end{bmatrix} \qquad (45)$$

For the balanced case, equation 45 is written as

$$\beta(\omega) = \beta(\omega_0)\left(\frac{\omega}{\omega_0} - \frac{\omega_0}{\omega}\right) \qquad (46)$$

where

$$\omega_0 = \frac{1}{\sqrt{L_R C_L}} = \frac{1}{\sqrt{L_L C_R}} \qquad (47)$$

is the resonant frequency of the series and shunt tanks in the CRLH TL unit cell.

The dispersion diagram of the CRLH TL resonator is shown in Figure 12a. The voltage distribution along the open-circuited resonator for seven resonances corresponding to the numbers $n = 0, \pm 1, \pm 2$ is depicted in Figure 12b. As in the case of resonators on a combination of RH and LH TL sections, the most interesting case is the zeroth-order resonance with $n = 0$ and homogeneous voltage distribution along the resonator.

An example, the characteristics of a CRLH TL resonator are shown in Figure 13a. The resonator is performed as a

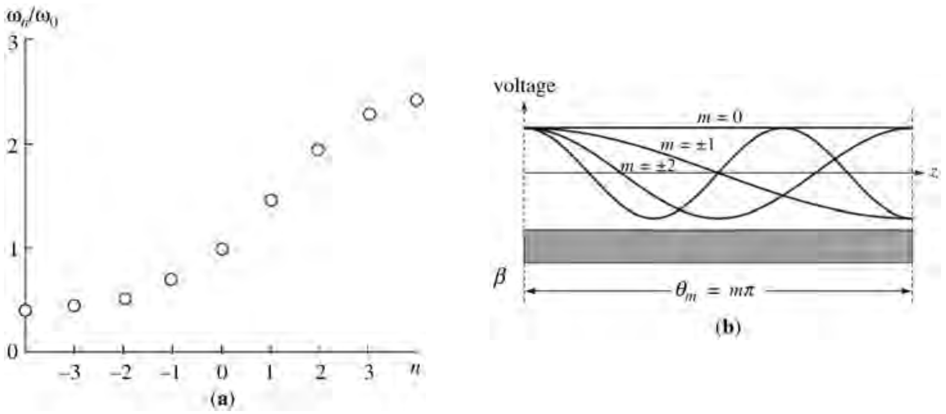

Figure 12. CRLH TL resonator (ideal homogeneous TL case): (a) normalized resonant frequencies for different n and (b) voltage distribution of the resonance modes for the case of an open-circuited CRLH TL resonator.

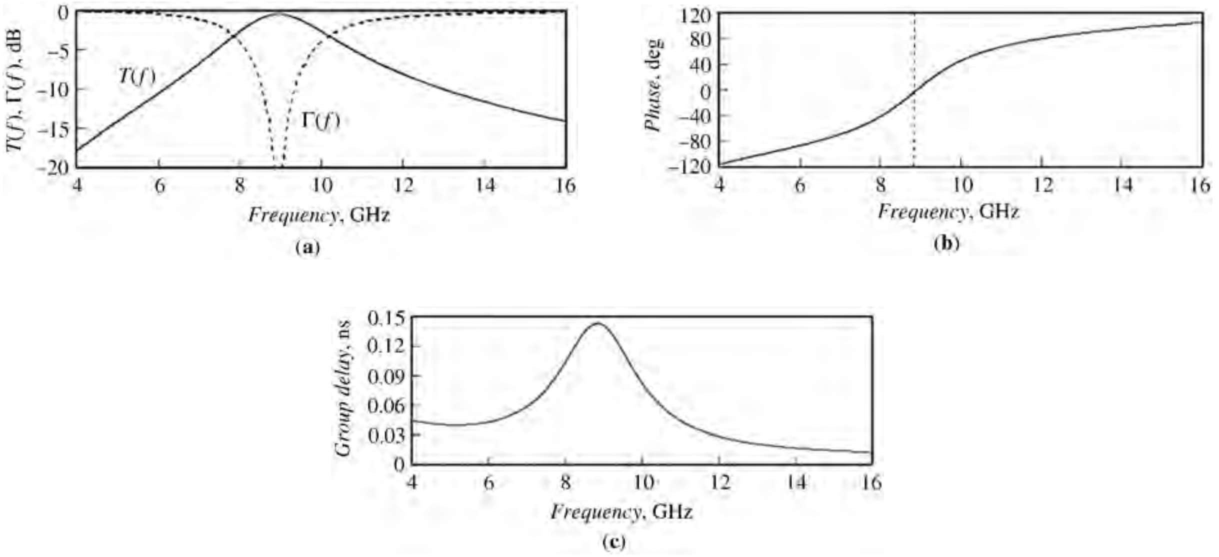

Figure 13. Characteristics of resonator on the CRLH TL implemented by two cascaded unit cells, (a) the zeroth-order resonance characteristic with $f_0 = 9\,\text{GHz}$, (b) phase response, and (c) group delay versus frequency.

cascaded connection of unit cells shown in Figure 6 consisting of series interdigital capacitors and grounded inductances with parasitic grounded capacitors of the inductance strips and parasitic inductances of the fingers of the interdigital capacitors. The open-ended resonator is connected with the external circuits by small capacitances. The resonator exhibits a set of resonances. The number of resonances is $2N - 1$, where N is the number of unit cells. In Figure 13a, the simulated resonance frequencies for open-ended resonator (balanced case) are presented.

Dual-Mode Resonator on a Cascaded Connection of RH/LH TL Sections

Another actual problem is a design of a dual-mode resonator for band-pass filter applications (25–28). Using the RH/LH SIR for this purpose is beneficial. Let us consider the main approach to the design of a dual-mode resonator as a cascaded connection of the LH TL and RH TL sections. At the same time, the problem of suppression of higher harmonics in the resonator should be taken into consideration. The dual-mode resonator can be designed using three unit cells shown in Figure 8. Different combinations of the unit cells may be used: L-R-L or R-L-R, T-Π-T or Π-T- Π, etc. The number of cells $N > 2$ also can be arbitrarily selected. For the open-ended resonator, the characteristics of the TL sections can be estimated for any arbitrary pair of resonant frequencies solving the system of equations 38–41. The *LC* components of the unit cells are to be found using equations 33–36.

Let us consider an example of a dual-mode resonator design. The equivalent diagram of the R-L-R resonator (Figure 14) is used as the dual-mode resonator with suppressed higher spurious responses. The frequencies ω_0 and

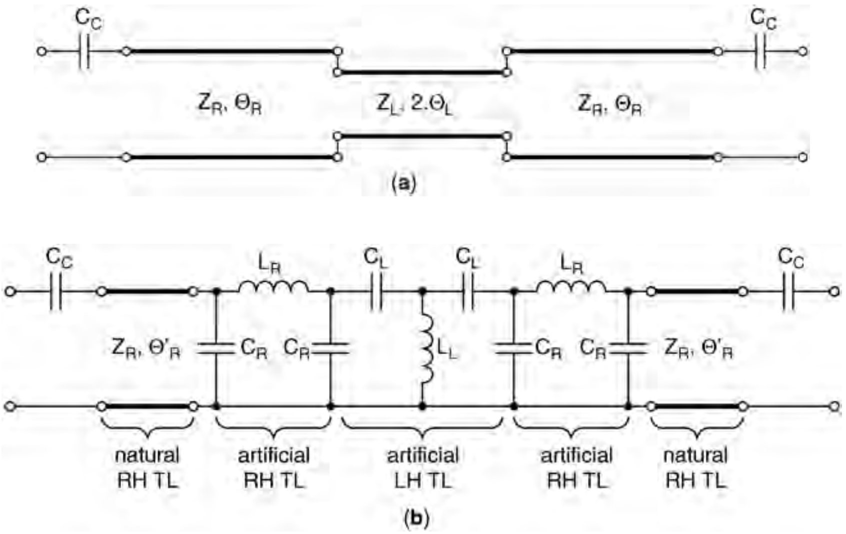

Figure 14. Equivalent diagram of the dual-mode resonator based on a combination of RH and LH TL sections.

ω_1 correspond to the lower and the higher resonant response of the resonator, respectively. To decrease the resonator dimensions, the RH TL is designed as a cascaded connection of a Π-section of an RH TL and a distributed TL section. As an example, the RH TL section of θ'_R electrical length and with the characteristic impedance Z_R was used in combination with the lumped element symmetric Π-section. The LH TL section is designed as the T-section (Figure 14). The structure of the dual-mode resonator designed for the resonant frequencies 2 and 3 GHz is presented in Figure 15 (20, 29). The advanced multilayer ceramic technology (low-temperature cofired ceramics, LTCC) was used for the resonator fabrication (30, 31). Grounded capacitances C_R are realized as parallel-plate capacitors. Series coupling capacitances C_L are produced by overlaying electrodes of the capacitors placed in different layers. Turned stacked inductors L_R and L_L are used. The natural RH TL section is realized as a microstrip TL section with the corresponding characteristic impedance and electrical length. The test structure of the resonator was fabricated using eight layers of the 95-μm-thick LTCC DuPont Green Tape$^{\text{TM}}$ 951 ($\varepsilon_r = 7.8$, $\tan\delta = 0.002$ at 2 GHz) (29). For the metallization layer deposition, the silver ink DP6145 was used. The fired thickness of the metallization layer is 9–11 μm. The resistivity is less than 6 mOhm/□. The paste was printed using 400-mesh metal screens with 15-μm film coating. The size of the LTCC multilayer substrate is $22 \times 20 \times 0.76\,\text{mm}^3$, whereas the actual area occupied by the dual-mode resonator is $10 \times 8\,\text{mm}^2$.

The results of electromagnetic (EM) simulation of the dual-band SIR using Sonnet 10.52 Software are shown in Figure 15 in comparison with the measured data (Hewlett-Packard 8510C Network Analyzer) for the five tested structures. In a wide frequency range, the spurious response is not observed up to 8 GHz.

Microwave Filters Based on RH/LH TL Sections (Examples of Design)

The possibility of controlling arbitrarily the resonant frequency of the first and second modes of the SIR designed as cascaded RH and LH TL sections can be successfully considered for a design of miniature dual-band filters. The dual-band filter designed on the R-L-R SIRs described in the previous section and implemented in the LTCC package is shown in Figure 16 (20, 29, 31). The performance of the filter is presented in Figure 16c. The filter bandwidth is 150 MHz for the operational frequencies $f_1 = 2$ GHz and $f_2 = 3$ GHz, which are nonmultiple. The simulated and measured return loss is better than 20 dB and 16 dB for the frequencies f_1 and f_2 correspondingly. The measured isolation between the operational pass bands is better than 20 dB. The measured insertion loss is not higher than 2.3 dB at f_1 and 3.6 dB at f_2. In the wide

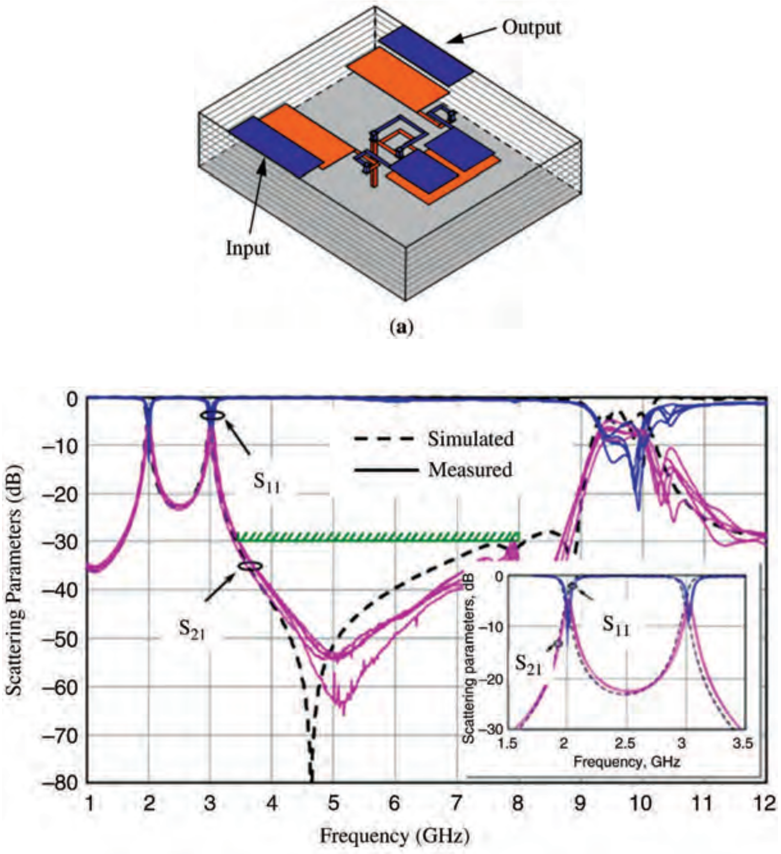

(a)

(b)

Figure 15. Two-mode resonator with a highly suppressed spurious response: (a) the multilayer structure of the resonator and (b) scattering parameters versus frequency.

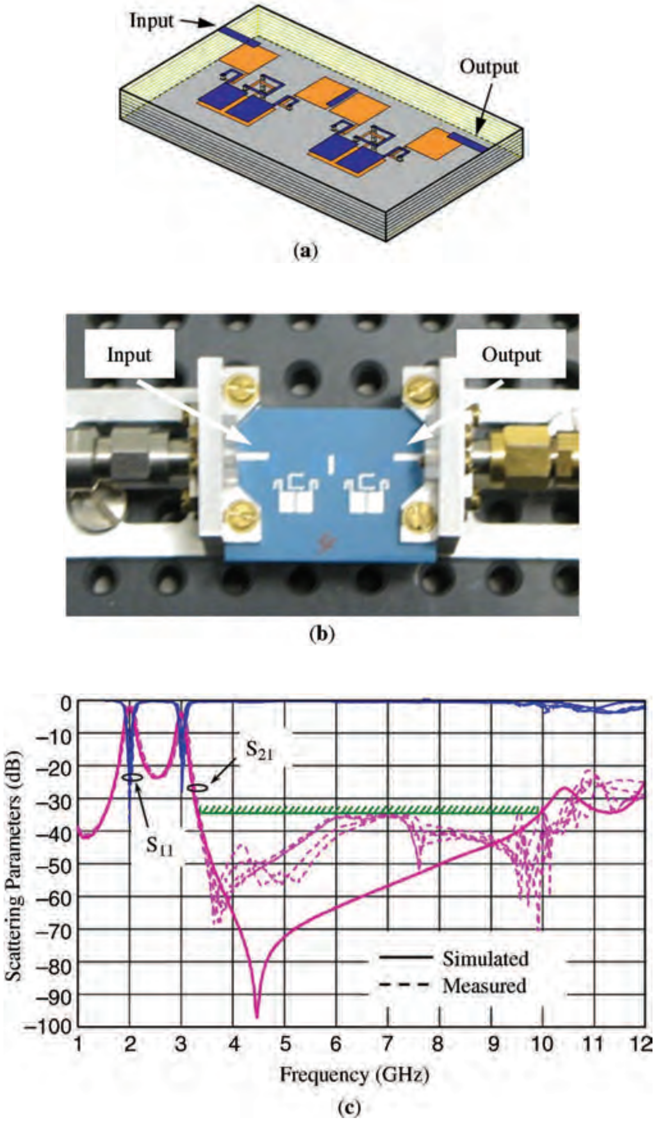

Figure 16. Two-pole filter on the resonators (Figure 15): (a) LTCC implementation of the filter; (b) photo of the filter; and (c) transmission (S_{21}) and reflection (S_{11}) characteristics for five test samples. The area occupied by the filter is $20 \times 8.5\,\text{mm}^2$.

frequency range shown in Figure 16c, the spurious response is not observed up to 10 GHz.

Another possibility for designing a dual-band filter is using the dual-band property of CRLH TLs (27, 32). Much more effective is using a generalized CRLH transmission line, which is an extension of the original transmission line (Figure 5a) (33–36). The unit cell of the generalized CRHL TL is presented in Figure 17. While a CRLH TL has one controllable left-handed (supporting a backward wave) and one controllable right-handed (forward wave) pass band, a generalized CRHL TL exhibits two controllable left-handed and right-handed pass bands. This line can be used for a design of a dual-band band pass filter. The generalized CRHL TL has eight distinct circuit elements (four inductors and four capacitors) as shown in Figure 17. These elements are arranged to create four distinct *LC* resonators.

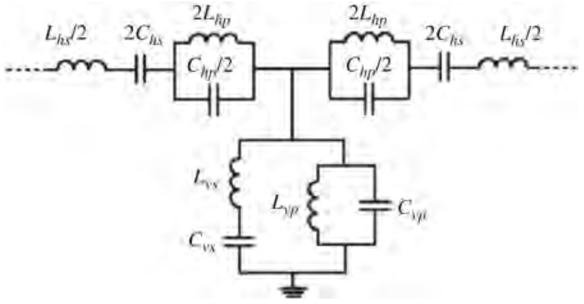

Figure 17. The unit cell of the generalized CRLH TL. From Reference 36; copyright © 2010 IEEE, reprinted with permission conveyed through Copyright Clearance Center, Inc.

The filter synthesis of the dual-band filters is based on the prototype low-pass filter. From this approach, it is possible to transform a low-pass response to a monoband band pass filter through well-known equations. An additional transformation is applied to obtain a dual-band response. The required transformation is as follows (36):

$$\omega = \frac{\omega_0}{\omega'}\left(\frac{\omega'}{\omega_0} - \frac{\omega_0}{\omega'}\right) \tag{48}$$

$$\omega' = \frac{\omega_2 - \omega_1}{\omega_0}, \quad \omega_0 = \sqrt{\omega_1 \omega_2} \tag{49}$$

with ω being the frequency of the dual-band band pass filter and ω_1 and ω_2 the angular central frequencies of the first and second filter bands, respectively.

An example of the dual-band filter on a generalized CRLH TL section is shown in Figure 18 (14). In planar technology, the series resonator of the series and shunt branches can be implemented by means of an open split ring resonator (OSRR, Figure 18a). The parallel resonator of the shunt branch was realized by means of an open complementary split ring resonator (OCSRR, Figure 18b) (37), and the parallel resonator of the series branch was implemented by parallel connecting a capacitive patch and a meander inductor. All these resonators are electrically small. The dual-band filter was fabricated on the *Rogers RO3010* substrate with thickness $h = 0.254\,\text{mm}$ and the dielectric constant $\varepsilon_r = 10.5$ is $19.5 \times 13.5\,\text{mm}^2$, which corresponds to $\lambda_g/4.5 \times \lambda_g/6.6$ with λ_g being the guided wavelength at f_0. The simulated and measured characteristics of the filter are presented in Figure 19.

CRLH TLs can be also effectively used for ultra-wideband (UWB) filter design. For this purpose, a traditional CRLH-TL (5) can be used. The filter equivalent circuit is shown in Figure 20a. With this circuit, it can be easily seen that, due to the high-pass nature of LH elements (C_l and L_l) and the low-pass nature of the RH elements (C_r and L_r), a band pass response is produced. The filter response can be further improved if an additional transmission zero is produced at the upper stop band. To achieve this, a coupling capacitor C_0 between input and output ports is introduced (Figure 20b) (38). The final circuit simulation result is shown in Figure 20c (solid lines) in comparison with the result obtained without the coupling capacitor (dashed lines). It can be seen that the circuit efficiently produces a UWB response with additional transmission zero in the upper stop band. Only six elements and a

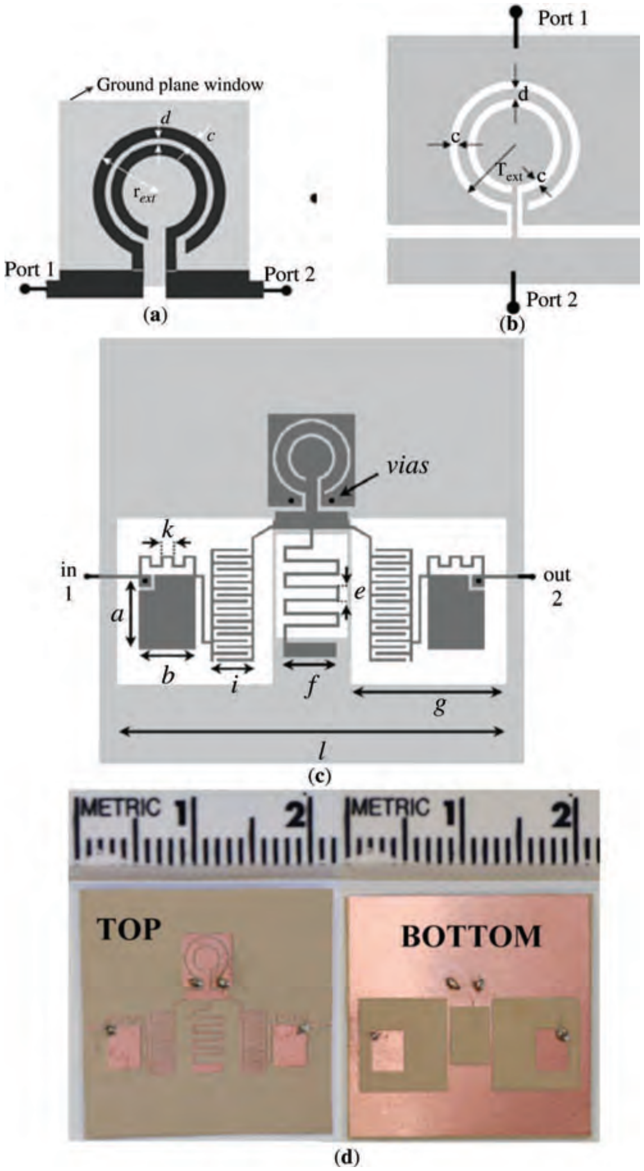

Figure 18. Structures of OSRR (a) and OCSRR (b) (37). Layout (c) and photograph (d) of the dual-band filter. From Reference 36; copyright © 2010 IEEE, reprinted with permission conveyed through Copyright Clearance Center, Inc.

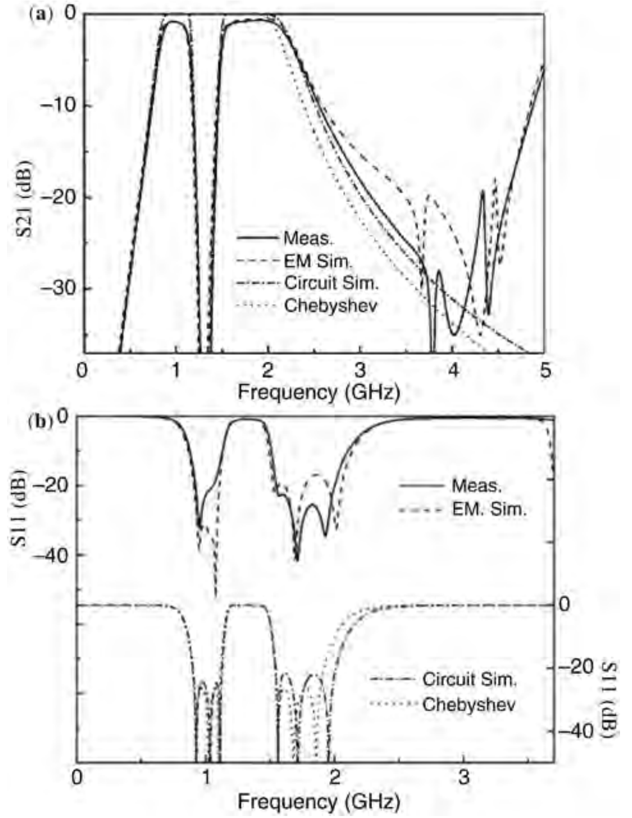

Figure 19. Scattering parameters of the dual-band filter on a generalized CRLH TL section. From Reference 36; copyright © 2010 IEEE, reprinted with permission conveyed through Copyright Clearance Center, Inc.

capacitive coupling are used. This leads to a compact physical implementation, which is being carried out using printed circuit board (PCB) or other multilayer technologies. The filter was fabricated using the liquid-crystal-polymer (LCP) technology (39). The multilayer structure of the filter consists of five layers of Rogers ULTRALAM® 3000 series ($\varepsilon_r = 3$, $\tan\delta = 0.0025$). The LCP implementation of the filter is presented in Figure 21a. The filter area is $13 \times 10\,\mathrm{mm}^2$, which corresponds to the linear dimensions of 0.4 λ_g at the central frequency f_0 (λ_g is the guided wavelength at f_0). The photograph of the filter is shown in Figure 21b, and its experimental performance is demonstrated in Figure 21c. The measured in-band insertion loss is less than 0.5 dB, and in-band return loss is better than 15 dB. The performance of the UWB filter can be improved by including resonant components between input and output for realization of additional transmission zeros (40).

Another approach based on using CRLH loaded with SRR is useful for a design of UWB filters (41). The key point to achieve the wideband or the UWB filter is the design of balanced cells, where the transition between the left- and the right-handed bands is continuous.

A band pass filter is based on a balanced line loaded with complementary split ring resonators, series gaps, and grounded stubs. This hybrid approach provides a further degree of flexibility due to the presence of additional elements (i.e., grounded stubs acting as shunt connected inductors). For the hybrid approach, the wide bands can be allocated either below or above the typical transmission zero, intrinsic to the presence of complementary split ring resonators.

The layout of the hybrid left-handed cell and its corresponding lumped-element equivalent-circuit model are depicted in Figure 22a. In the topology, two series gaps are included and shunt stubs are grounded through metallic vias, which are described as a shunt connected inductance.

The fabricated filter is depicted in Figure 23a. Four unit cells have been enough to achieve the required rejection at 2 GHz. The rings are etched on the bottom layer. The dashed rectangle has an area of $1\,\mathrm{cm}^2$. The dimensions of the structure components are as follows: the line width $W = 0.126$ mm, external radius of the outer ring $r =$

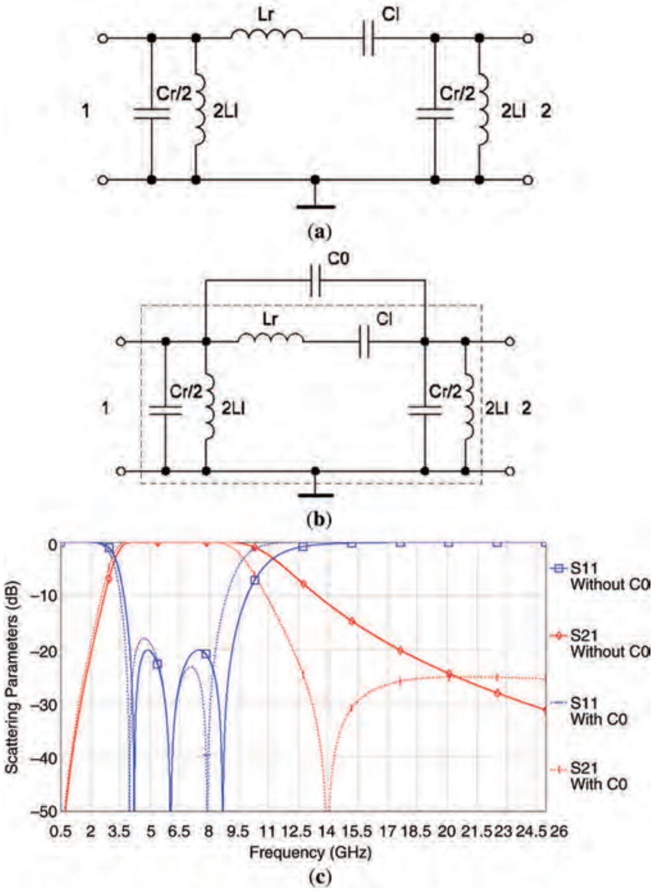

Figure 20. UWB filter on CRLH TL section: (a) equivalent diagram, (b) equivalent diagram with additional coupling capacitor C_0, and (c) simulated UWB filter performance.

1.68 mm, the ring width $c = 0.32$ mm, and rings separation $d = 0.19$ mm; inductor width is 0.10 mm, and the distance between the electrodes forming the gap is 0.4 mm.

Figure 23b illustrates the simulated (by using Agilent Momentum) and measured (by means of the Agilent 8720ET Vector network analyzer) frequency response of the filter. Reasonable agreement between simulation and experiment has been achieved. The ripple level is slightly higher than 1 dB. This excess of ripple is attributed to fabrication-related tolerances. The combination of size and performance for this periodic filter is a relevant aspect to highlight. A very wide measured bandwidth (3.5–10 GHz) has been achieved with high selectivity at both band edges, and the first spurious response is observed at 17 GHz.

Many useful characteristic features have been demonstrated by filters based on CRLH TL sections and on combinations of RH and LH TL sections. Let us consider the narrow-band filter discussed in Ref. 42. A miniature band-pass filter having two transmission zeros placed on both sides of the pass-band skirt is shown in Figure 24. The filter design is based on the transversal signal-interference concept (43, 44) and consists of an LH TL section and an RH TL section connected in parallel, with characteristic impedances Z_R and Z_L and electrical lengths θ_R and θ_L, respectively. While compared with conventional transversal filters, the proposed structures would have the following advantages: First, the phase incursion along the LH-TL is positive, which corresponds to the negative electrical length, which is promising to replace a conventional transmission line of long electrical length $\theta = 270°$ by an equivalent of the LH TL section with $\theta = -90°$, thus, significantly reducing the size of the device. The artificial lines are realized as a lumped-element Π-section of LH TL and two T-sections of RH TL connected in series. Additionally, the high-pass nature of lumped element LH TL and the low-pass nature of RH TL provide a good asymmetrical out-of-band response with two transmission zeros on two sides of the operational pass band. The filter was realized using LCP technology and fabricated on a five-metal layer by using three types of LCP films: 100-μm-thick LCP core film and 50-μm- and 25-μm-thick LCP bonding film. The

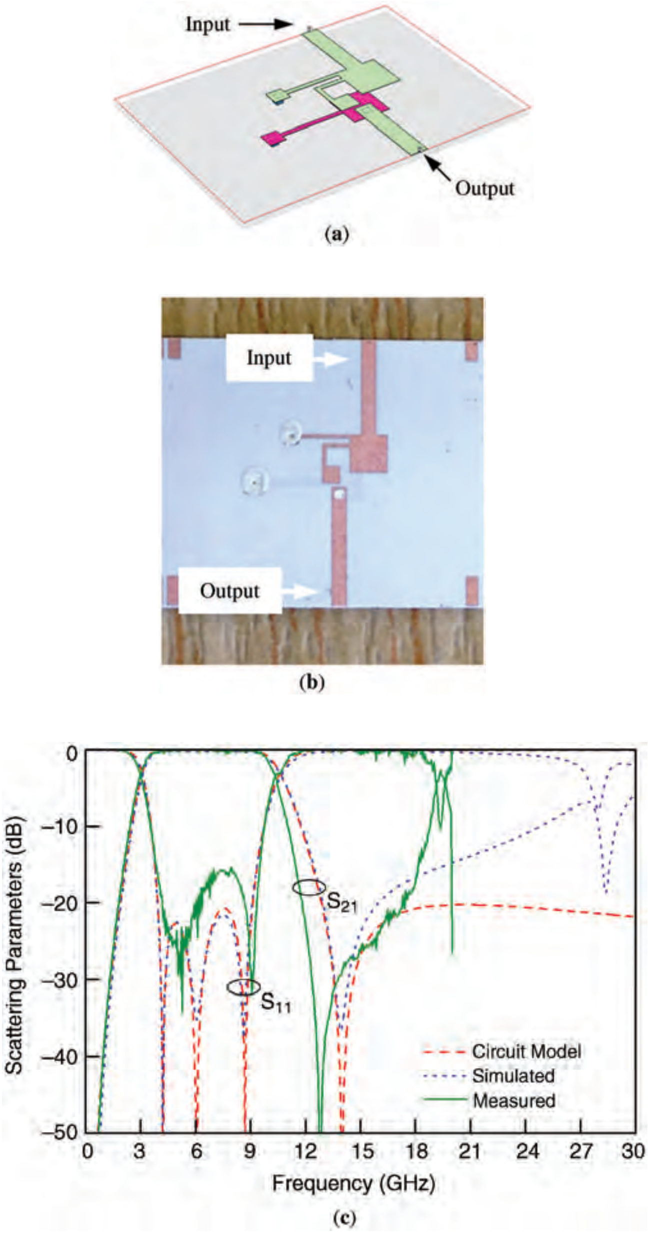

Figure 21. LCP implementation of the (a) UWB filter, (b) photograph of the filter, and (c) the filter performance.

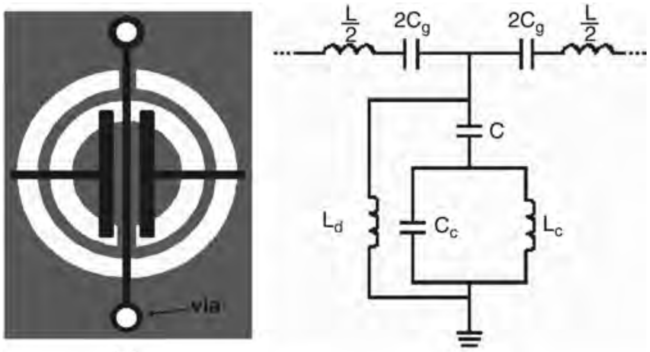

(a) (b)

Figure 22. Topology of the (a) hybrid left-handed cell and (b) its equivalent circuit. Ground plane metal is depicted in gray; the upper metal level is depicted in black. From Reference 41; copyright © 2007 IEEE, reprinted with permission conveyed through Copyright Clearance Center, Inc.

filter structure is presented in Figure 25a. The transmission and reflection coefficients as functions of frequency are shown in Figure 25b. The fabricated filter is measured using an HP8510 vector network analyzer and an Anritsu Test Fixture. The high performance of the filter with two transmission zeros is achieved. The filter has the center frequency at 2.06 GHz and a 3-dB bandwidth of 24%. The measured in-band insertion loss is about 1.5 dB. The transmission zeros are located at 1.69 GHz and 3.26 GHz, respectively. The photograph of the filter is shown in the inset to Figure 25b. The size of the filter is $5.8 \times 4.8\,\mathrm{mm}^2$, excluding the input and output microstrip lines.

Using a metamaterial transmission line approach makes it possible to design advanced microwave frequency selective miniature devices exhibiting useful properties.

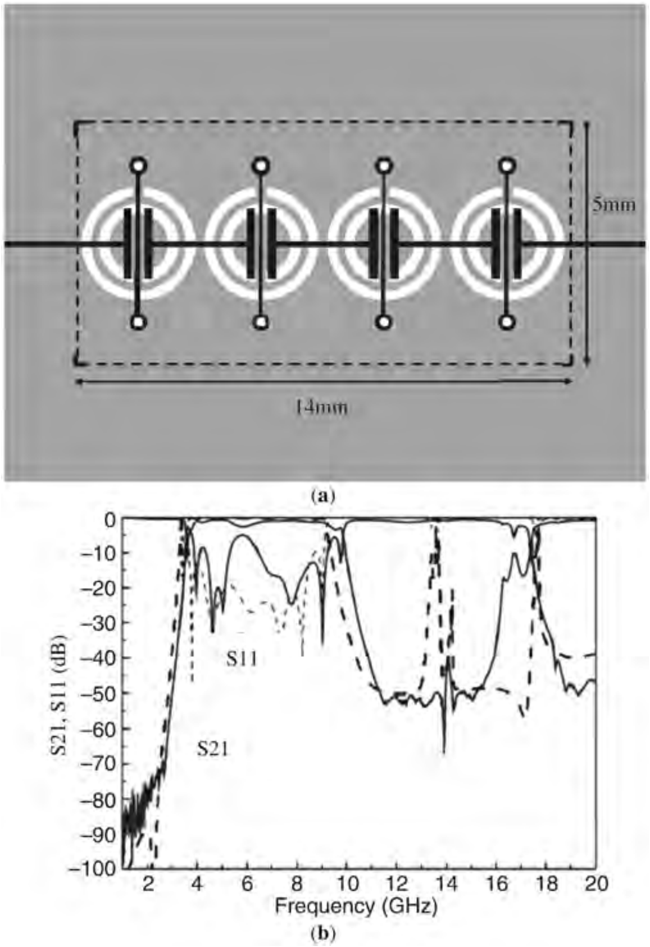

Figure 23. Layout of the filter formed by cascading (a) four balanced hybrid cells and (b) its performance: simulated (dashed lines) and measured (solid lines). From Reference 41; copyright © 2007 IEEE, reprinted with permission conveyed through Copyright Clearance Center, Inc.

DIRECTIONAL COUPLERS AND POWER DIVIDER-COMBINERS ON METAMATERIAL TRANSMISSION LINES

Directional couplers and power dividers are important components of many RF and microwave systems. They are widely used in many power splitting networks. Design of these devices on a combination of RH TL and LH TL sections or on CRLH TL sections makes it possible to improve their performance and enrich functionality. The most important feature of the LH and RH TLs is that their dispersion characteristics are described by different equations. That can be used for many beneficial applications for a design of a microwave directional couplers demonstrating improved functionality of these devices accompanied by their miniaturization. The most interesting achievements are the following: (1) decreasing drastically device dimensions; (2) achievement of a desired phase difference for output signals: 0°, ±90°, ±180°; (3) widening the operational frequency range; and (4) design of dual-band devices.

Miniature Branch-Line Directional Coupler

A conventional branch-line directional coupler is usually designed as a symmetric structure consisting of quarter-wavelength TL sections (Figure 26a). At the same time, the branches forming the directional coupler can be designed as artificial RH and LH TL sections. Taking into consideration that the electrical length of the branches is $\theta = \pm 90^\circ$, the lumped-element equivalent T- and Π- unit cells presented in Figure 27 can be formally used as the branches of the coupler. In practice these cells are used in filter design as impedance and admittance inverters. As an example, a suitable version of the equivalent circuit of the branch-line directional coupler is shown in Figure 26b. The horizontal branches are the RH TL sections in a form of the Π-circuit (Figure 4b), whereas the vertical ones are designed as the LH TL sections (impedance inverter, Figure 27d). Negative capacitances of the impedance inverters have been absorbed by the positive capacitances of the RH TL sections. The final equivalent circuit is shown in Figure 26c and seems to be the optimal one for practical implementation because of containing only two inductances and having reduced grounded capacitors. The performance of the device equivalent circuit is nearly the same as it is obtained for the commonly used distributed version (Figure 26a).

In general, the values of the LC-parameters depend on a desired coupling rate of the directional coupler, which is provided by the corresponding characteristic impedances

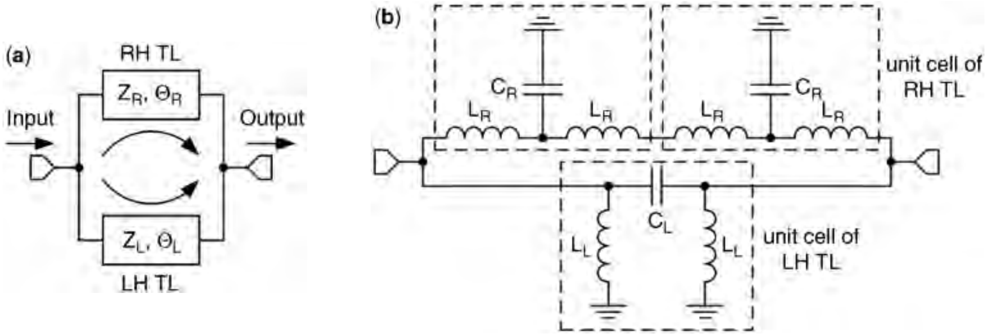

Figure 24. Band-pass filter based on (a) signal-interference concept; equivalent circuit of the filter on (b) artificial RH and LH TL sections.

of the branches. The miniature 3-dB directional coupler (known as a hybrid junction) for the operational bandwidth of 2.4–2.5 GHz was designed by means of multilayer LTCC technology (45, 46). The device was accomplished in five layers of DuPont Green Tape^{TM} 951 LTCC with layer thicknesses of 42 μm and 210 μm. The 10-μm-thick conductive layers have been screen-printed using DuPont 6142 silver paste. The multilayer LTCC structure of the 3-dB DC is shown in Figure 28a. Two ground planes covering the multilayer structure are connected to each other via holes situated along the external perimeter of the structure (not shown in Figure 28a). The quasi-lumped parallel plate capacitors and two-turn stacked inductors situated in two conductive layers have been used. Grounded capacitors were realized as parallel-plate capacitors between the inner conductive patterns and the ground planes. Series capacitors were produced by overlapping the electrodes of the grounded capacitors. The size of the hybrid junction is $5.2 \times 3.0\,\text{mm}^2$ corresponding to $\lambda_g(f_0)/12 \times \lambda_g(f_0)/20$ in terms of guiding wavelength.

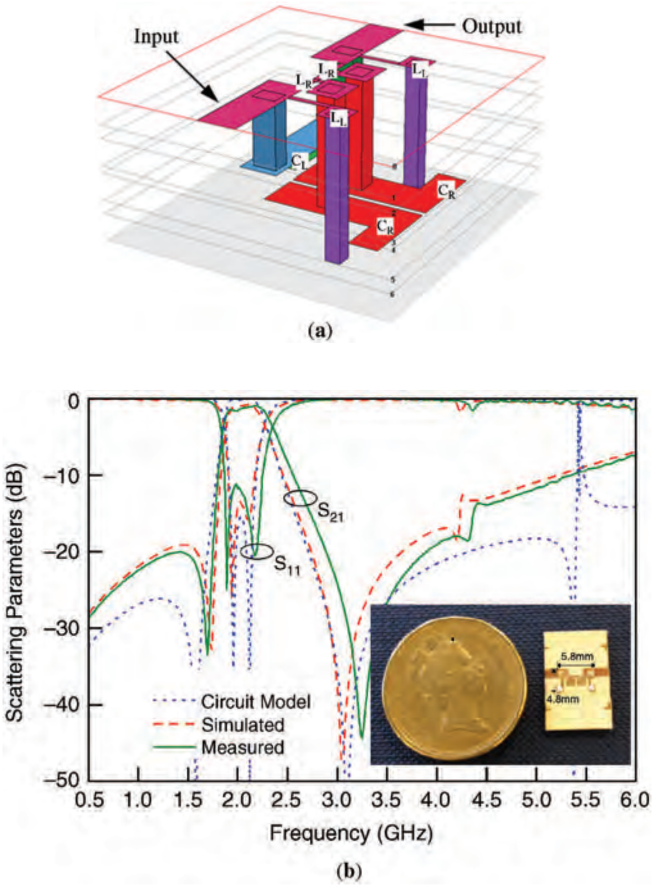

Figure 25. LCP-structure of the (a) two-pole filter and the (b) filter performance.

The results of experimental investigation carried out using Agilent E8631A PNA Network Analyzer (10 MHz–67 GHz) are shown in Figure 28b. At the center frequency 2.45 GHz, the device provides the required power division (3 dB) between output ports 2 and 3. In the frequency range 2.4–2.5 GHz, the measured return loss is better than 20 dB and the isolation is not less than 20 dB. The insertion loss does not exceed 0.3 dB, the amplitude unbalance is not worse than ±0.5 dB, and the phase difference between the signals in output ports is $90 + 5^\circ$.

Miniature Rat-Race Ring

A schematic diagram of a conventional rat-race ring is shown in Figure 29a. According to the procedure described earlier, the distributed TL section with the electrical length of 270° can be replaced by an artificial RH TL consisting at least of three T- or Π-cells. On the other hand, the 270° RH TL can be substituted by an LH TL with the electrical length of −90°.

Figure 29b shows the equivalent circuit of a rat-race ring with 270° TL section replaced by the −90° artificial LH TL, which has been implemented as a single Π-cell (Figure 4d). Three 90° TL sections have been realized as the Π-cells of RH TL (Figure 4b). The resonant frequency of parallel tanks formed at ports 1 and 4 is equal to the central frequency ω_0 of the device and, consequently, can be removed from the equivalent circuit without any change of characteristics at the central frequency ω_0. The final equivalent diagram of the rat-race ring under consideration is presented in Figure 29c.

Figure 30a presents a coplanar waveguide (CPW) implementation of the rat-race ring using an equivalent circuit shown in Figure 29c. The device has been designed as multilayer LTCC integrated circuits using eight layers of 92-μm-thick DuPont Green Tape^{TM} 951 LTCC (45, 47). In the design, quasi-lumped parallel-plate capacitors and two-turn stacked inductors are used as in the case of the 3-dB directional coupler. The dimension of the device

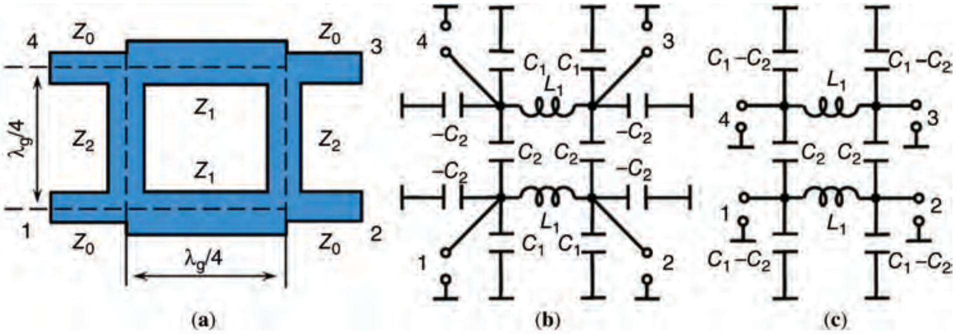

Figure 26. Branch-line 3-dB directional coupler: (a) traditional structure, (b) LC-equivalent circuit presentation, and (c) simplified LC-circuit.

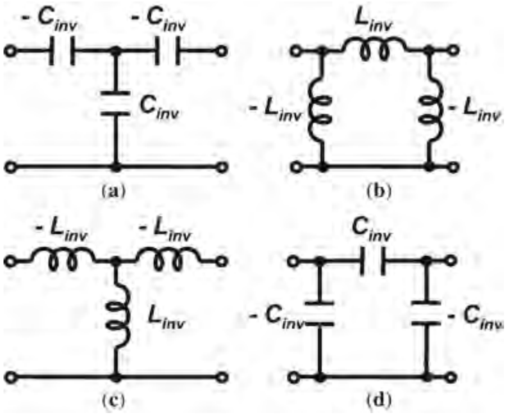

Figure 27. Lumped-element equivalent T- and Π-cells of the (a and b) RH TL and (c and d) LH TL sections of electrical length $\theta = \pm\frac{\pi}{2}$ containing negative values of capacitors C_{inv} and inductances L_{inv}.

designed for the central frequency of 2.45 GHz is $7.5 \times 7.5\,\text{mm}^2$, corresponding to electrical dimensions of about $\lambda_g(f_0)/8 \times \lambda_g(f_0)/8$.

The scattering parameters of the rat-race ring directional coupler measured with an HP 8510C vector network analyzer are presented in Figure 30b in comparison with the simulated results. In the frequency range 2.2–2.7 GHz, the device provided an equal power division with the amplitude unbalance of less than ±1 dB. The measured insertion loss is better than 0.2 dB at the central frequency. The measured return loss and isolation are better than 20 dB. The phase difference between the output signals is 180° −1°/+7°.

Dimensions of the rat-race ring directional coupler on RH LH TL sections in line with the equivalent diagram can be further decreased using optimized designs and additional possibilities of the multilayer LTCC technology (48, 49). The strip-line version of the rat-race ring using the ceramic layers of different thickness manufactured on Dupont Green Tape 951 LTCC (1 layer of thickness $d = 43\,\mu\text{m}$ and six layers of $d = 210\,\mu\text{m}$ with the same dielectric constant $\varepsilon_r = 7.8$) was designed as a module with dimensions $3.8 \times 3.8 \times 0.21\,\text{mm}^3$. The linear size of the device is estimated as $< \lambda_g(f_0)/16$. The following performance of the strip-line rat-race ring is as follows: operational bandwidth 12%, insertion loss 0.28 dB, amplitude unbalance ±0.7 dB, return loss and isolation >18 dB, and phase difference of signals in output ports 180° ± 7°.

The ultra-small version of the rat-race ring directional coupler was designed as a CPW structure with multiturn stacked inductances and miniature capacitors using a thin ceramic layer with a high dielectric constant $\varepsilon_r = 30$. The following Dupont Green Tape 951 LTCC layers have been used: one layer ($d = 13\,\mu\text{m}$, $\varepsilon_r = 30$) and six layers ($d = 210\,\mu\text{m}$, $\varepsilon_r = 7.8$). The dimensions of the module are $2.4 \times 2.4 \times 0.2\,\text{mm}^3$, which corresponds to the linear size $\lambda_g/24$. The LTCC structure of the miniature rat-race ring is presented in Figure 31a. The performance of the ultra-small directional coupler in Figure 31b demonstrates nearly

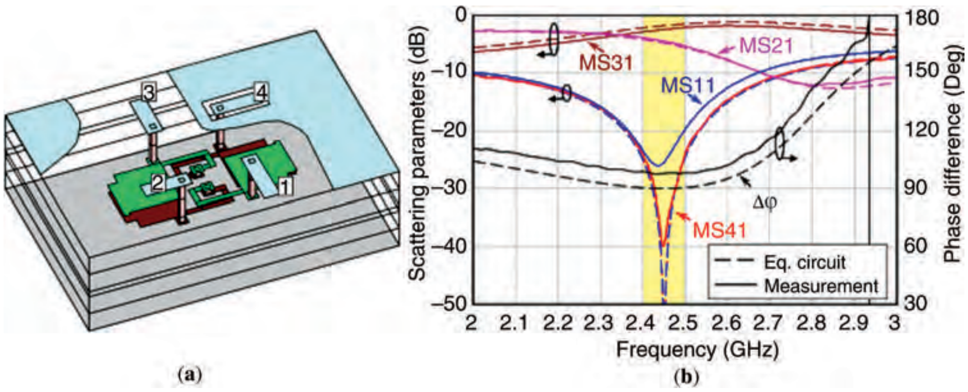

Figure 28. LTCC implementation of (a) 3-DB branch-line directional coupler and (b) its scattering parameters versus frequency.

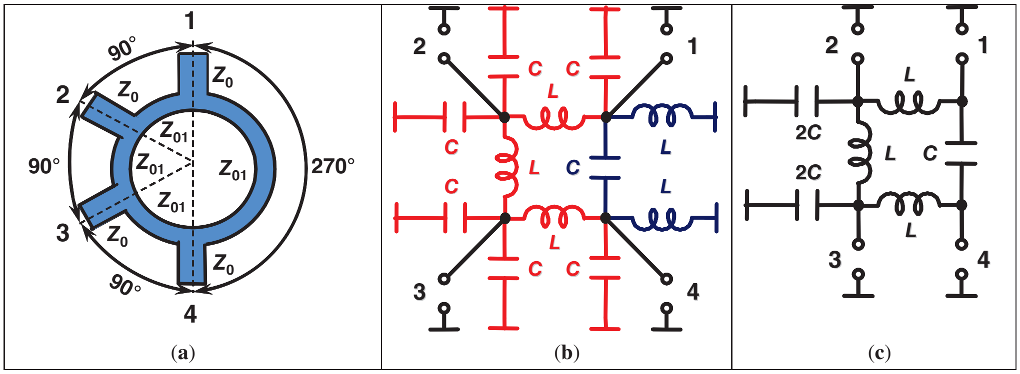

Figure 29. Rat-race ring: (a) conventional microstrip line design, (b) equivalent presentation by the Π-circuits, and (c) final equivalent circuit of the device on lumped elements.

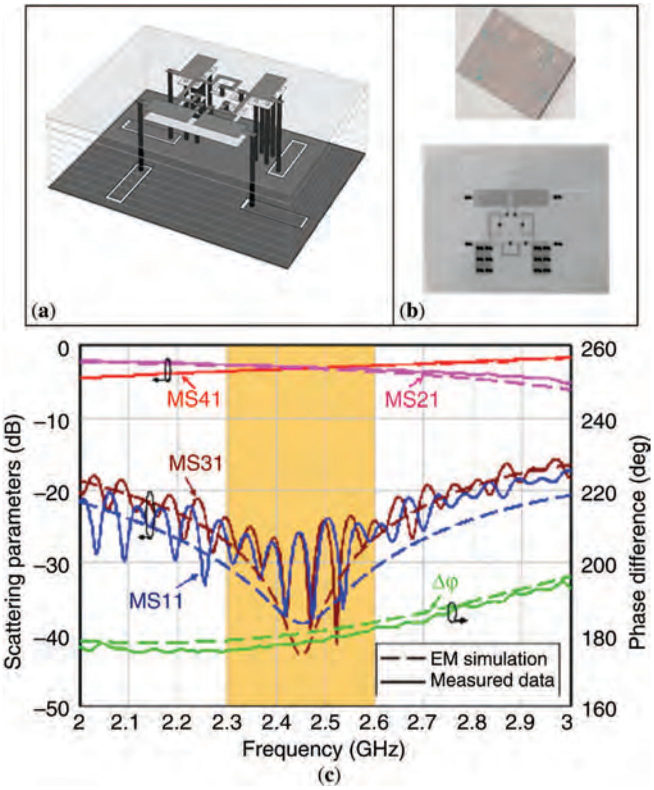

Figure 30. (a) Coplanar multilayer LTCC implementation of the rat-race ring, (b) photograph and EM image of the directional coupler, and (c) performance of the device.

the same parameters as compared with the previous versions: operational bandwidth: 20%, insertion loss: 0.4 dB, amplitude unbalance: ±1 dB, return loss and isolation: >15 dB, phase difference: 180° −5°. The dimensions of the designed directional couplers are shown in comparison in Figure 31c.

There is a possibility of broadening the operational frequency band of the rat-race ring directional coupler by using two unit cells of ±45° of length for the section design (Figure 32a) instead of one section (Figure 29b and c). The directional coupler is implemented in eight layers of Dupont Green Tape 951 LTCC ($d = 95\,\mu$m, $\varepsilon_r = 7.8$). The LTCC structure is presented in Figure 32b. The following characteristics have been observed (Figure 32c): operational bandwidth of 47%, amplitude unbalance of ±0.7 dB, return loss and isolation of more than 20 dB, phase difference of output signals of 180° +2°/−8°. The dimension of the device is $10 \times 8 \times 0.76\,\text{mm}^3$. So there is a trade-off between the rat-race ring dimensions and the width of the frequency band.

A small-size rat-race ring directional coupler can be also designed using traditional planar technology as applied to the structure based on artificial LH and RH TL sections implemented by means of SRR and CSRR (50–53). In microstrip technology, these artificial lines have been mainly implemented by using CSRR, which is a complementary structure with respect to traditional SRR and is manufactured by ring splits in ground plane. Figure 33 depicts the basic unit cells of the CSRR-based LH and RH lines. By combining CSRR with a series gap (etched above the positions of the CSRR) a LH transmission line results. Conversely, forward (RH) wave propagation arises in an artificial line where the CSRR is combined with grounded stubs. The CSRR-based artificial LH TL section with electrical length of −90° replaces the conventional 270° TL section in the rat-race ring directional coupler, with the result of a significant reduction in final dimensions. Both LH and RH TL sections based on CSRR are used for the design of a small-size rat-race hybrid coupler.

With the proposed design, a size reduction by a factor of 3 is achieved as compared with the conventional implementation. The operating frequency of the rat-race ring hybrid coupler has been set to $f_0 = 1.6$ GHz. The layout of the device is depicted in Figure 34a. In two RH lines, the grounded stubs have been etched in the inner region of the structure to save area, and they have been coiled to avoid overlapping. The photo of the device is shown in Figure 34b. The device has been fabricated on the Rogers RO3010 substrate with dielectric constant $\varepsilon_r = 10.2$ and thickness $h = 635\,\mu$m. The active area (excluding access lines) of the CSSR hybrid coupler based on LH and RH artificial lines is $3.62\,\text{cm}^2$, whereas the conventional one occupies the area of $10.33\,\text{cm}^2$; i.e., the device proposed in this work is roughly three times smaller. The simulated and measured impedance matching, coupling, and isolation for the CSRR directional coupler are depicted in Figure 34c.

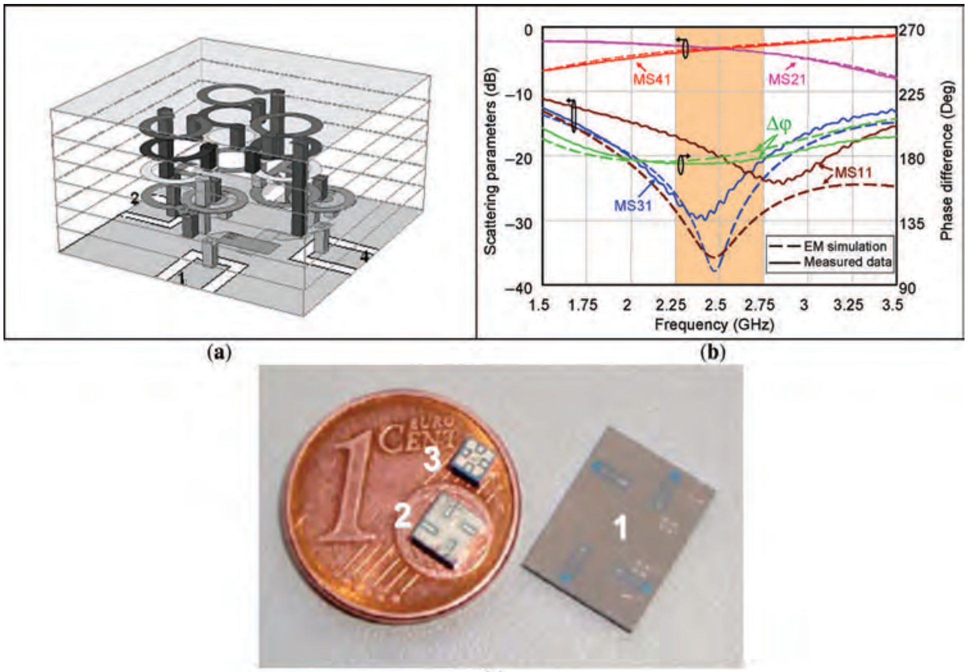

(a) (b)

(c)

Figure 31. Ultra-small rat-race ring: (a) LTCC implementation, (b) scattering parameters and phase difference in output ports versus frequency, and (c) comparison of dimensions of different versions of the rat-race ring: 1—miniaturized rat-race ring (CPW), $7.5 \times 7.5 \times 0.76\,\mathrm{mm}^3$ (<λg/8); 2—miniaturized rat-race ring (strip line), $3.8 \times 3.8 \times 0.21\,\mathrm{mm}^3$ (< λg/16), and 3—ultra small rat-race ring (CPW) $2.4 \times 2.4 \times 0.2\,\mathrm{mm}^3$ (<λg/24).

180° Broad-Band Wilkinson Power Divider-Combiner (Balun) Using a Combination of Artificial RH and LH TL Sections

The Wilkinson power divider-combiner (referred to as the "Wilkinson power divider" from here on) is a very popular microwave device employed in various power distribution networks (Figure 35a). It is well known that the output signals of the classic Wilkinson power divider are in phase. For some practical applications, a Wilkinson power divider with an output phase difference of 180° (balun) looks very useful. The first realization of a 180° Wilkinson power divider was reported in Ref. 54. The 180° Wilkinson power divider proposed there employs external LH and RH TL phase-shifting sections with the electrical length of −90° and +90°, respectively, connected with the output arms of the classic power divider (Figure 35b). Such a divider configuration is very useful when the impedance transformation is required along with the 180° phase shift. The architecture of the Wilkinson balun is presented in Figure 36a. The input feed line was designed with a characteristic impedance of 50 Ohms, while the two λ/4 branches were designed with a characteristic impedance of 70.7 Ohms, resulting in a resistor value of 100 Ohms. A five-stage design was chosen for the +90° phase-shifting line, with an initial host TL unit cell. To achieve a phase advance for a positively traveling plane wave of the form $e^{-j\theta_L}$, θ_L must be chosen to be negative. For $\theta_L = -\frac{\pi}{2}$, the artificial line parameters were chosen: $C_{01} = 4.16$ pF and $L_{01} = 10.40$ nH. For the −90° phase-shifting line, a five-stage design was also chosen. For providing $\theta_R = +\frac{\pi}{2}$, the artificial line parameters $C_{02} = 10.83$ pF and $L_{02} = 27.07$ nH were chosen. The device was fabricated on microstrip TL sections and lumped element phase-shifting sections designed using the MuRata chip lumped element as surface-mount device (SMD) components (Figure 36b). The amplitude and phase characteristics are given in Figure 36c and d. The device is very broadband. Combined with its compact, planar design, and the fact that the two output ports can be spaced closely together, the suggested balun is well suited for feeding planar devices that require a broadband differential input signal.

From the point of view of practical realization, it seems suitable to eliminate the external phase-shifting TLs and to provide the 180° phase difference by means of TL sections forming the Wilkinson power divider. Let us consider the Wilkinson power divider with one of the TL sections replaced by an LH TL of the same characteristic impedance and of the electrical length −90°. The electromagnetic waves propagating from port 1 along the divider lines should be in-phase in ports 2 and 3 for a proper power division. At the same time, the waves propagating from port 2 should be of opposite phases in port 3 to isolate these ports from each other. Both conditions are satisfied by introducing an additional 180° TL section between ports 2 and 3 as shown in Figure 37a. The theoretical characteristics of this novel 180° power divider in the case of perfect RH and LH TLs with electrical lengths described by equations 19 and 20 are presented in Figure 37b. The operational bandwidth regarding the amplitude response is maximum when the normalized characteristic impedance of the 180° TL section is $\bar{Z}_0 = 1$. The fractional bandwidth is about 40% if determined at the 20-dB level of both the

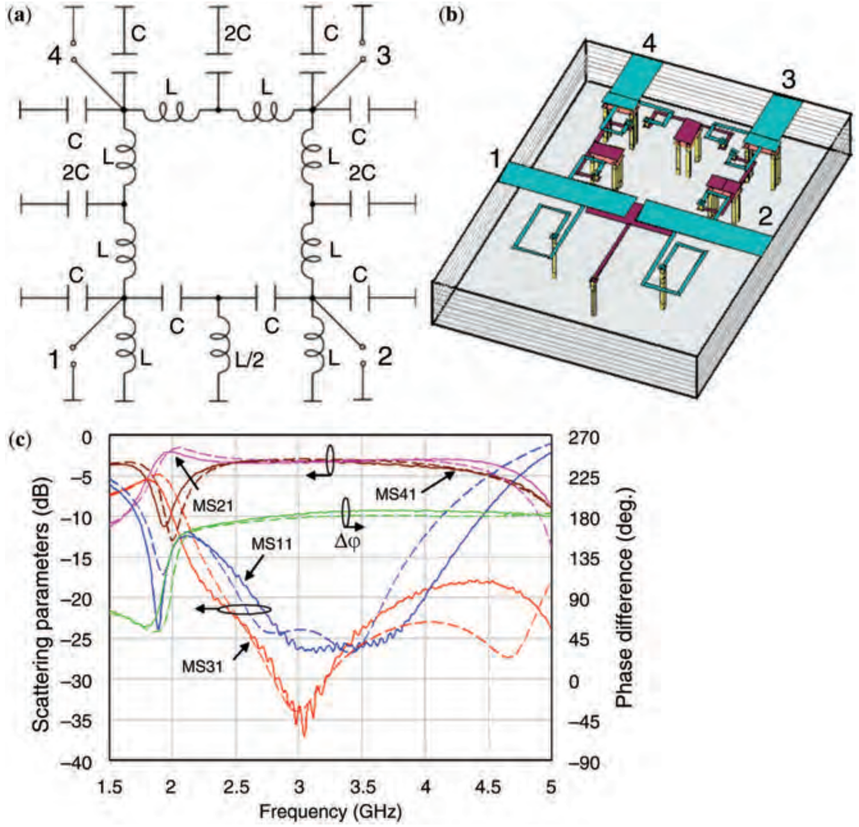

Figure 32. Broad-band rat-race ring directional coupler using two single cells of RH and LH TL sections in the ring: (a) equivalent diagram, (b) LTCC implementation of the rat-race ring, and (c) performance of the device: simulation (dashed lines) and measurements (solid lines).

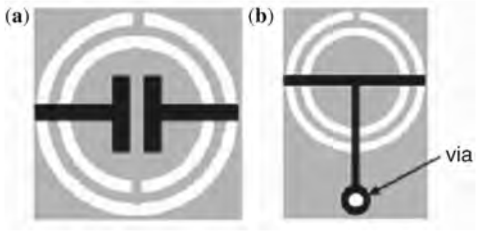

Figure 33. Topologies of the (a) LH and (b) RH unit cells implemented by means of CSRR. Bottom metal is depicted in gray. From Reference 50; copyright © 2007 IEEE, reprinted with permission conveyed through Copyright Clearance Center, Inc.

return loss and the isolation. The amplitude unbalance within this bandwidth is −0.5/+0.9 dB, and the phase shift is 180 ± 17°. The phase shift error can be decreased to ±10.5° by choosing $\bar{Z}_0 = \sqrt{2}$. It narrows the bandwidth to 34% with improvement of the amplitude unbalance up to −0.4/+0.5 dB.

The operational bandwidth of the 180° Wilkinson power divider can be enhanced by using a cascaded connection of the TL sections with electrical lengths $|\theta| < 90^\circ$ (55).

Dual-Band Directional Couplers and Power Divider-Combiners on RH/LH TL Sections and CRLH TL Sections

Different designs of dual-band directional couplers incorporating metamaterial LH TLs have been recently reported (11, 56–58). Most designs are based on a consideration of CRLH structures. Depending on the technology available, the LH TL section can be also realized using SMD inductors and capacitors. In some cases, the SMD realization is not advantageous due to standard-scale and tolerance of element values. Involving multilayer LTCC technology, we use another approach to design dual-band directional couplers with fully integrated implementation of LH TL sections on quasi-lumped elements, which does not require any SMD components.

A conventional branch-line directional coupler has spurious responses at the frequencies $f = (2n - 1)\cdot f_0$, where $n = 1,2,3\ \ldots$, due to resonant properties of λ/4 nondispersive RH TL sections. Using a combination of RH and LH TLs in the coupler branches allows changing the dispersion law and, therefore, shifting the first spurious response from $3f_0$ to an arbitrary frequency. For example it can be moved to the frequency $f_1 = 2f_0$ to design a dual-band directional coupler for applications in a GSM/DCS (900/1800 MHz) transceiver.

The overall phase incursion along cascaded LH and RH TL sections having the same characteristic impedance Z_0 is

$$\varphi_\Sigma(f) = \varphi_L(f) + \varphi_R(f) \tag{50}$$

For an RH TL, the propagation constant k is proportional to the frequency and the phase response is $\varphi_R(f) =$

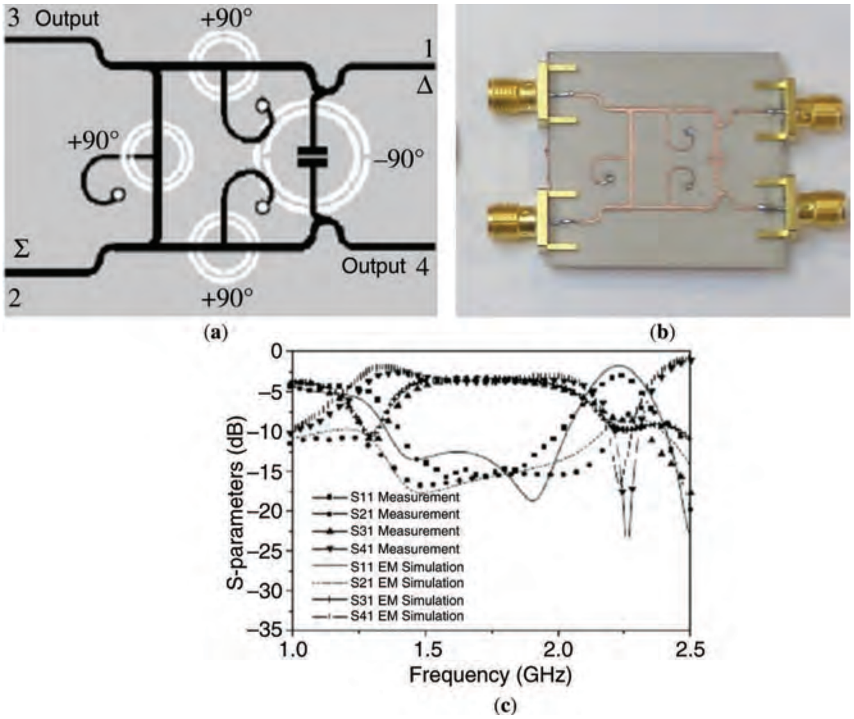

Figure 34. (a) Layout of the rat-race ring directional coupler on artificial LH and RH microstrip lines; upper metal level is depicted in black, whereas the bottom metallization is depicted in gray. (b) Photo of the device. (c) Impedance matching (S11), coupling (S31, S41), and isolation (S21) for the CSRR-based directional coupler. From Reference 50; copyright © 2007 IEEE, reprinted with permission conveyed through Copyright Clearance Center, Inc.

$\varphi_R(f_0)\cdot f/f_0$; in the case of an LH TL, k is inversely proportional to the frequency and $\varphi_L(f)=\varphi_L(f_0)\cdot f_0/f$. Taking into account these frequency dependencies, from equation 50, one can obtain the following equations for the frequencies of the fundamental mode f_0 and the first higher harmonic f_1:

$$\begin{cases}\varphi_L(f_0)+\varphi_R(f_0)=\varphi_{\sum}(f_0)\\ \varphi_L(f_0)/m+\varphi_R(f_0)\cdot m=\varphi_{\sum}(f_1)\end{cases} \tag{51}$$

where $m=f_1/f_0$.

The overall phase incursion $\varphi_{\sum}$ along each branch of the dual-band directional coupler with the operational frequencies f_0 and f_1 has to be equal ±90° or ±270° at the operational frequency. For $m=2$, the solutions to equation 51, which comply with physical realizability conditions, i.e., $\varphi_L>0$ and $\varphi_R<0$, are summarized in Table 1. To satisfy matching conditions, the characteristic impedance of each section in a branch is chosen in the same manner as for the corresponding branch of the conventional directional coupler with the desired coupling value. Solution #1 (Table 1) seems to be the most suitable one for practical realization. The operational principle of the dual-band DC is illustrated by Figure 38a using solution #1.

For the practical realization of the dual-band directional coupler, the branches have been represented as combinations of three lumped-element LH TL sections with the electrical length of −60° and three sections of RH TL sections with the electrical length of +30° (47). The TL sections have been designed as single T-cells (Figure 4c). The 3-dB dual-band directional coupler with the operational frequencies $f_0=$ 900 MHz and $f_1=1800$ MHz was implemented as a fully integrated multilayer structure in 11 layers of DuPont Green Tape$^{\text{TM}}$ 951 LTCC with a thickness of 92 μm (Figure 38b).

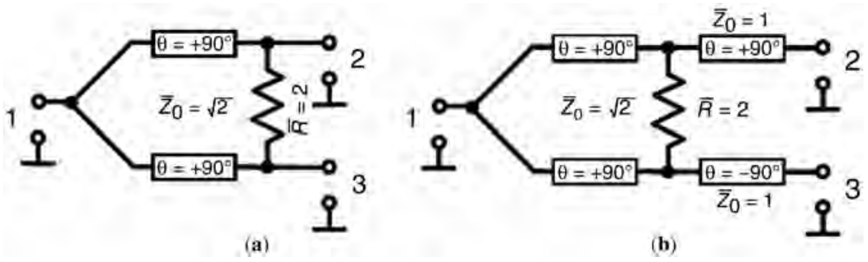

Figure 35. Schematic diagrams of the (a) classic Wilkinson power divider and the (b) 180° Wilkinson power divider employing external phase shifting RH and LH TL sections.

Table 1. Possible Combinations of the Phase Response Along the RH and LH Branches of the Dual-Band Directional Coupler

Solution	#1	#2	#3	#4	#5
$\varphi_L(f_0)$	+180°	+300°	+420°	+60°	+300°
$\varphi_R(f_0)$	−90°	−210°	−150°	−150°	−30°
$\varphi_{\sum}(f_0)$	+90°	+90°	+270°	−90°	+270°
$\varphi_{\sum}(f_1)$	−90°	−270°	−90°	−270°	+90

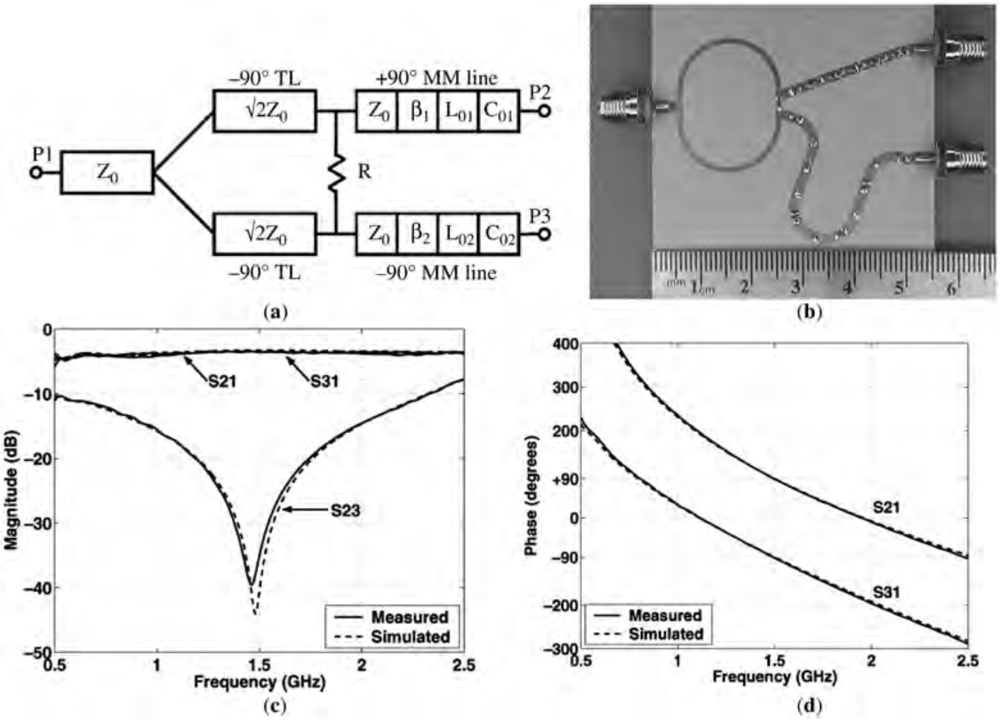

Figure 36. Architecture of the (a) metamaterial balun and (b) its photo. Performance of the 180° Wilkinson power divider: (c) amplitude response and (d) phase response. From Reference 54; copyright © 2005 IEEE, reprinted with permission conveyed through Copyright Clearance Center, Inc.

Characteristics of the 3-dB dual-band directional coupler obtained by electromagnetic simulation of the multilayer structure are presented in Figure 38c.

The conventional branch-line directional coupler can be modified by replacing its RH TL sections by CRLH TLs to yield a coupler with an arbitrary second operating frequency (59). The advantage of the CRLH TL over the RH TL for a dual-band branch-line directional coupler can be seen in the phase-response diagram of Figure 39a. Since the phase-response curve of the RH TL is a straight line

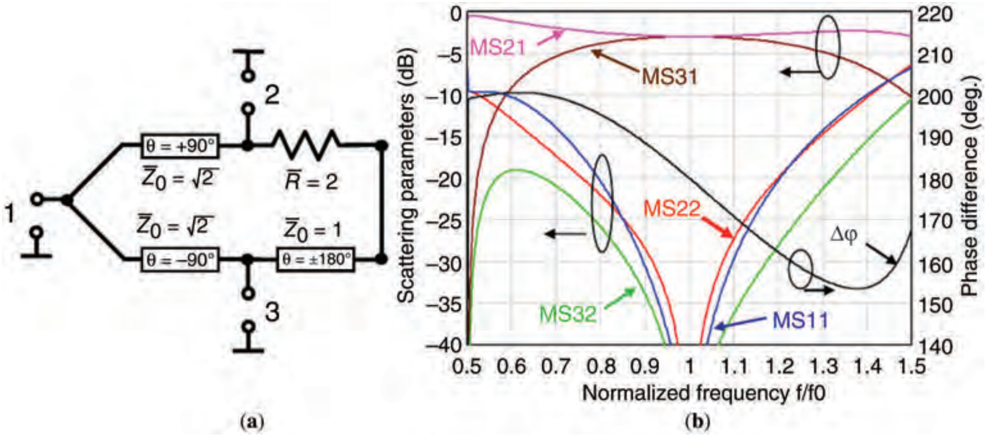

Figure 37. 180° Wilkinson power divider: (a) schematic diagram and (b) simulated characteristics of the divider.

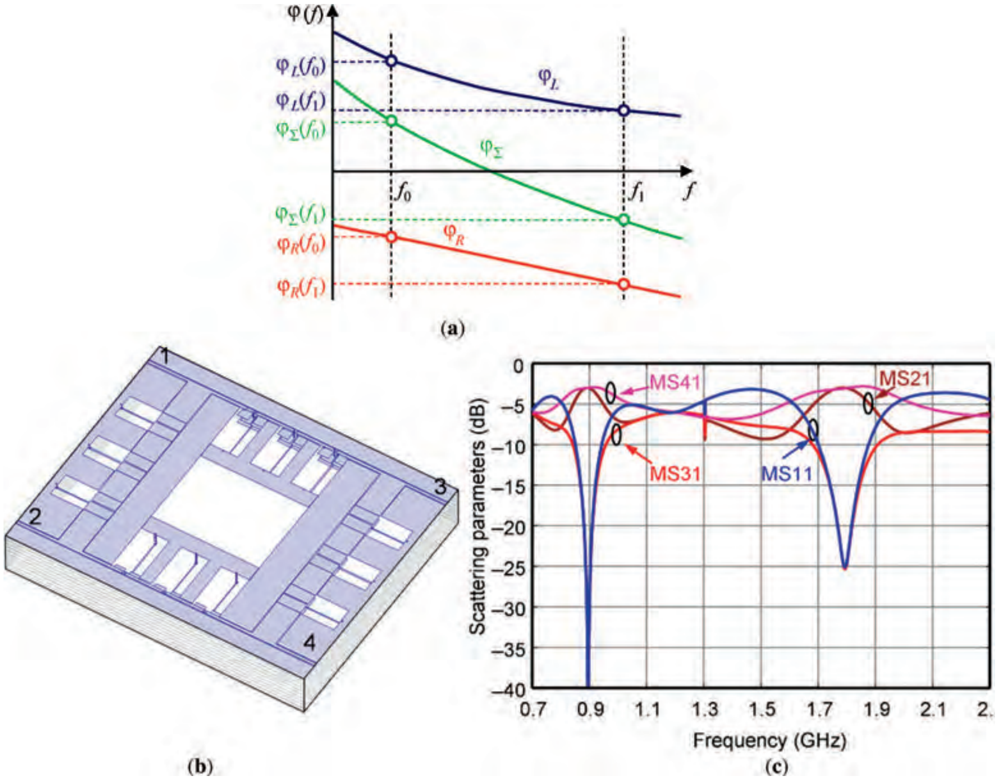

Figure 38. Phase diagram of (a) RH and LH TL sections, (b) LTCC implementation of the dual-band directional coupler, and (c) its S-parameters versus frequency.

from dc to f_1, the design frequency f_1 at -90° determines the next usable frequency $3\,f_1$ at -270°. By changing the phase slope of the RH TL, the frequency at -270° can be varied but -90° is no longer at the design frequency. Since the CRLH TL has a dc offset, it has an additional degree of freedom compared with the RH TL. By changing the dc offset and phase slope, the CRLH TL phase-response curve can intercept a desired pair of phases at any arbitrary pair of frequencies (f_1, f_2) for dual-band operation. Figure 39b shows a CRLH-based branch-line directional coupler with operational frequencies at $f_1 = 930$ MHz and $f_2 = 1780$ MHz and corresponding phase delays of 90° and 270°, respectively. The CRLH TLs were implemented with SMD chip components (11).

The generalized CRLH-line concept exhibiting four independent transmission bands (and hence described by eight independent elements) is useful for the synthesis of structures exhibiting quad-band functionality (34, 60). The layout of the branch-line quad-band power splitter is depicted in Figure 40a. The branch-line coupler is composed of a pair of 50- and 35.35-Ohm impedance inverters, the parallel resonator of the shunt branch is realized by means of an open complementary split ring resonator OCSRR, and the parallel resonator of the series branch was implemented by parallel connecting a capacitive patch and a meander inductor (12). The measured power splitting and matching (inferred from the *Agilent E8364B* vector network analyzer) are depicted in Figure 40b, where for comparison purposes the results obtained from electromagnetic simulation are also included. The measured matching is better than 10 dB for the four bands. The measured transmission losses are 4 dB, 5.9 dB, 6.3 dB, and 4.6 dB at the 1st, 2nd, 3rd, and 4th bands, respectively.

A Wilkinson power divider is an attractive device for power-splitting networks. A design of dual-band Wilkinson power divider with arbitrary frequency of the second pass band is possible by using a combination of RH and LH TL sections. As in the case of the conventional branch-line directional couplers, the classic Wilkinson power divider has spurious responses at the frequencies $f = (2n-1) \cdot f_0$, where $n = 1,2,3\ldots$. To shift the second operational frequency band of the Wilkinson power divider to a desired frequency f_1, it is necessary to use the TL sections with nonlinear dispersion characteristics. For this purpose, an LH TL section is incorporated into each branch of the power divider. At the frequencies f_0 and f_1, the overall phase incursion should be equal to ±90°.

Let us assume for example that $f_1 = 2f_0$. Then one can easily obtain that $\varphi_\Sigma(f_0) = \varphi_\Sigma(f_1) = \pm 90^\circ$ if the electrical length of the RH and LH TL section is $\theta_{\mathrm{RH}} = 90^\circ$ and $\theta_{\mathrm{LH}} = -180^\circ$, respectively. A schematic diagram of such a dual-band Wilkinson power divider is shown in Figure 41a (55). The multilayer LTCC structure and the characteristics of electromagnetic simulation are presented in Figure 41b and c, respectively. The device is manufactured in 11 layers of DuPont Green Tape$^{\mathrm{TM}}$ 951 LTCC with a thickness of 92 μm. The branches are

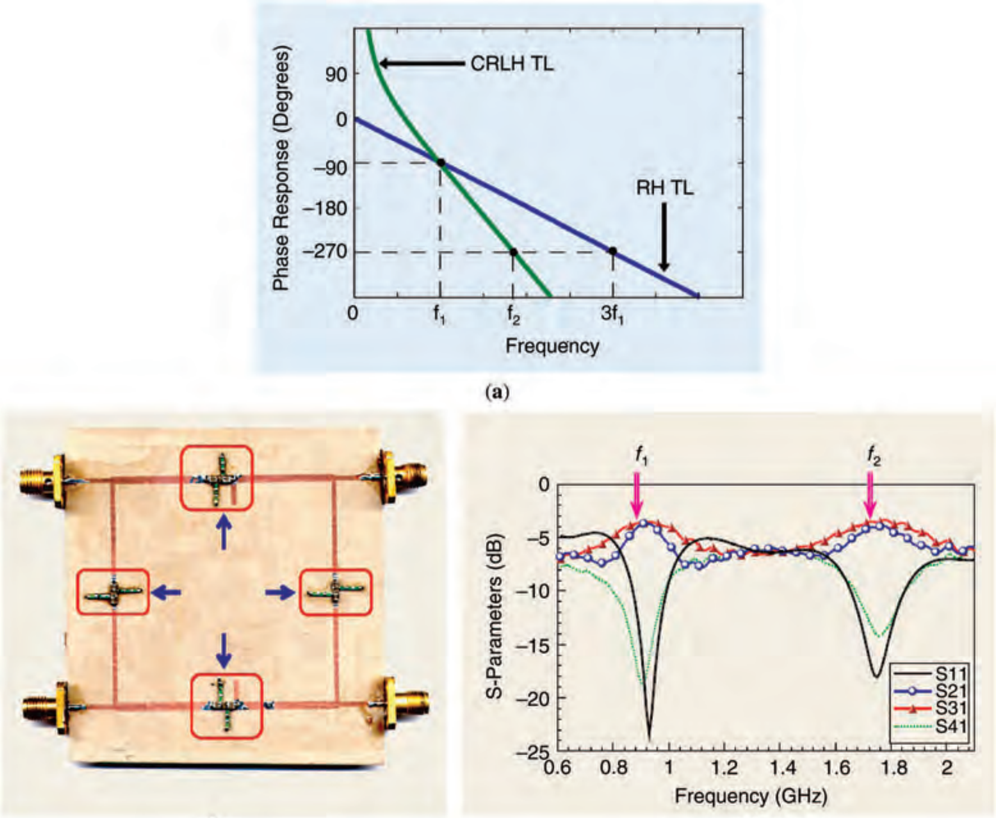

(a)

(b) (c)

Figure 39. (a) The general phase response of RH TL and CRLH TL. Photo of the (b) dual-band branch-line directional coupler on CRLH and (c) its S-parameters versus frequency. From Reference 11; copyright © 2004 IEEE, reprinted with permission conveyed through Copyright Clearance Center, Inc.

designed as a combination of three lumped-element T-cells of LH TL sections with the electrical length of -60° and four sections of natural coplanar RH TL with the electrical length of $+22.5^\circ$. The 100-Ohm resistor is used. The overall dimension of the LTCC structure is $30 \times 30\,\mathrm{mm}^2$ in plane.

It is worth mentioning that the ratio of the frequencies f_0 and f_1 can be chosen in an arbitrary way. In general, for arbitrary m, it is necessary to use equation 51 to find the necessary phase incursion along the chosen branch of the device.

Many different versions of microwave directional couplers used as power dividers/combiners demonstrate that using the metamaterial approach for a realization of these devices makes it possible to enlarge functionality of the directional couplers, extend the operational bandwidth, and provide a miniaturization of the directional couplers suitable for mass production.

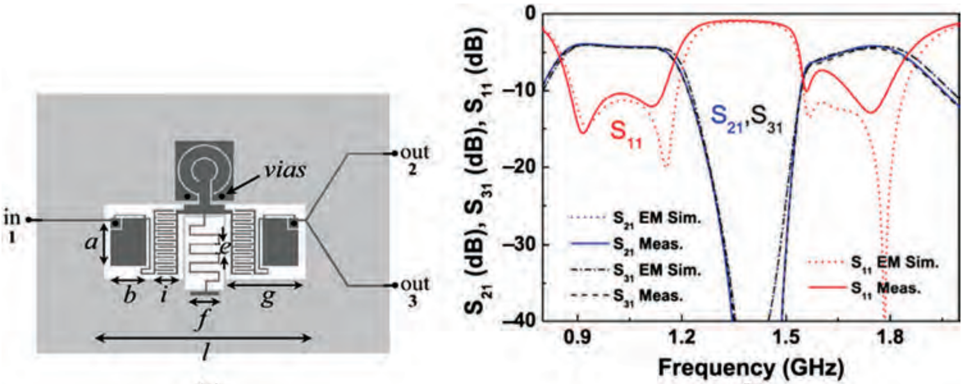

(a) (b)

Figure 40. Quad-band power splitter. The layout of the (a) power splitter and the (b) measured (solid lines) and simulated (dotted lines) S-parameters of the power splitter. From Reference 36; copyright © 2010 IEEE, reprinted with permission conveyed through Copyright Clearance Center, Inc.

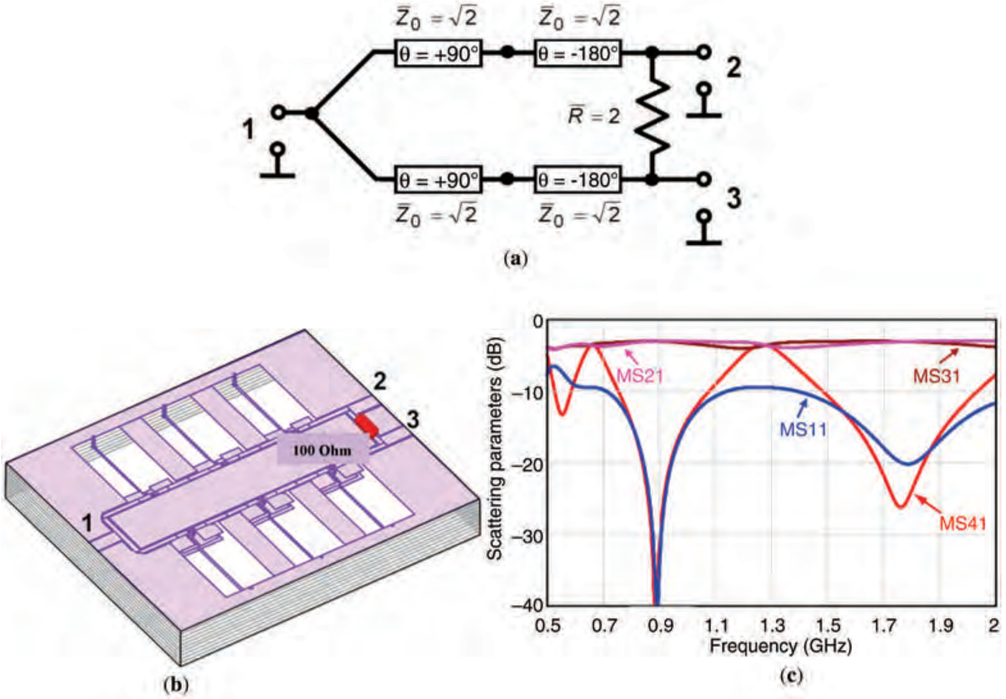

Figure 41. Schematic diagram of the (a) dual-band Wilkinson power divider, (b) multilayer LTCC structure, and (c) simulated performance of the dual-band Wilkinson power divider.

TUNABLE DEVICES BASED ON A COMBINATION OF LH/RH TL SECTIONS

Microwave devices based on metamaterial TLs demonstrate a specific feature useful for practical applications. For the design process, lumped-element T- or Π- single cells of the RH and LH transmission line sections are used. The CRLH unit cells also are widely used. The cells contain capacitive components. This provides the possibility of using tunable capacitors instead of fixed ones and provides tuning of the microwave devices in a wide frequency range. Most electronically tunable devices use varactor diodes as a tuning element. The benefit of varactors is fast tuning and low control voltage. Nevertheless, a low Q-factor of varactor diodes leads to increased insertion loss. Among many different devices based on a combination of RH and LH TL sections, CRLH unit cells with the most effective tunability exhibit resonators, filters, and directional couplers.

Tunability of Artificial TL Section Based on Lumped Components With Tunable Capacitances

A transmission-line section with the characteristic impedance Z_0 and the electrical length of θ can be presented at a central frequency ω_0 as an artificial T- or Π-network based on *LC*-elements (Figure 4). Let us consider the Π-network as an equivalent of the TL section (Figure 42). The ABCD matrices of the TL sections with characteristic impedance Z_0 and electrical lengths θ_{RH} and θ_{LH} and their artificial equivalents using *LC*-elements are written as (61, 62)

$$[A]_{RH\ TL} = \begin{bmatrix} \cos(\Theta_{RH}) & iZ_{0RH}\sin(\Theta_{RH}) \\ iZ_{0RH}^{-1}\sin(\Theta_{RH}) & \cos(\Theta_{RH}) \end{bmatrix} \tag{52}$$

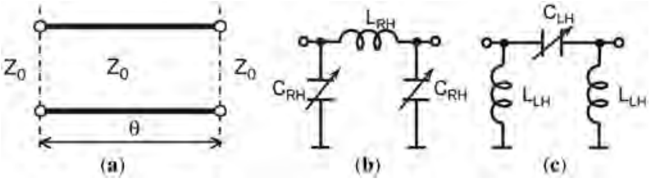

Figure 42. (a) A transmission line section and its equivalent representation as a Π-network of the (b) RH TL section and (c) LH TL section with variable capacitances.

$$[A]_{\Pi\ RH} = \begin{bmatrix} 1-\omega_0^2 L_{RH}C_{RH} & i\omega_0 L_{RH} \\ i\omega_0\left(2C_{RH}-\omega_0^2 L_{RH}C_{RH}^2\right) & 1-\omega_0^2 L_{RH}C_{RH} \end{bmatrix} \tag{53}$$

$$[A]_{LH\ TL} = \begin{bmatrix} \cos(\Theta_{LH}) & iZ_{0LH}\sin(-\Theta_{LH}) \\ iZ_{0LH}^{-1}\sin(-\Theta_{LH}) & \cos(\Theta_{LH}) \end{bmatrix} \tag{54}$$

$$[A]_{\Pi\ LH} = \begin{bmatrix} 1-\dfrac{1}{\omega_0^2 L_{LH}C_{LH}} & (i\omega_0 C_{LH})^{-1} \\ i\omega_0\left(-\dfrac{2}{\omega_0^2 L_{LH}}+1/\omega_0^2 C_{LH}L_{LH}\cdot\omega_0^2 L_{LH}\right) & 1-\dfrac{1}{\omega_0^2 L_{LH}C_{LH}} \end{bmatrix} \tag{55}$$

Comparing equations 52–55, one obtains:

$$\theta_{RH} = \cos^{-1}\left(1-\omega_0^2 L_{RH}C_{RH}\right) \tag{56}$$

$$Z_{0RH} = \frac{\omega_0 \cdot L_{RH}}{\sin(\theta_{RH})} \tag{57}$$

$$\theta_{LH} = \cos^{-1}\left(1 - \frac{1}{\omega_0^2 L_{LH} C_{LH}}\right) \tag{58}$$

$$Z_{0LH} = \frac{(\omega_0 C_{LH})^{-1}}{\sin(-\theta_{LH})} \tag{59}$$

The electrical length of the quarter-wavelength TL section at the frequency ω_0 is equal to $|\theta| = \pi/2$. If the capacitance is changed while tuning, the electrical length of the TL section at the frequency ω_0 is also changed and $|\theta| \neq \pi/2$, although at some other frequency the electrical length is $|\theta| = \pi/2$. Figure 43 illustrates this possibility for different values of capacitances in the Π-cells of RH TL and LH TL. The phase response $\varphi = -\theta = \pm 90^\circ$ is observed at different frequencies. From equations 56 and 58, the frequency ω_0 for the quarter-wavelength TL section is defined as

$$\omega_0 = \frac{1}{\sqrt{LC}} \tag{60}$$

where L and C are L_{RH} and C_{RH} for the RH TL section and L_{LH} and C_{LH} for the LH TL section. In line with equation 60, the central frequency ω_0 can be tuned by a variation of the capacitance value while the inductance value is kept constant. At the same time from equations 57 and 58, one can obtain:

$$Z_0 = \sqrt{\frac{L}{C}} \tag{61}$$

Thus, the value of the characteristic impedance Z_0 will be also changed by the capacitance variation, which leads to mismatching of the device in the frequency range of tunability.

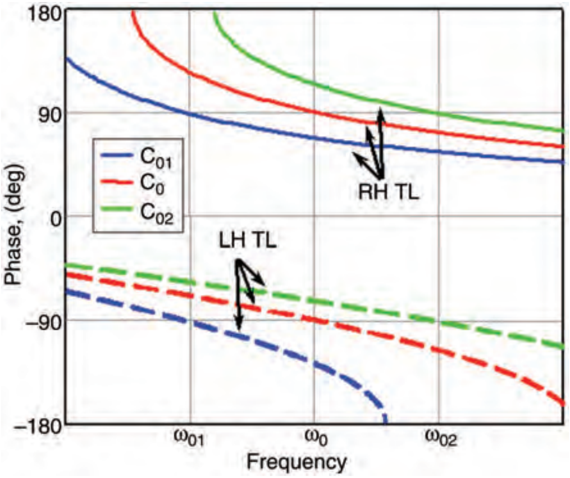

Figure 43. Phase response of the Π-cell of (a) RH TL and (b) LH TL sections versus frequency for different values of tunable capacitance.

Let us say that we would like to tune the TL section in frequency range from $\omega_1 < \omega_0$ to $\omega_2 > \omega_0$. In this case, the corresponding capacitances and characteristic impedances are C_1, Z_{01} and C_2, Z_{02}. At both frequencies ω_1 and ω_2, the electrical lengths of the TL section have to be equal $\theta_{01} = \theta_{02} = \pi/2$. From equations 56–59, the following is obtained:

$$\frac{\omega_{02}}{\omega_{01}} = \sqrt{\frac{C_1}{C_2}} \tag{62}$$

$$\frac{Z_{02}}{Z_{01}} = \sqrt{\frac{C_1}{C_2}} \tag{63}$$

By comparing equations 62 and 63, one can find:

$$\frac{\omega_{02}}{\omega_{01}} = \frac{Z_{02}}{Z_{01}} \tag{64}$$

To determine the tunability range formed by a set of variable central frequencies calculated from equation 60, it is necessary to determine an admissible level of reflection coefficient Γ:

$$\Gamma = \frac{\overline{Z}_{in} - 1}{\overline{Z}_{in} + 1} \tag{65}$$

Here $\bar{Z}_{in} = Z_{in}/Z_0$ is the normalized input impedance of the Π-equivalent of the TL section. In the case of a quarter-wavelength TL section ($\theta = \pi/2$), the normalized input impedance is:

$$\overline{Z}_{in} = \overline{Z}_0^2 \tag{66}$$

From equations 65 and 66, one obtains:

$$\overline{Z}_0 = \sqrt{\frac{1+\Gamma}{1-\Gamma}} \tag{67}$$

Using equations 64 and 67, the following useful formula was obtained:

$$\frac{\omega_{02}}{\omega_{01}} = \frac{1+|\Gamma|}{1-|\Gamma|} = \mathrm{VSWR} \tag{68}$$

where VSWR is the voltage standing wave ratio, which is used for mismatching estimation. In Table 2, the operational frequency range determined by a permissible level of mismatching is presented. There is a trade-off between the width of the frequency band of tunable devices and the mismatching level.

Table 2. Parameters of the Tunable TL Section ($\theta = \pi/2$)

Return loss $\lvert S_{11}\rvert^2$, dB	VSWR	ω_{02}/ω_{01}
20	1.2	1.2
15	1.5	1.5
10	2.0	2.0

Tunable Rat-Race Ring Power Divider-Combiner

Let us consider a tunable rat-race ring based on the equivalent diagram in Figure 44a. Variable capacitances are used instead of fixed ones in the artificial RH and LH TL sections. The equivalent circuit has been optimized to operate at frequency f_0.

Using the procedure described earlier, the range of tunability of the central frequency $f_0 = 1.8\,\text{GHz}$ can be estimated by a specification of the permissible level of mismatching at the edges of the tuning range. In many practical applications, the reflection coefficient should be better than 15 dB that corresponds to $\Gamma_{\text{adm}} = \pm 0.18$. Using equations 64 and 68, one can calculate the tunability of the central frequency as $f_{02} = 1.43 \cdot \omega_{01}$. The predicted range of tunability is defined by $f_{01} = 1.4\,\text{GHz}$ and $f_{02} = 2.2\,\text{GHz}$.

As tuning elements, varactor diodes are used in the tunable rat-race ring directional coupler. Figure 44b shows the equivalent circuit of a tunable rat-race ring with varactor diodes used as variable capacitances. The shunt capacitances $2C$ and serial capacitance C are replaced by the varactor diodes VD1 and VD2, respectively. Hyperabrupt silicon varactors from Skyworks Inc. (63) have been used. To exploit the potential tuning range optimally, the varactor diodes SMV1231 (VD1) and SMW1233 (VD2) have been chosen. The resistors R and blocking capacitors $C1$ and Cb are used for the biasing network.

Multilayer LTCC technology has been used for practical realization of a tunable rat-race ring. Figure 45a shows the LTCC module design. The inductors L were embedded into eight LTCC layers of the 95-μm-thick DuPont Green Tape$^{\text{TM}}$ 951. The other components are designed as SMD and placed on the top of the LTCC module. The multilayer module of the tunable rat-race ring has been simulated using Sonnet software. The SPICE models of varactor diodes including losses and parasitic effects like package inductance and capacitance have been used. The module has been manufactured. The photograph of the demonstrator is shown in Figure 45b. The SMD components were mounted on the top of the ceramic module. The device size is 16 mm × 16 mm × 0.76 mm.

The results of simulation and measurements of the tunable rat-race ring for different biasing voltages applied are presented in Figure 46. According to the measured data, the device provides equal power division between outputs with unbalance across the 200-MHz band less than ±1 dB. The high level of the insertion loss level (1.3 dB) can be explained by the additional insertion loss caused by SMD components. The measured reflection coefficient is 15 dB at frequencies $f_{01} = 1.4\,\text{GHz}$ and $f_{02} = 2.4\,\text{GHz}$. The range of tunability is 1.4–2.4 GHz, which corresponds to the estimated tunability of 70%.

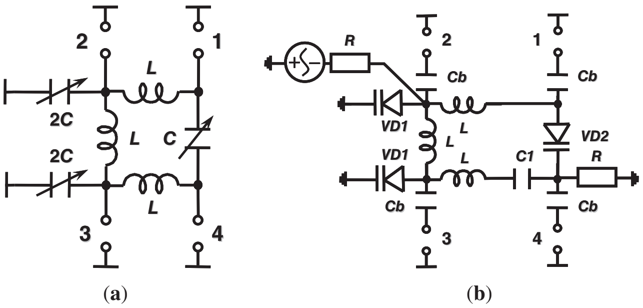

(a) (b)

Figure 44. Equivalent circuits of the (a) tunable rat-race ring and (b) the tunable rat-race ring with varactor diodes and biasing components.

Tunable Resonators and Filters on a Combination of LH and RH TL Sections

To design a filter with a highly flexible frequency response, the possibility exists of controlling the frequency location of the pass-bands by considering variable capacitances in the RH and LH TL sections of the dual-mode SIR (Figure 15). The voltage-dependent capacitance $C(V)$-values have been taken as specified in the data sheet for hyperabrupt silicon varactors [Skyworks, Inc., (63)]. The simulation revealed distinct differences between controlling the capacitances of the LH and the RH TL section (62). By replacing the series capacitances of the LH TL section by SMV1232 varactors, only the position of the lower pass-band was tuned. The equivalent diagram of the two-pole dual-band tunable filter is depicted in Figure 47a. The multilayer LTCC structure of the tunable dual-band filter with variable capacitors and bias resistors is shown in Figure 47b. The tunable dual-band filter was manufactured and experimentally investigated. The SMV1232 varactors and 1-MOhm resistors have been mounted on the top of the multilayer substrate, while the other components were embedded in the LTCC multilayer structure. The photograph of the device under test is presented in Figure 47c. The experimental results are shown in Figure 47d. The reflection coefficient was better than 16 dB for all values of the control voltage. The insertion loss remained below 3.2 dB and 4 dB at the frequencies f_0 and f_1, respectively. As expected, the lower pass-band could be tuned while the upper pass-band remained fixed. The measured tunability of the lower pass-band is 28%. Based on this promising result, further improvements are expected for a selection of varactors with lower dissipation losses.

Controlling the shunt capacitances of both RH TL sections by SMV1231 varactors (Figure 48a) resulted in a shift of both pass-bands to higher frequencies. The widths of the pass-bands were changed slightly upon tuning. The tunability of the first pass-band amounted to 20%, while that of the second pass-band reached 42%. Both values are higher than would be required to compensate for the deviation of the frequencies f_1 and f_2 caused by the fabrication tolerances of the LTCC process.

The simultaneous tuning of the RH and LH TL sections by varactor diodes opens the possibility of tuning both pass-bands. In this case, either the ratio of the two center frequencies or their difference could be kept constant, as illustrated by Figure 48b and 48c, respectively.

Reconfigurable 0-dB Directional Coupler Using Metamaterial Structures

Coupled-line directional couplers are widely used for microwave applications. It is challenging task to design a traditional coupled-line 0-dB directional coupler with a

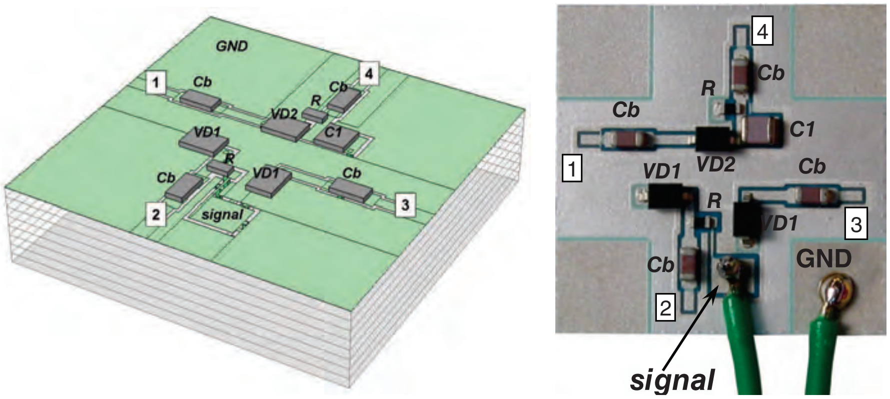

(**a**) (**b**)

Figure 45. Multilayer LTCC structure of the (a) tunable rat-race ring and (b) the top view of the demonstrator with mounted SMD components.

high directivity because it either requires a combination of even- and odd-mode impedances that are nonrealizable in practice or needs a very long coupling length. In Ref. 64, a novel forward-wave directional coupler with a strong coupling level was presented. The coupler was designed with the same characteristic impedances for even and odd modes (50 Ohm) and enhanced difference of propagation constants for the even and odd modes. It was achieved by adding a mushroom-shaped ground plane to coupled lines. The other approach of design of a 0-dB forward wave directional coupler was discussed in Ref. 65. It consists of a pair of microstrip coupled lines and an etched periodical structure on the ground plane.

Let us consider a possibility of using a combination of two types of metamaterial structures: SRR and mushroom-shaped resonators as constituents of the coupled-line directional coupler. The structure of a 0-dB directional coupler with forward and backward power coupling is presented in Figure 49a. It is realized as two coupled microstrip lines loaded with SRRs and mushroom-shaped resonators. The width of the lines is 200 μm, and the coupling gap is 100 μm. The structure consists of two dielectric layers of Rogers RO3010 (dielectric characteristics: $\varepsilon_r = 11.2$, $\tan\delta = 0.0022$) with thicknesses $h = 130\,\mu$m and $h = 1280\,\mu$m. On the first thin layer, the coupled lines with a pair of SRRs are printed. The second layer is used for implementation of mushroom-shaped resonators.

The SRR coupled with the microstrip line forms a stop band structure at its resonance frequency and prevents microwave power from going through the coupled lines, which helps to obtain backward coupling characteristics. The mushroom-shaped resonators work as a matching network and allow achieving forward wave characteristics at other frequencies. The results of full-wave simulation are shown in Figure 49b. If port 1 is assigned as an input one, the power goes to port 4 at 5.9 GHz and to port 3 at 6.9 GHz. In this way, two types of 0-dB coupling are observed at two different frequencies. The insertion loss level is 2 dB and 2.5 dB, respectively.

The 0-dB directional coupler with forward and backward power coupling can be used as a core for designing a reconfigurable 0-dB directional coupler (66). The tunable varactor diodes are inserted in the gap of the SRR. Changing the capacitance of varactors by applying biasing voltage leads to a variation of the resonance frequency of the SRR. In turn it results in achieving two types of coupling at the same frequency.

The structure of the reconfigurable 0-dB directional coupler is presented in Figure 49c. The capacitance of the varactor diode (KV1993A by Microsemi) varies from 0.6 pF to 0.35 pF by applying voltage from 1 V to 8 V. When the capacitance of varactor diode C_v is equal to 0.35 pF, the input power goes to port 4 and one obtains backward coupling characteristics. In the case of $C_v = 0.4$ pF, port 3 works as an output corresponding to forward coupling. Figure 49 shows the results of full-wave simulations of the structure scattering parameters. The central frequency is 7.5 GHz.

The considered examples of tunable and reconfigurable microwave circuits using metamaterial TL sections or metamaterial resonant components demonstrate a variety of microwave devices with enlarged functionality.

MICROWAVE PHASE SHIFTERS BASED ON SWITCHABLE LH AND RH TRANSMISSION LINE SECTIONS

The device providing a desired phase change of the electromagnetic wave is known as a phase shifter. The development of a compact one-dimensional phase shifter comprising sections of LH TL cascaded with sections of conventional RH TL sections can be used to synthesize an arbitrary transmission phase. This phase shifter offers some significant advantages when compared with standard delay TLs: It is more compact in size, it can achieve a positive or a negative phase shift including 0° phase shift while occupying the same short physical length, and it exhibits a linear, flatter phase response with frequency, leading to shorter group delays (11, 16, 67).

The much more interesting applications are related to the controllable phase shifters widely used in phased antenna arrays. The phase shifter is a loss-less two-port providing a change in a phase response of the electromagnetic wave under the control signal (current or voltage). There are two types of devices: digital and analog

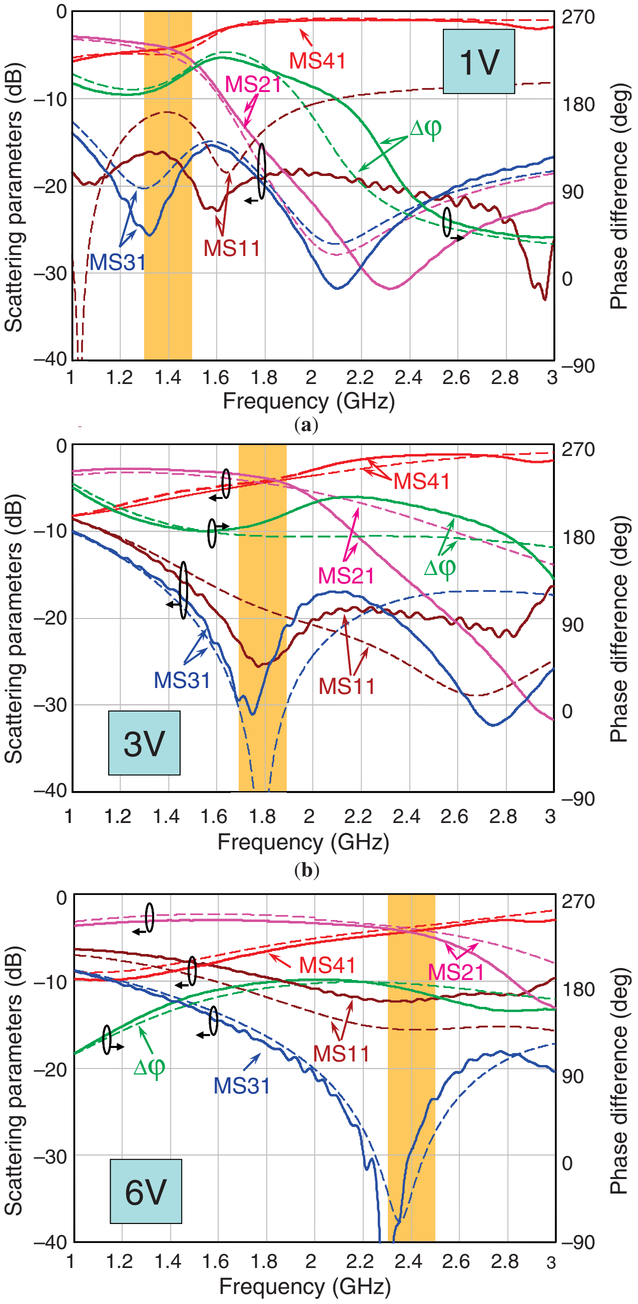

(a)

(b)

(c)

Figure 46. Results of experimental investigation (solid lines) of tunable rat-race ring for applied voltage 1–6 V in comparison with simulated results (dashed lines).

phase shifters. The unit cell of a digital phase shifter is characterized by two values of the phase of transmitted or reflected electromagnetic wave in two different states of the phase shifter. The analog phase shifter demonstrates a continuous change of the phase of transmitted or reflected electromagnetic wave under a control signal.

Well known are the digital phase shifters using switchable channels (68). In the device, electromagnetic waves propagate in turn along two channels formed by transmission-line sections of different electrical lengths. These lines are characterized by a different phase response, which is used for obtaining the differential phase shift. The channels are switched by two single-pole-double-throw (SPDT) switches. As the switches *p-i-n* diodes, microelectromechanical systems (MEMS)-capacitors or field-effect transistors (FET) are used. The devices are controlled by current or voltage, and the optical control also can be used.

Switching between a low-pass network and a high-pass network is commonly used to design broad-band phase shifters (68). The phase shift is flat over a wide frequency range due to the equal slope of the phase characteristics of two channels. However, a simultaneous control of the required phase shift and a suitable input matching within the same bandwidth is complicated. Inappropriate

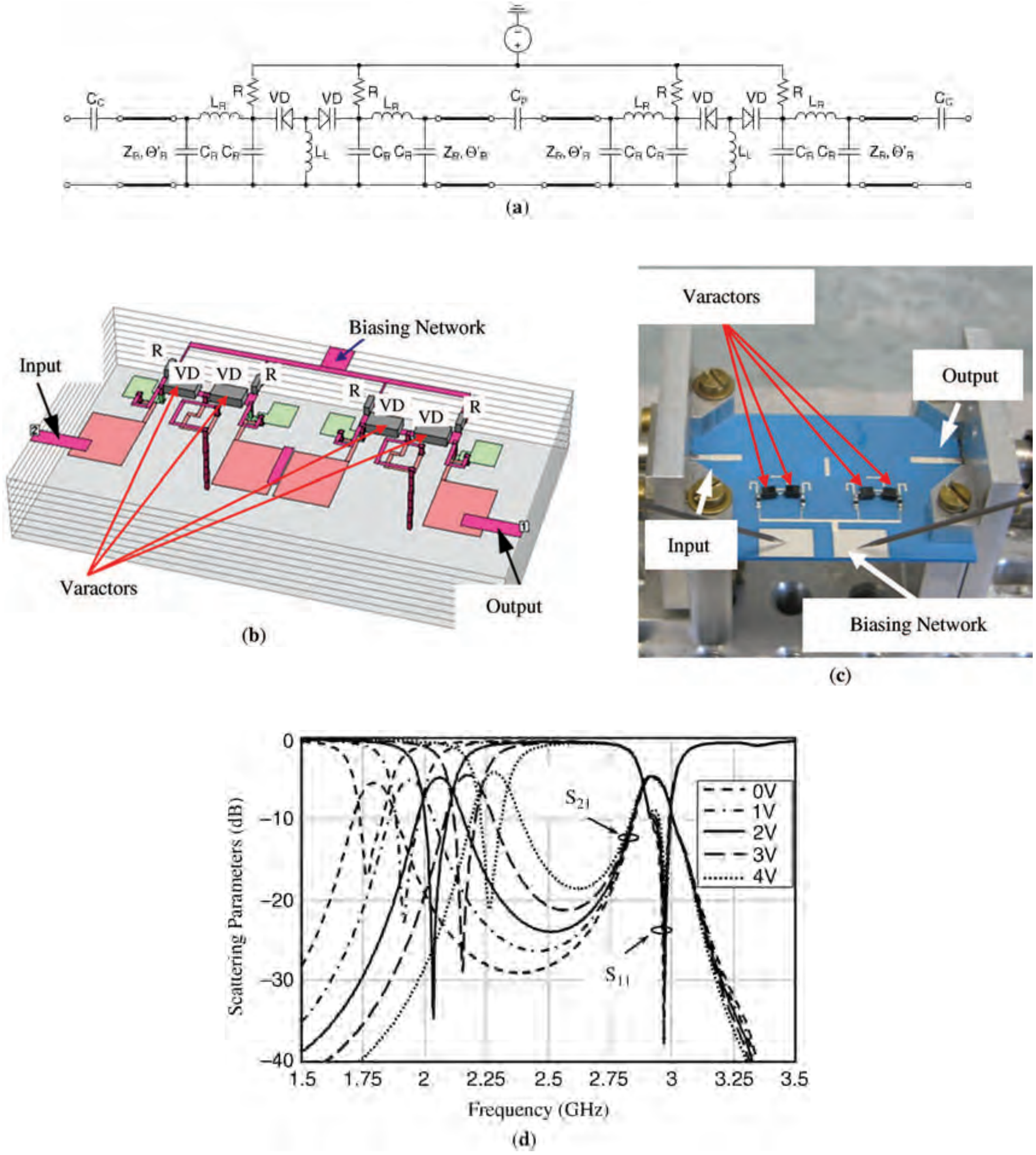

Figure 47. Equivalent diagram of the tunable version of the (a) dual-band filter, (b) layout of the dual-band filter by employing varactor diodes and bias resistors, instead of series capacitances of LH TL, (c) photograph of the device under test, and (d) experimental performance of the filter tuned by the series capacitances of the LH TL section.

mismatch causes a significant loss level of the device. On the other hand, the phase shifters based on two switchable transmission-line sections of different electrical lengths exhibit a broadband matching while the operational bandwidth is limited by a significant variation of the phase shift because of nonparallel phase responses in two states.

Using specific dispersion characteristics of RH and LH TLs makes it possible to combine the benefits of switchable channel phase shifters of both kinds. It was shown (69–72) that using a cascaded connection of RH and LH TL sections provides a similar slope of the phase response of two TLs of different electrical lengths. That means that in principle it is possible to design a controllable phase shifter based on switchable metamaterial TL sections providing a flat differential phase response.

General Properties of Microwave Digital Phase Shifters Based on RH and LH Transmission Line Sections

Let us consider a digital phase shifter based on switching between RH TL and LH TL sections. The operational principle of a digital phase shifter using switchable RH and LH TL sections is illustrated by Figure 50. In one state, the signal goes along the RH TL section with a negative phase response φ_1, whereas in another state, it propagates along the LH TL section with a positive phase response φ_2. The differential phase response (phase shift) $\Delta\varphi = \varphi_1 - \varphi_2$

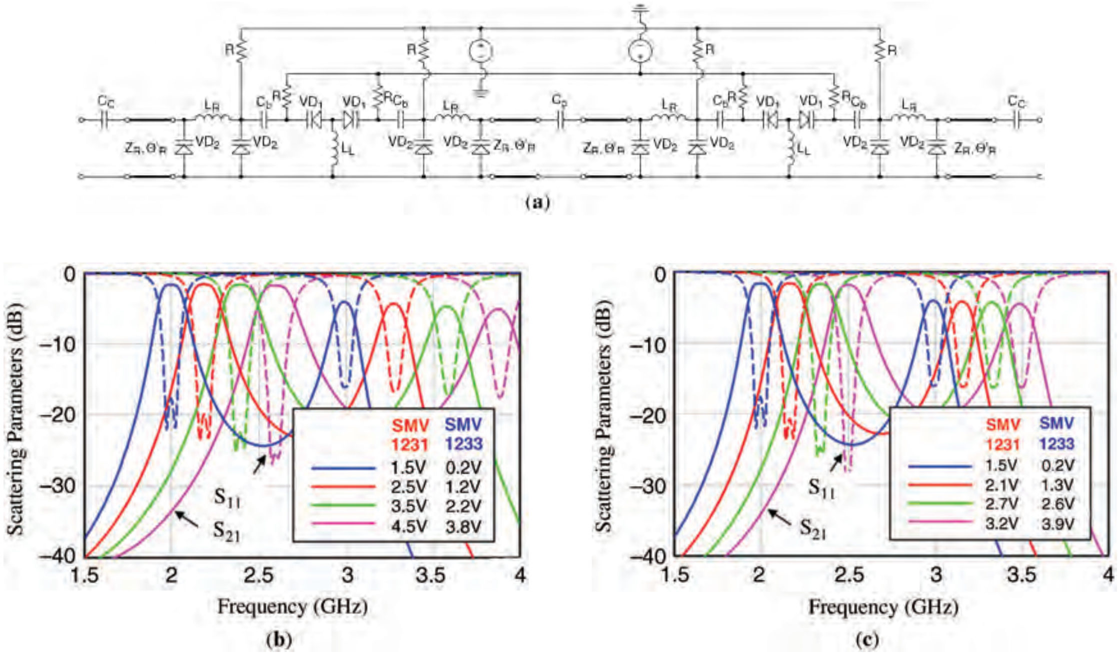

(a)

(b)

(c)

Figure 48. Equivalent diagram of the (a) tunable dual-band filter and results of circuit simulation of the dual-band filter with tunable (b) RH TL and (c) LH TL sections by varactor diodes.

is obtained by switching the signal path using two SPDT switches. Switching between the RH and LH TL sections with the electrical lengths, which are the same by absolute value at the central frequency and differ in sign, results in providing an almost constant phase shift over a fairly large bandwidth. It was theoretically estimated that in the case of ideal RH TL and LH TL sections switched by perfect SPDT-switches, the phase shift error is ±3% in one octave bandwidth and about ±12.5% over two octaves for any value of the phase shift within variation up to 180° (70, 10). Moreover, if the characteristic impedance of both transmission lines is equal to the port impedance, the perfect matching is provided in any frequency range for both states.

It is reasonable to create the phase shifter containing switchable RH and LH TL unit cells as T- or Π-networks (Figure 4). For different bits of a digital N-bit phase shifter giving the phase shift $\Delta\Phi_m$, the equivalent electrical length θ of both RH TL and LH TL should be chosen as follows:

$$|\theta|_m = \Delta\Phi_m/2 \tag{69}$$

where

$$\Delta\Phi_m = \Delta\varphi_{LH} - \Delta\varphi_{RH} \tag{70}$$

and $m = 1, 2, \ldots, N$ is the order number of the bit.

The number of different states of the digital phase shifter is defined as

$$p = 2^N \tag{71}$$

and the phase shift provided by the mth bit is

$$\Delta\Phi_m = \varphi_\Sigma/2^m \tag{72}$$

The unit cells presented in Figure 4 can be used as equivalent circuits of the sections of RH and LH transmission lines. In the frequency range close to the chosen frequency ω_0, the characteristics of the T- or Π-circuits with LC-parameters defined by equations 33–36 will be the same as for the corresponding RH/LH TL sections with known Z_0 and θ. This equivalent presentation of the RH/LH TL sections is used in a design of microwave devices.

The phase shift is determined by the LC-parameters of T- or Π-circuits used in the channels of the phase shifter. Using equivalence of the $ABCD$ matrix of a TL section with the $ABCD$ matrices of T- and Π-circuits, the phase characteristics of the RH and LH TL can be found as

$$\varphi_{RH}(\omega) = -\cos^{-1}\left(1 - \omega^2 L_R C_R\right) \tag{73}$$

$$\varphi_{LH}(\omega) = \cos^{-1}\left[1 - 1/\left(\omega^2 L_L C_L\right)\right] \tag{74}$$

The products $L_R C_R$ and $L_L C_L$ are the same for the T- and Π-sections for both RH and LH TL and are calculated using equations 33–36.

Equations 73 and 74 can be considered as dispersion equations. The main characteristic of interest is the slope parameter of the phase characteristics, which can be determined by the differentiation of equations 73 and 74 with respect to ω:

$$\frac{d\varphi_{RH}}{d\omega} = -\frac{\sqrt{2L_R C_R}}{\sqrt{1 - \omega^2 L_R C_R/2}} \tag{75}$$

$$\frac{d\varphi_{LH}}{d\omega} = -\frac{\sqrt{2/L_L C_L}}{\omega^2} \cdot \frac{1}{\sqrt{1 - 1/2\omega^2 L_L C_L}} \tag{76}$$

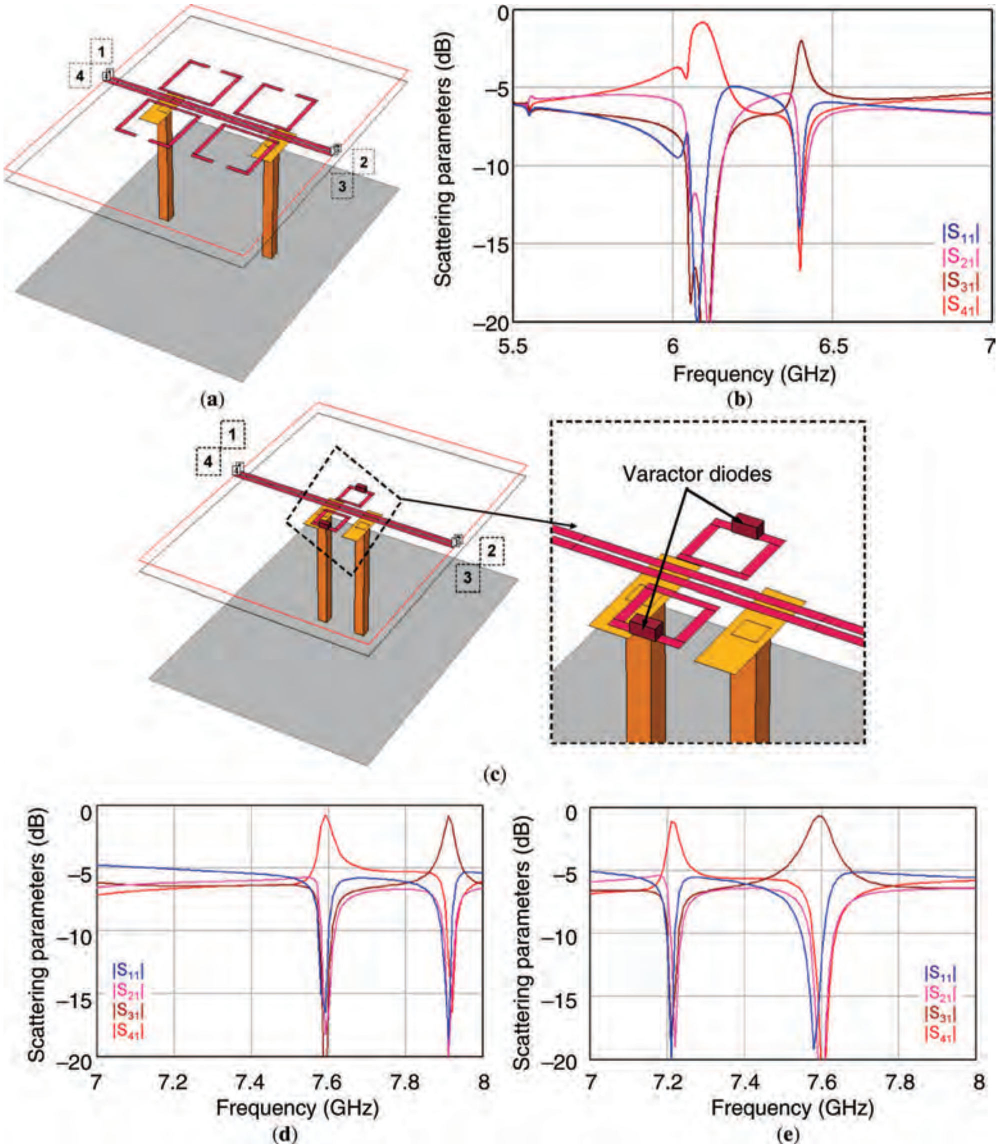

Figure 49. A 0-dB directional coupler based on a combination of SRRs and mushroom-shaped resonators embedded in the (a) coupled-line structure and (b) its performance; 0-dB reconfigurable directional coupler: (c) multilayer structure and characteristics of (d) backward and (e) forward types of coupling.

The phase response of a transmission-line section relates to the electrical length as $\varphi(\omega) = -\Theta(\omega)$. For the maximum available digital phase shift $\Delta\Phi = \varphi_{LH} - \varphi_{RH} = 180^\circ$ ($m = 1$), the electrical lengths of the both RH and LH channels $|\theta|_0 = 90^\circ$ and consequently $\omega_0^2 L_R C_R = \omega_0^2 L_L C_L = 1$. At the central frequency of the operational bandwidth ω_0:

$$\left.\frac{d\varphi_{RH}}{d\omega}\right|_{\omega=\omega_0} = \left.\frac{d\varphi_{LH}}{d\omega}\right|_{\omega=\omega_0} = -2\sqrt{L_{R,L}C_{R,L}} \qquad (77)$$

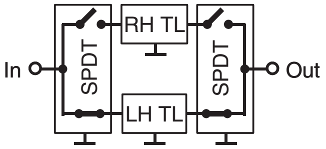

Figure 50. Equivalent diagram of a digital phase shifter based on switchable RH/LH TL sections of different electrical lengths.

This equality is valid at the central frequency only. The frequency dependence of the slope is different for LH and RH TL.

For $m > 1$, the terms in equations 75 and 76 $\omega_0^2 L_R C_R/2 \ll 1$, $1/2\omega_0^2 L_L C_L \ll 1$ and they both rapidly decrease when m arises. Thus, one can simplify equations 75 and 76 for $m > 1$:

$$\frac{d\varphi_{RH}}{d\omega} = -\sqrt{2L_R C_R} \qquad (78)$$

$$\frac{d\varphi_{LH}}{d\omega} = -\frac{\sqrt{2/L_L C_L}}{\omega^2} \qquad (79)$$

At the central frequency ω_0, the slope parameter of the phase characteristic is the same for RH and LH TL sections. The frequency-dependent slope of the RH TL

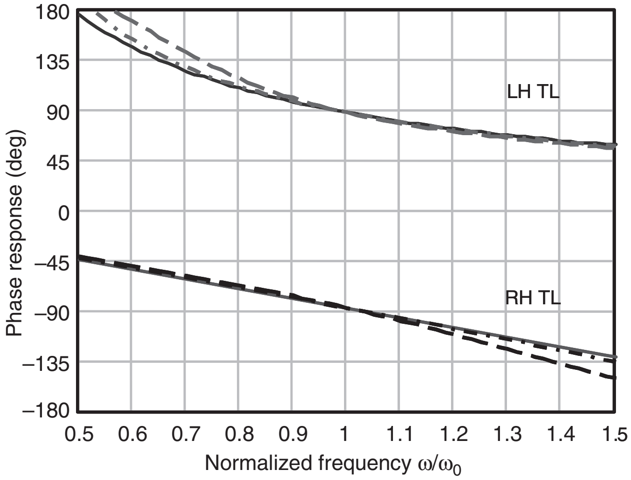

Figure 51. Phase characteristics versus normalized frequency for different numbers of *LC*-sections (single *LC*-section—dashed lines, two *LC*-sections—dash-dot lines, and ideal transmission line section—solid lines).

section made as the T- or Π-single cell is very close to the frequency-independent slope of the natural RH TL section of the same electrical length θ_0. The difference in the slope parameters of the LH and RH TL sections is remarkably pronounced at a lower frequency range ($\omega \ll \omega_0$) and is less at higher frequencies, although it arises at $\omega \gg \omega_0$. The simulations revealed that the smaller θ_0, the smaller the difference between the slope parameters of lumped-element LH and RH TL sections. Thus, one can conclude that for a design of the broad-band phase shifter on switchable RH and LH TL sections, it is reasonable to use the cascaded single cells with a small value of the equivalent electrical length. That is followed by the conclusion that for lower *m* the RH and LH branches should be designed as a cascaded connection of RH and LH TL single cells (T or Π) having a small electrical length.

As an example, Figure 51 presents the theoretical phase responses of the RH TL and LH TL sections for a different number of *LC*-sections providing the phase shift of 180° while switching the RH and LH channels. In the normalized bandwidth of one octave (0.707–1.414), the deviation of the phase shift for RH and TL sections is ±5.5°. The higher number of single cells used for a design of the phase shifter on switchable RH/LH TL channels, the closer the characteristic of the artificial lumped-component transmission line to the characteristic of the ideal distributed transmission-line section. There is a remarkable difference between the phase response of the single *LC*-cell and the ideal transmission line sections, which is pronounced at lower frequencies for the LH TL and at higher frequencies for the RH TL. Using two cascaded single cells with +45° and −45° electrical lengths for the LH TL and the RH TL, respectively, improves the characteristics drastically. One can conclude that for $\Delta\Phi = 180^\circ$, the artificial lines containing two single cells can be used for a design of the phase shifter. For the smaller phase shifts ($\Delta\Phi \leq 90^\circ$), the single T- or Π-sections can be used for a design of a switchable channel phase shifter providing a phase shift with a small deviation of the phase shift over a wide frequency range.

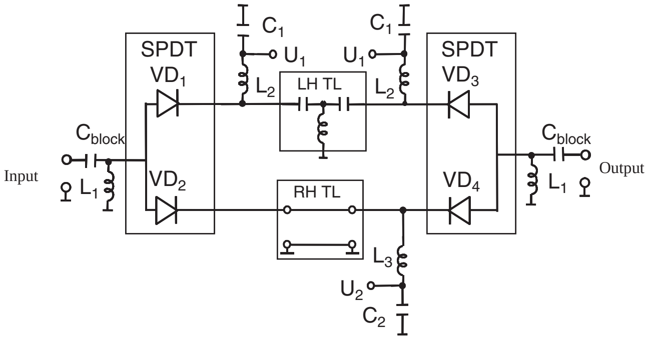

Figure 52. Equivalent circuit of the 180° phase shifter.

When the characteristic impedance of both transmission lines Z_0 is the same and equal to the port impedance, the perfect matching of the network shown in Figure 50 is provided in any frequency range for both states.

Design of Digital Phase Shifters on Switchable LH and RH TL Channels

Let us consider the 180° phase shifter on switchable LH and RH TL channels (69–71). The phase shifter uses switching between the conventional coplanar waveguide section (RH TL) with the electrical length +90° and the artificial lumped-element LH TL section providing the electrical length −90° (Figure 52). The same characteristic impedance $Z_0 = 50$ Ohms for both RH TL and LH TL sections was chosen. To extend the operational bandwidth to one octave with respect to the input matching of the LH TL, the artificial LH TL section was designed as a cascaded connection of two identical lumped-element T-networks with +45° phase response each.

Figure 53a shows a coplanar realization of the phase shifter. The device was manufactured on 1-mm-thick alumina substrate on the base of the sandwich multilayer technology using the screen printing technique (69, 70). Two 15-μm thick conductive layers separated from each other by the additional dielectric layer with the thickness of 60 μm and the dielectric permittivity $\varepsilon_r = 10.2$ were employed to form series capacitors of the artificial LH TL section. Lumped grounded inductors made as short, narrow strips were situated on the bottom conductive layer and connected to the ground plane by via holes. The coplanar RH TL section was implemented on the top conductive layer. The channel switching was carried out by surface-mounted *p-i-n*-diodes. The size of the fabricated phase shifter is $21 \times 14 \times 1.1\,\mathrm{mm}^3$. Simulated amplitude characteristics and the phase shift of the phase shifter in the specified operational bandwidth are shown by dashed lines in Figure 53b–d. The experimental results are presented by solid lines. The experimental investigation was performed using an HP 8720B vector network analyzer. Within the frequency range 2.0–3.6 GHz, the experimentally observed phase shift is 180 ± 7°. The measured value of the return loss is not worse than 11 dB for the RH TL being switched on and not less than 14 dB in the case of the switched on the LH TL section. The insertion loss is not

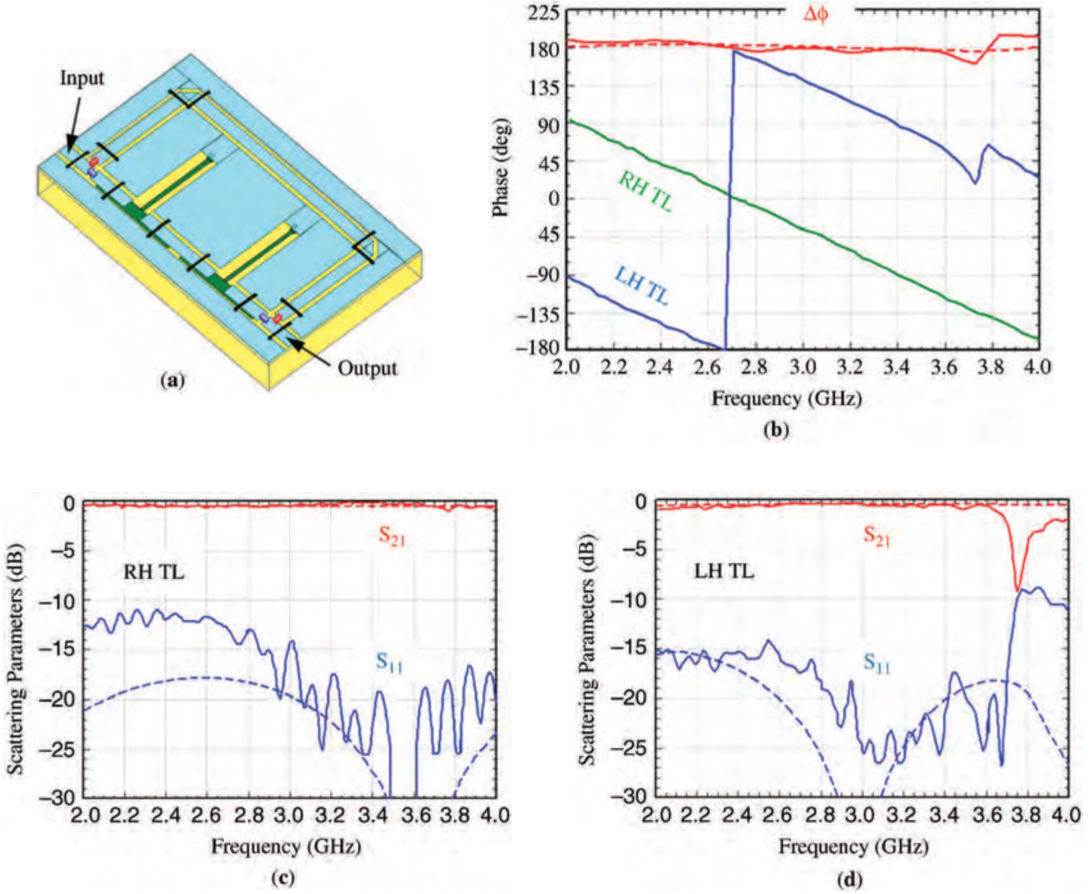

Figure 53. A 180° phase shifter with CPW RH channel and LH channel made on (a) two cascaded T-sections, (b) simulated (dashed lines) and measured (solid lines) phase response of the device, and S-parameters of the phase shifter in two different states: (c) $\varphi = -90°$ and (d) $\varphi = +90°$.

higher than 0.7 dB and 0.9 dB for the RH TL channel and for the LH TL channel, respectively.

A 3-bit phase shifter was designed as a cascaded connection of three 1-bit phase shifters (Figure 54). The area occupied by the device is $45 \times 18\,\text{mm}^2$. The characteristics for all eight states of the 3-bit phase shifter, which were obtained by EM simulation of the multilayer structure taking into account the *p-i-n*-diodes and the biasing networks, are presented in Figure 55. In the frequency range 2–4 GHz, the phase shift error does not exceed ±8° in the worst case. In the same bandwidth, the return loss is about 15 dB and the insertion loss is less than 1 dB.

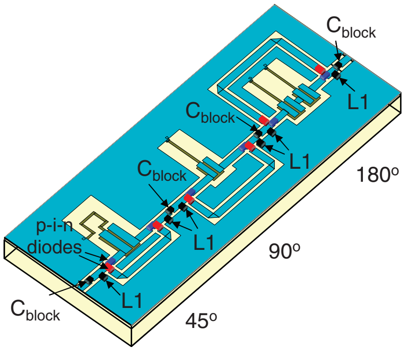

Figure 54. Design of the 3-bit phase shifter.

Digital phase shifters are widely used in antenna arrays providing beam forming and scanning. For the antenna array applications, it is important to design the phase shifters suitable for mass production. Small-size, low-cost, and easy-to-fabricate phased shifters were designed using PCB technology with commercially available SMD components. The 6-bit phase shifter for the frequency range of 5–6 GHz was designed providing the smallest digital phase shift $\Delta\varphi = 5.625°$. For a realization of the high-order bits (45°, 90°, and 180°), the switchable RH and LH TL sections have been used (Figure 56a). Microstrip line sections were used as RH TL sections, and the LH TL section was realized as T-circuit. The low-order bits were designed in a different way (Figure 56b) to minimize the overall insertion loss. NEC micropackaged FET SPDT-switches were employed as the controlling components. To improve the input/output device matching, the order of bits in cascade was optimized (Figure 57a). The 6-bit phase shifter was implemented on 0.625-mm-thick Rogers RO3210 PCB with 0402 SMD passives. The layout of the phase shifter is shown in Figure 57b. The phase shifter performance for all 64 states is presented in Figure 58.

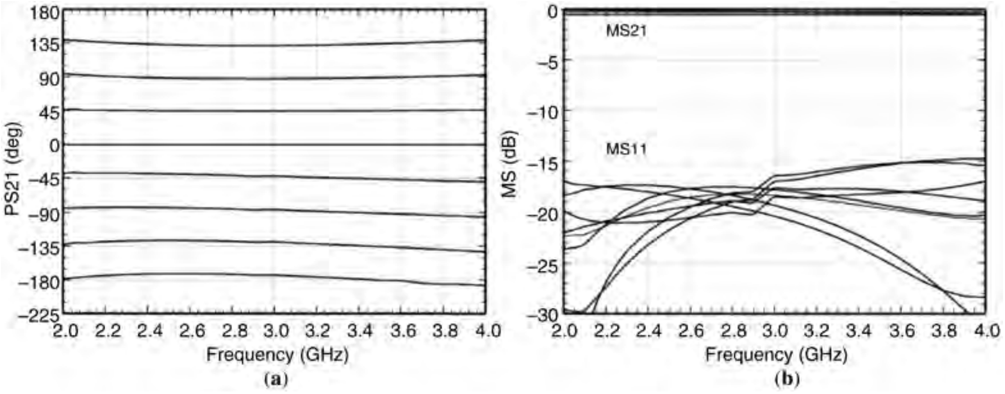

Figure 55. (a) Simulated amplitude and (b) phase characteristics (b) of the 3-bit phase shifter.

The device size is $27 \times 16 \times 1.2\,\text{mm}^3$. In the operational bandwidth, it exhibits a low phase shift error and VSWR < 2. The average insertion loss per bit lies in the range 1–1.3 dB.

Analog Phase Shifter Based on Composite RH/LH Transmission Lines

A composite R/LH TL section can be used for a phase shifter design with tunable components. The analog phase shifter is based on a CRLH TL section with variable capacitors. An equivalent diagram of the single cell is shown in Figure 59. The design of a phase shifter based on such a line controlled by ferroelectric varactors was treated in Ref. 72. A change of the values of tunable capacitors in the unit cell of a tunable CRHL TL (Figure 59) leads to a variation of the electrical length of the cell and, hence, to a change of the phase response along the artificial transmission-line section. For a tunable device, the tunability parameter is introduced. The tunability $n = C(V_1)/C(V_2)$ is defined as the ratio of the two capacitance values $C(V_1)$ and $C(V_2)$ of the tunable capacitor corresponding to the different values of applied voltage.

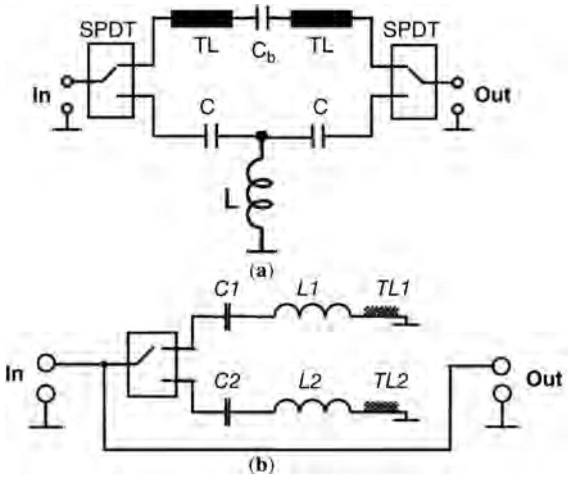

Figure 56. (a) Switchable channels as 1-bit phase shifter for a realization of $\Delta\varphi = 45°$, $90°$, and $180°$. (b) Switchable stubs for a realization of $\Delta\varphi = 5.625°$, $11.25°$, and $22.5°$.

Let us consider an analog composite TL-based phase shifter laid out as a PCB with surface mount components. Tuning is implemented by commercial semiconductor varactor diodes, which suit better than the ferroelectric varactors. To provide matching, the characteristic impedance Z_c of the CRHL TL should be equal to the input impedance Z_0: $Z_c = Z_0 = 50$ Ohms at the central frequency f_0 of the operational frequency band. The matching condition leads to

$$L = \frac{Z_c}{\omega_0} \tag{80}$$

The dependence of the phase shift on the tunability n for a single cell of the CRHL TL, for the balanced case, is described by the formula (5):

$$\Delta\varphi(n) = \Delta\varphi_{RH} + \Delta\varphi_{LH} = 2\pi f\sqrt{LC}(1 - \sqrt{n}) + \frac{1}{2\pi f\sqrt{LC}}\frac{1 - \sqrt{n}}{\sqrt{n}} \tag{81}$$

The dependence of the transmission coefficient and phase shift on tunability n for a single cell of the CRHL TL is

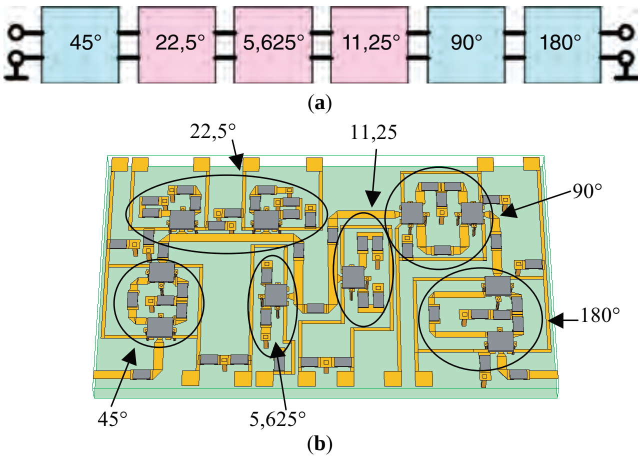

Figure 57. (a) A 6-bit phase shifter as a cascaded connection of different bits. (b) Layout of the PCB device with SMD components.

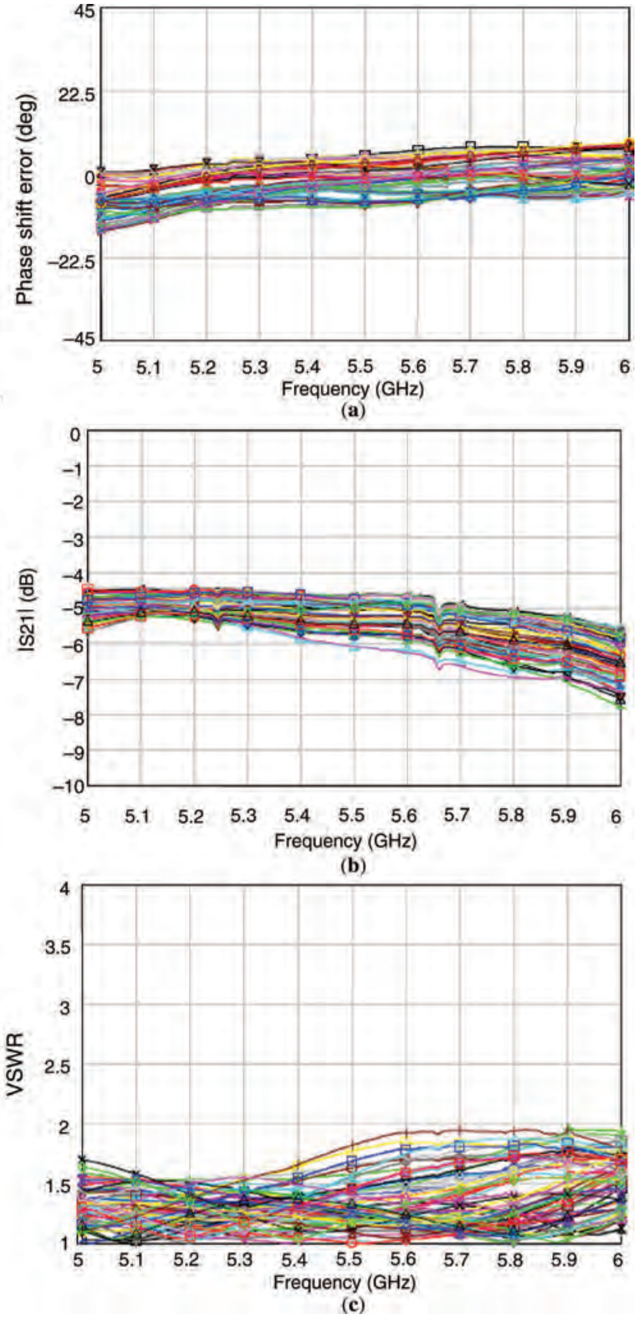

Figure 58. Experimental performance of the 6-bit phase shifter for 64 states: (a) phase shift error, (b) transmission coefficient, and (c) VSWR.

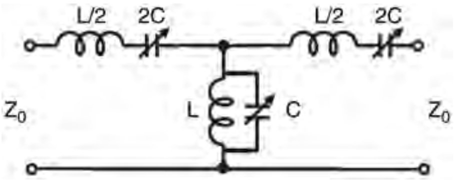

Figure 59. Equivalent diagram of a tunable single cell of the CRLH TL.

shown in Figure 60. The transmission coefficient S_{21} is remarkably decreased for $n > 2$ due to mismatching of the CRHL TL. The characteristic impedance of the tunable CRHL TL depends on the tunability of the tunable capacitances of varactors diodes and is determined as follows:

$$Z_c(\omega) = \sqrt{\frac{B}{C}} = Z_c(\omega_0)\sqrt{1 - \frac{1}{4}\left(\frac{\omega_0}{\omega\sqrt{n}}\right)^2 \left(1 - \frac{\omega^2 \cdot n}{\omega_0^2}\right)^2} \quad (82)$$

Taking into consideration the above-mentioned key points of the design, the number of the unit cells forming the phase shifter should be chosen such as to achieve a phase shift up to 180° and to keep matching conditions in a defined limit. The analysis and schematic simulations of the phase shifter for the frequency range of interest revealed that it is necessary to use four unit cells (73). Such a device provides an insertion loss of 2.5 dB and a return loss of 15 dB.

The layout and photograph of the four-cell 0° to 180° CRLH TL analog phase shifter operating at S-band frequencies implemented on a 1.27-mm-thick printed circuit board from Rogers RO3010 with surface-mount device components is depicted in Figure 61. Miniature flip-chip varactor diodes from Microsemi and high-Q 0402 chip inductors from Murata are used to design the device. All varactors are tuned simultaneously by applying voltage in the range from 1 to 3 V, which corresponds to a tunability of $n = 2.2$. The area of the phase shifter measures $17 \times 8.4\,\text{mm}^2$. The phase shifter characteristics are presented in Figure 62. At a center frequency of 2.7 GHz over a fractional bandwidth of 25%, the EM simulation revealed a flat phase shift with an error less than ±10° for the 180° phase shift, the insertion loss less than 2.5 dB, VSWR < 2, and the return loss better than 15 dB.

ACTIVE MICROWAVE DEVICES ON CRLH TRANSMISSION LINES

In previous sections, mainly passive microwave metamaterial devices have been discussed, although among them tunable, reconfigurable, and controllable devices also have been considered. In such devices, tunable and switchable components (varactors diodes and *p-i-n*-diodes) are used for providing tunability. Most important is that under the constant value of a control voltage or current, the device is linear. At the same time, there is another class of microwave devices known as active ones exhibiting in general nonlinear properties. Microwave amplifiers, oscillators, frequency converters, etc. are widely used in electronic systems. We are not going to consider this class of microwave devices in detail, but we only show that in principle these devices can be improved while using metamaterial TLs. Two examples are briefly described: a microwave amplifier and mixer.

Distributed amplifiers (DAs) are widely used as broadband devices. The DAs with CRHL TLs are very promising for microwave applications. These distributed circuits are based on signal propagation in transmission lines coupled

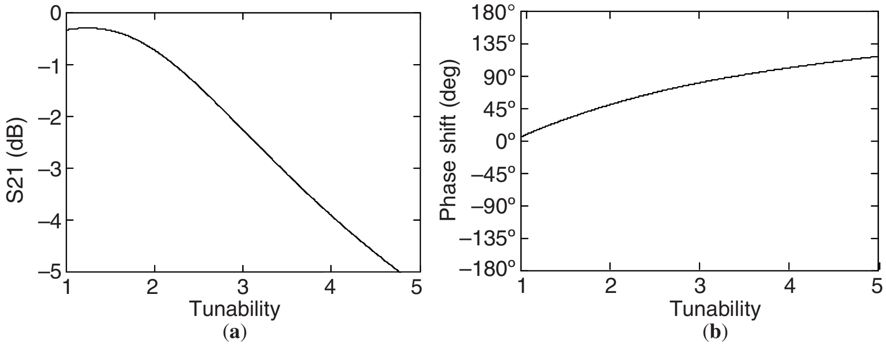

Figure 60. Transmission coefficient and phase response versus capacitance tunability for a single cell of the tunable CRLH TL.

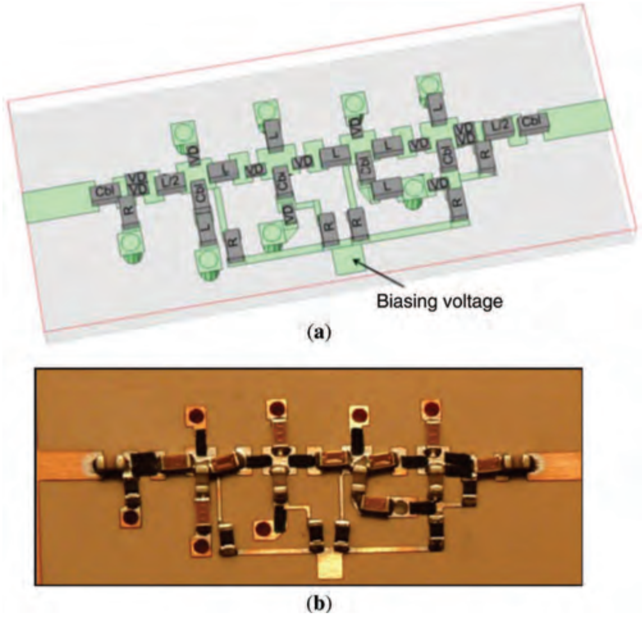

Figure 61. (a) Layout and (b) photo of 0° to 180° CRLH TL phase shifter.

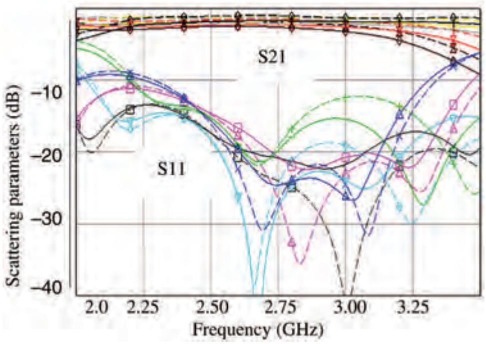

Figure 62. Simulated (dashed lines) and experimental (solid lines) frequency dependence of S-parameters of the analog phase shifter for different phase shifts, corresponding to the variation of the capacitance $n = 1/2.2$ providing the phase shifts $\Delta\varphi = 45^\circ$, 90°, 135°, and 180°.

by active devices (74–76). Using such lines, it is possible to get a very broad operational bandwidth. Due to the CRLH-TL properties exhibiting RH behavior ($\theta_R > 0$) at high frequencies and LH behavior ($\theta_L < 0$) at low frequencies, a new class of distributed amplifiers, known as the meta-distributed amplifier (MDA), has been introduced, offering dual-band amplifying performance. The DA is based on wave propagation along two transmission lines coupled by active devices, which are generally FETs (Figure 63). The input signal travels along the so-called gate line, which interconnects the FET gates. The output wave, amplified by the active devices, travels along the so-called drain line. Thus, two output ports can be defined in the drain line, the forward and reverse ports, and two corresponding gains can also be defined, the forward gain (G_{fwd}) and the reverse gain (G_{rev}). These gains depend on the FET transconductance (g_m), the number of sections (N), and the electrical lengths of the elementary cells (θ_g and θ_d). As the negative values for θ are possible, the conditions $\theta_g - \theta_d = 0$ and $\theta_g + \theta_d = 0$ can be fulfilled at different frequencies by properly designed gate and drain lines. Dual-band behavior can be obtained this way, and separated frequencies or channels can be amplified and extracted separately at the reverse and forward ports.

This concept has also been extended to distributed mixers (meta-distributed mixers) capable of providing mixing with intermediate frequency (IF) signals at different physical output ports (77, 78). Active distributed mixers based on the classic solution provide very wideband mixing performance. Mixers based on artificial CRLH TLs offer new functionalities such as dual-band behavior, diplexer functionality, and image-rejection capability (78). The intrinsic performance of these mixers can bee analyzed by means of a simple lossless continuous model of unilaterally coupled TLs. Any practical implementation must take the form of artificial CRLH TLs periodically loaded/coupled by active devices. The equivalent circuit of a distributed mixer based on CRLH TL sections is shown in Figure 64.

The following types of the distributed mixers can be designed with different functionalities: dual-band diplexer, wideband image-rejection, and dual-band diplexer/image-rejection. The experimental results obtained confirm that such novel performances can be achieved and show the usefulness of the proposed design methodology. Using existing artificial CRLH TL topologies or inhomogeneous

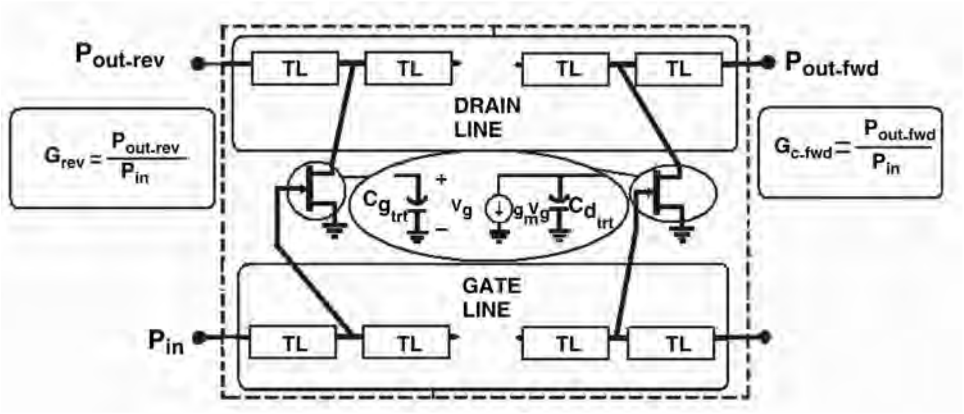

Figure 63. Distributed amplifier equivalent circuit. From Reference 75; copyright © 2006 IEEE, reprinted with permission conveyed through Copyright Clearance Center, Inc.

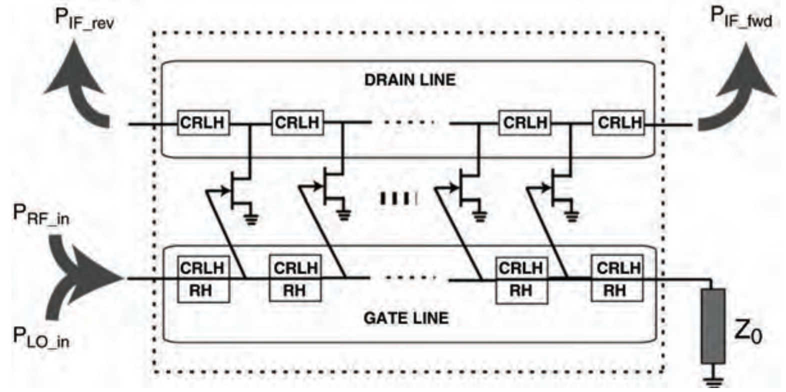

Figure 64. Equivalent diagram of the distributed mixer. From Reference 78; copyright © 2009 IEEE, reprinted with permission conveyed through Copyright Clearance Center, Inc.

structures by employing an advanced artificial TL impedance or dispersion engineering is straightforward for many useful applications.

The use of CRLH TLs in the design of active distributed circuits such as distributed amplifiers or distributed mixers has led to potential new applications for these kinds of microwave circuits. In particular, CRLH TL-based distributed microwave devices exhibit multiband performance.

CONCLUSION

The characteristics of the RH/LH TLs make it possible to use the combination of the RH and LH TL sections and CRLH TL sections as well employ them in beneficial applications in microwave techniques. A new approach to a design of resonators, filters, and digital phase shifters with enlarged functionality demonstrates the exceptional performance of the devices. The combination of the RH and LH TL sections and CRLH TL sections of different designs are also used for characteristic improvement of directional couplers and power splitters. The modern multilayer technology makes it possible to design fully integrated miniature microwave devices on the metamaterial TLs. The novel approach to the design of active microwave devices with implementation of CRLH TLs is also promising providing enlarged functionality of the devices.

BIBLIOGRAPHY

1. V. G. Veselago. The Electrodynamics of Substances with Simultaneously Negative Values of ε and μ. *Sov. Phys. Usp.* **1968**, *10*, 4, pp 509–518.
2. *Metamaterials Handbook, Vol. 1: Phenomena and Theory of Metamaterials, Vol. 2: Applications of Metamaterials*, Ed. F. Capolino, Taylor: Boca-Raton, FL, 2009.
3. *Negative_Refraction Metamaterials: Fundamental Principles and Applications*, Eds. G. V. Eleftheriades and K. G. Balmain, Wiley_IEEE: Hoboken, NJ, 2005.
4. *Metamaterials: Physics and Engineering Explorations*, Eds. N. Engheta and R. W. Ziolkowski, Wiley IEEE: Hoboken, NJ, 2006.
5. C. Caloz and T. Itoh. *Electromagnetic Metamaterials: Transmission Line Theory and Microwave Applications*. Wiley: New York, 2006.
6. R. Marques, F. Martin, and M. Sorolla. *Metamaterials with Negative Parameters: Theory, Design and Microwave*

Applications, Wiley Series in Microwave and Optical Engineering, Wiley-Blackwell, New York, 2008.

7. J. A. Kong. *Electromagnetic Wave Theory*. EMW Publishing: MA, 2005.
8. L. Brillouin et M. Parodi. *Propagation des ondes dans les milieux periodiques*. Masson et C^{ie} eds. et Dunod Editeurs, 1956.
9. K. C. Gupta, R. Garg, and R. Ghadha. *Computer-Aided Design of Microwave Circuits*, Artech House: Dedham, MA, 1981.
10. I. B. Vendik, O. G. Vendik, D. V. Kholodnyak, E. V. Serebryakova, and P. V. Kapitanova. Digital Phase Shifters Based on Right- and Left-Handed Transmission Lines. *Proc. of the EuMA* **2006**, *2*, pp 30–37.
11. A. Lai, C. Caloz, and T. Itoh. Composite Right/Left-Handed Transmission Line Metamaterials, *IEEE Microw. Mag.* **2004**, *5*, pp 34–50.
12. M. Durán-Sindreu, G. Sisó, J. Bonache, and F. Martín. Planar Multi-Band Microwave Components Based on the Generalized Composite Right/Left Handed Transmission Line Concept. *IEEE Trans. Microw. Theor. Tech.* **2010**, *58*, pp 3882–3891.
13. Y. Dong and T. Itoh. Promising Future of Metamaterials, *IEEE Microw. Mag.* **2012**, *13*, pp 39–56.
14. M. Durán-Sindreu, J. Naqui, J. Selga, P. Vélez, J. Bonache, and F. Martín. Composite Right-/Left-Handed Transmission Line Metamaterials, in Wiley Encyclopedia of Electrical and Electronics Engineering ed. John G. Webster.
15. F. Martín, J. Bonache, M. Durán-Sindreu, J. Naqui, F. Paredes, and G. Zamora. Artificial Transmission Lines, in Wiley Encyclopedia of Electrical and Electronics Engineering ed. John G. Webster.
16. G. V. Eleftheriades, A. K. Iyer, and P. C. Kremer. Planar Negative Refractive Index Media Using, Periodically L–C Loaded Transmission Lines. *IEEE Trans. Microw. Theor. Tech.* **2007**, *50*, pp 2702–2712.
17. A. K. Iyer and G. V. Eleftheriades. Metamaterials, in Wiley Encyclopedia of Electrical and Electronics Engineering ed. John G. Webster.
18. I. B. Vendik, D. V. Kholodnyak, I. V. Kolmakova, E. V. Serbryakova, P. V. Kapitanova, F. Martín, J. Bonache, J. García, I. Gil, and M. Gil. Applications of Right/Left Handed and Resonant Left Handed Transmission Lines for Microwave Circuit Design. *Proc. of the 36th European Microwave Conference EuMC36*, October 2006, Manchester UK, pp 955–958.
19. J. Garcia-Garcia, I. B. Vendik, B. Sans, D. Kholodnyak, P. Kapitanova, J. Bonache, and F. Martin. Miniaturization and Optimization of Planar Microwave Filters Based on Metamaterials, *Proc. 37th European Microwave Conference EuMC37*, October 2007, Munich Germany, pp. 500–503.
20. P. Kapitanova, D. Kholodnyak, S. Humbla, R. Perrone, J. Mueller, M. A. Hein, and I. B. Vendik. Multi-band and tunable multi-band microwave resonators and filters on cascaded left/right–handed transmission line sections, *Proc. EUROCON 2009*, 18–23 May 2009, Saint Petersburg, Russia, pp. 60–66, **2009**.
21. K. Zemlyakov and I. Vendik. Tuneable Microwave Resonators and Filters on Combination of Right/Left Handed Transmission Line Sections for Multiband Applications, Proc. Metamaterials'2010, Karlsruhe, Germany, September 2010, pp. 423–425.
22. J. R. Crute and L. Davis. A Compact Microstrip Interdigital Stepped-Impedance Bandpass Filter with Enhanced Stopbad. *Microw. Opt. Tech. Lett.* **2002**, *31*, pp 336–340.
23. C.-Wen Tang. Harmonic-Suppression LTCC Filter with the Step-Impedance Quarter Wavelength Open Stub. *IEEE Trans. Microw. Theory Tech.* **2004**, *52*, pp 617–624.
24. J.,-T. Kuo and C.-Y. Tsai. Periodic Stepped-Impedance Ring Resonator (PSIRR) Filter with a Miniaturized Area and Desirable Upper Stopband Characteristics. *IEEE Trans. Microw. Theory Tech.* **2006**, *54*, pp 1107–1112.
25. S.-Gang Mao, M.-Sou Wu, and Y.-Zhi Chuch. Design of Composite Right/Left-Handed Coplanar-Waveguide Band-Pass and Dual-Passband Filters. *IEEE Trans. Microw. Theory Tech.* **2006**, *54*, pp 3543–3549.
26. H. Joshi and W. J. Chappel. Dual-Band Lumped-Element Bandpass Filter. *IEEE Trans. Microw. Theory Tech.* **2006**, *54*, pp 4169–4177.
27. X. Q. Lin, R. P. Liu, X. M. Yang. Arbitrarily Dual-Band Components Using Simplified Structures of Conventional CRLH TLs. *IEEE Trans. Microw. Theory Tech.* **2006**, *54*, pp 2902–2909.
28. A. Görür and C. Karpuz. Miniature Dual-Mode Microstrip Filters. *IEEE Microw. Wireless Compon. Lett.* **2007**, *17*, pp 37–39.
29. P. Kapitanova, D. Kholodhyak, S. Humbla, R. Perrone, J. Mueller, M.A. Hein, and I. Vendik. Right- and Left-Handed Transmission Line Resonators and Filters for Dual Band Application. *Microw. Opt. Tech. Lett.* **2009**, *51*, pp 629–633.
30. P. V. Kapitanova, A. V. Simine, D. V. Kholodnyak, and I.B. Vendik. Multilayer Thick-Film Technology as Applied to Design of Microwave Device. *J. Eur. Ceram. Soc.* **2007**, *27*, pp 2941–2944.
31. J. Müller, R. Perrone, H. Thust, K.H. Drüe, C. Kutscher, R. Stephan, J. Trabert, M. A. Hein, D. Schwanke, J. Pohlner, G. Reppe, R. Kulke, P. Uhlig, A. F. Jacob, T. Baras, and A. Molke. Technology Benchmarking of High-Resolution Structures on LTCC for Microwave Circuits. *Proc. 2006 Electronics System Integration Technology Conference*, ESTC, Dresden, Germany, pp 5–7, **2006**.
32. S.-G. Mao, M.-S. Wu, and Y.-Z. Chueh. Design of Composite Right/Left-Handed Coplanar-Waveguide Bandpass and Dual-Passband Filters. *IEEE Trans. Microw. Theory Tech.* **2006**, *54*, pp 3543–3549.
33. J. Bonache, G. Sisó, M. Gil, A. Iniesta, J. García-Rincón, and F. Martín. Application of Composite Right/Left Handed (CRLH) Transmission Lines Based on Complementary Split Ring Resonators (Csrrs) to the Design of Dual Band Microwave Components. *IEEE Microw. Wireless Compon. Lett.* **2008**, *18*, pp 524–526.
34. G. V. Eleftheriades. A Generalized Negative-Refractive-Index Transmission Line (NRL-TL) Metamaterial for Dual-Band and Quad-Band Applications. *IEEE Microw. Wireless Compon. Lett.* **2007**, *17*, pp 415–417.
35. M. Studniberg and G. V. Eleftheriades. A Dual-Band Bandpass Filter Based on Generalized Negative-Refractive-Index Transmission-Lines. *IEEE Microw. Wireless Compon. Lett.* **2009**, *19*, pp 18–20.
36. M. Durán-Sindreu, G. Sisó, J. Bonache, and F. Martín. Planar Multi-Band Microwave Components Based on the Generalized Composite Right/Left Handed Transmission Line Concept. *IEEE Trans. Microw. Theor. Tech.* **2010**, *58*, pp 3882–3891.
37. A. Velez, F. Aznar, J. Bonache, M. C. Velázquez-Ahumada, J. Martel, and F. Martín. Open Complementary Split Ring Resonators (OCSRRs) and their Application to Wideband CPW Band Pass Filters. *IEEE Microw. Wireless Compon. Lett.* **2009**, *19*, pp 197–199.

38. A. S. Rusakov, I. B. Vendik, S. Qian.A Direct Synthesis Method for UWB Bandpass Filters Based on Metamaterial Transmission lines, *6th International Congress on Advanced Electromagnetic Materials in Microwaves and Optics–Metamaterials 2012*, Proc. Metamaterials' 2012, St. Petersburg, September 2012, pp 387–389, **2012**.
39. S. Qian and J. Hong. Miniature Quasi-Lumped-Element Wideband Bandpass Filter at 0.5–2-GHz Band Using Multilayer Liquid Crystal Polymer Technology, *IEEE Trans. Microw. Theory Tech.* **2012**, *60*, pp 2799–2807.
40. S. Qian, J. Hong, A. Rusakov, and I. B. Vendik. A Novel Compact Ultra-Wideband Bandpass Filter. *Proc. European Microw. Conf. EuMC43*, October 2013, pp 896–899.
41. M. Gil, J. Bonache, J. García-García, J. Martel, and F. Martín, Composite Right/Left-Handed Metamaterial Transmission Lines Based on Complementary Split-Rings Resonators and Their Applications to Very Wideband and Compact Filter Design. *IEEE Trans. Microw. Theor. Tech.* **2007**, *55*, pp 1296–1304.
42. J. Ni, I. Vendik, D. Kholodnyak, and J. Hong. A Compact Bandpass Filter Based on Right- and Left-Handed Transmission Line Sections. *IEEE Microw. Wireless Compon. Lett.* **2013**, *23*, pp 279–281.
43. R. Gómez-García and Manuel Sánchez-Renedo. A Class of Microwave Transversal Signal-Interference Dual-Passband Planar Filters. *IEEE Microw. Wireless Compon. Lett.* **2009**, *19*, pp 158–160.
44. M. Á. Sánchez-Soriano and E. Bronchalo. Compact UWB Bandpass Filter Based on Signal Interference Techniques. *IEEE Microw. Wireless Compon. Lett.* **2009**, *19*, pp 692–694.
45. V. Piatnitsa, D. Kholodnyak, P. Kapitanova, I. Fischuk, T. Tick, J. Jantti, H. Jantunen, and I. Vendik. Right/Left-Handed Transmission Line LTCC Directional Couplers. *Proc. of 37th European Microwave Conf. EuMC37*, Munich, Germany, pp 636–639, **2007**.
46. I. Vendik, D. Kholodnyak, E. Serebryakova, and P. Kapitanova. Miniature Microwave Devices Based on a Combination of Natural Right-Handed and Metamaterial Left-Handed Transmission Lines. *Eur. Phys. J. Appl. Phys.* **2009**, *46*, p. 32610.
47. D. Kholodnyak, P. Kapitanova, and I. Vendik. Design of Directional Couplers Using Fully-Integrated Left-Handed Transmission Lines. *Proceedings of First Int. Congress on Advanced Electromagnetic Materials in Microwaves Electromagnetic Materials in Microwaves and Optics*, September 2007, Rome, Italy, pp 91–94, **2007**.
48. J. Müller, R. Perrone, P. Kapitanova, D. Kholodnyak, I. Vendik, S. Humbla, and M.A. Hein. Highly Integrated Passive LTCC Device with Embedded High-K Capacitors. *Proc. IMAPS/ACerS, 5th Int. Conf. on Ceramic Interconnect and Ceramic Microsystems Technologies (CICMT 2009)*, 21–23 April 2009, Denver, Colorado. pp 193–198, **2009**.
49. R. Perrone, P. Kapitanova, D. Kholodnyak, I. Vendik, S. Humbla, M. Hein, and J. Müller. Miniaturisation of a LTCC High-Frequency Rat-Race-Ring by Using 3-Dimensional Integrated Passives and Embedded High-K Capacitors. *Proc. 17th European Microelectronics and Packaging Conf.*, 15–17 June 2009, Rimini, Italy, **2009**.
50. Gerard Sisó, Jordi Bonache, Marta Gil, Joan García-García and Ferran Martín, Compact Rat-Race Hybrid Coupler Implemented Through Artificial Left Handed and Right Handed Lines, *Proc. Microwave Symposium* IEEE/MTT-S, IMS 2007, 3–8 June 2007, Honolulu, Hawaii, pp 25–28, **2007**.
51. M. Gil, J. Bonache, I. Gil, J. García-García, and F. Martín. Artificial Left-handed Transmission Lines for Small Size Microwave Components: Application to Power Dividers, *Proc. of the 36th European Microwave Conf. (EuMC 2006)*, pp 1135–1138, Manchester, UK, September **2006**.
52. M. Gil, J. Bonache, I. Gil, J. García-García, and F. Martín. On the Transmission Properties of Left Handed Microstrip Lines Implemented by Complementary Split Rings Resonators. *Int. J. Numer. Modell.: Electron. Networks, Devices Fields* **2006**, *19*, pp 87–103.
53. J. Bonache, F. Falcone, J. D. Baena, T. Lopetegi, J. García-García, M. A. G. Laso, I. Gil, A. Marcotegui, R. Marqués, F. Martín, and M. Sorolla. Application of Complementary Split Rings Resonators to the Design of Compact Narrow Band Pass Structure in Microstrip Technology. *Microw. Opt. Tech. Lett.* **2005**, *46*, pp 508–512.
54. M. A. Antoniades and G. V. Eleftheriades. A Broadband Wilkinson Balun Using Microstrip Metamaterial Lines. *IEEE Antenn. Wireless Propag. Lett.* **2005**, *4*, pp 209–212.
55. D. V. Kholodnyak, P. Kapitanova, I. Vendik, S. Humbla, R. Perrone, J. Mueller, and M. A. Hein. Novel Wilkinson-Type Power Dividers Based on Metamaterial Transmission Lines. *38th European Microwave Conference EuMC38*, October 2008, Amsterdam, Netherland, pp 341–344, **2008**.
56. I. H. Lin, M. DeVincentis, C. Caloz, and T. Itoh. Arbitrary Dual-Band Components Using Composite Right/Left-Handed Transmission Lines. *IEEE Trans. MTT* **2004**, *52*, pp 1142–1149.
57. C. Collado, A. Grau, and F. De Flaviis. Dual-Band Planar Quadrature Hybrid with Enhanced Bandwidth Response. *IEEE Trans. MTT* **2006**, *54*, pp 180–188.
58. X. Q. Lin, R. P. Liu, X. M. Yang. Arbitrarily Dual-Band Components Using Simplified Structures of Conventional CRLH TLs. *IEEE Trans. MTT* **2006**, *54*, pp 2902–2909.
59. I. Lin, C. Caloz, and T. Itoh. A Branch-Line Coupler With Two Arbitrary Operating Frequencies Using Left-Handed Transmission Lines. In *IEEE-MTT Int. Symp. Dig*. Philadelphia, PA, 2003, vol. 1, pp 325–327.
60. M. Durán-Sindreu, G. Sisó, J. Bonache, and F. Martín. Fully Planar Implementation of Generalized Composite Right/Left Handed Transmission Lines for Quad-Band Applications. In *Proc. IEEE-MTT-S Int. Microw. Symp*., Anaheim, CA, May 2010, pp 25–28.
61. P. Kapitanova, D. Kholodnyak, and I. Vendik. Tuneable Lumped Element Directional Coupler Using Metamaterial Tramsmission Lines. *Proceedings of 39th European Microwave Conf. EuMC39*, October 2009, Rome, Italy, pp 1247–1250, **2009**.
62. P. Kapitanova, D. Kholodnyak, S. Humbla, R. Perrone, J. Mueller, M.A. Hein, and I. Vendik. Tunable Microwave Devices Based on Left/Right-Handed Transmission Line Sections in Multilayer Implementation. *Int. J. Microw. Wireless Tech.* **2009**, *1*, pp 323–329.
63. http://www.skyworksinc.com
64. S.-K. Hsu, C.-H. Tsai, and T.-L. Wu. A Novel Miniaturized Forward-Wave Directional Coupler with Periodical Mushroom-Shaped Ground Plane. *IEEE Trans. Microw. Theory Tech.* **2010**, *58*, pp 2277–2283.
65. S.-K. Hsu, J.-C. Yen, and T.-L. Wu. A Novel Compact Forward-Wave Directional Coupler Design Using Periodical Patterned Ground Structure. *IEEE Trans. Microw. Theory Tech.* **2011**, *59*, pp 1249–1257.
66. I. Munina, I. Vendik, and V. Crnojevic-Bengin. Design of 0-dB Reconfigurable Directional Coupler Using Metamaterial Structure. *Proc. 7th International Congress on Advanced*

Electromagnetic Materials in Microwaves and Optics–Metamaterials 2013. Bordeaux, France, 16–21 September **2013**.

67. M. Antoniades and G. V. Eleftheriades. Compact, Linear, Lead/Lag Metamaterial Phase Shifters for Broadband Applications. *IEEE Antennas Wireless Propag. Lett.* **2003**, *2*, pp 103–106.
68. S. K. Koul and B. Bhat. *Microwave and Millimeter Wave Phase Shifters*. Artech House: Boston, MA, 1991.
69. O. G. Vendik, I. B. Vendik, D. V. Kholodnyak, S. P. Zubko, and E. V. Serebryakova. Electronically Controlled Phase Shifters Based on Right/Left-Handed Transmission Lines, *Proc. of 35th European Microwave Conf. EuMC35*, Paris, France, October, 2005, pp 909–912.
70. D. Kholodnyak, E. Serebryakova, I. Vendik, and O. Vendik. Broadband Digital Phase Shifter Based on Switchable Right- and Left-Handed Transmission Line Sections. *IEEE Microw. Wireless Compon. Lett.* **2006**, *16*, pp 258–260.
71. I. B. Vendik, D. V. Kholodnyak, I. V. Kolmakova, E. V. Serebryakova, and P. V. Kapitanova. Microwave Devices Based on Transmission Lines with Positive/Negative Dispersion. *Microw. Opt. Tech. Lett.* **2006**, *48*, pp 2632–2638.
72. D. Kuylenstierna, A. Vorobiev, P. Linner, and S. Gevorgian. Composite Right/Left Handed Transmission Line Phase Shifter Using Ferroelectric Varactors. *IEEE Microw. Wireless Comp. Lett.* **2006**, *16*, pp 167–169.
73. E. Zameshaeva, D. Stoepel, S. Humbla, M.A. Hein, and I.B. Vendik. 180° Analogue S-Band Phase Shifter Based on Composite Right/Left-Handed Transmission Lines. *Proceedings of 5th International Congress on Advanced Electromagnetic Materials in Microwaves and Optics (Metamaterials 2011)*, Barcelona, Spain, 2011, pp 358–360.
74. J. Mata-Contreras, T.M. Martín-Guerrero, and C. Camacho-Peñalosa. Distributed Amplifiers with Composite Left/Right-Handed Transmission Lines. *Microw. Opt. Tech. Lett.* **2006**, *48*, pp 609–613.
75. J. Mata-Contreras, T.M. Martín-Guerrero, and C. Camacho-Peñalosa. Experimental Performance of a Meta-Distributed Amplifier. *Proceedings of the 37th European Microwave Conference EuMC37*. October 2007, Munich Germany, pp 743–746.
76. S. H. Ji, C. S. Cho, J. W. Lee, and J. Kim. Concurrent Dual-Band Class-E Power Amplifier Using Composite Right/Left-Handed Transmission Lines. *IEEE Trans. Microw. Theory Tech.* **2007**, *55*, pp 1341–1347.
77. J. Mata-Contreras, T. M. Martín-Guerrero, and C. Camacho-Peñalosa. Distributed Mixers with Composite Right/Left-Handed Transmission Lines, in *Proc. Integr. Nonlinear Microw. Millimeter-Wave Circuits Conf.*, Aveiro, Portugal, 2006, pp 98–101.
78. J. Mata-Contreras, C. Camacho-Peñalosa, and T. M. Martín-Guerrero. Active Distributed Mixers Based on Composite Right/Left-Handed Transmission Lines. *IEEE Trans. Microw. Theory Tech.* **2009**, *57*, pp 1091–1101.

IRINA VENDIK

St. Petersburg Electrotechnical University, Russia